Magnetoelastic Coupling in Mn-Fe-P-Si Compounds

Miao, Xue-fei

Important note
To cite this publication, please use the final published version (if applicable).
Please check the document version above.

MAGNETOELASTIC COUPLING IN MN-FE-P-SI COMPOUNDS

Magnetoelastic Coupling in Mn-Fe-P-Si Compounds

Proefschrift

ter verkrijging van de graad van doctor
aan de Technische Universiteit Delft,
op gezag van de Rector Magnificus prof. ir. K.C.A.M. Luyben,
voorzitter van het College voor Promoties,
in het openbaar te verdedigen op donderdag 7 juli 2016 om 15:00 uur

door

Xue-Fei Miao

Master in Materials Science and Engineering,
Nanjing University of Aeronautics and Astronautics, China

geboren te Nantong, China.

This dissertation has been approved by the

promotor: Prof. dr. E.H. Brück
copromotor: Dr. ir. N.H. van Dijk

Composition of the doctoral committee:

Rector Magnificus,	voorzitter
Prof. dr. E.H. Brück,	Technische Universiteit Delft
Dr. ir. N.H. van Dijk,	Technische Universiteit Delft

Independent members:

Prof. dr. P. Nordblad,	Uppsala Universitet
Prof. dr. A. Planes Vila,	Universitat de Barcelona
Dr. ir. G.A. de Wijs,	Radboud Universiteit
Prof. dr. C. Pappas	Technische Universiteit Delft
Prof. dr. H.T. Wolterbeek	Technische Universiteit Delft
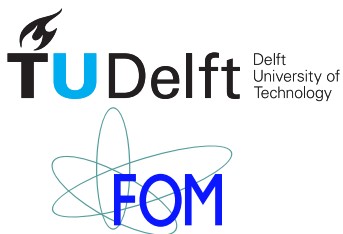
Dedicated to my parents and my wife Fengjiao

CONTENTS

1

INTRODUCTION

Magnetic refrigeration, based on magnetocaloric effect, has been considered to be the most promising technology to replace vapor-compression for near room-temperature refrigeration applications (e.g. refrigerator, air-conditioner). It has been demonstrated that the cooling efficiency of magnetic refrigeration systems can reach up to 60% of the theoretical limit, compared to about 45% in the best gas-compression refrigerators [1–4]. Cooling systems based on magnetocaloric technology operate with less noise due to the absence of a compressor. Additionally, magnetic refrigeration makes use of water-based coolants instead of ozone depleting or greenhouse gases, which makes it an environmentally friendly technology.

$(Mn,Fe)_2(P,Si)$-type compounds are, to date, the best candidate for magnetic refrigeration and energy conversion applications due to the combination of highly tunable giant magnetocaloric effect and low material cost. In this chapter, the magnetocaloric effect and some well-studied magnetocaloric materials are introduced. Since this thesis aims at a better understanding of the magnetoelastic coupling in $(Mn,Fe)_2(P,Si)$-based compounds, previous studies on the crystal structure and the unique mixed magnetism for $(Mn,Fe)_2(P,Si)$-based compounds are summarized. The outline of the thesis can be found at the end of this chapter.

1.1. MAGNETOCALORIC EFFECT

MAGNETIC refrigeration is based on the magnetocaloric effect (MCE). The MCE is a phenomenon, in which a temperature change is caused by exposure of a magnetic material to a changing magnetic field. The magnetocaloric effect was discovered in 1917 by Weiss and Piccard [5]. A temperature rise of 0.7 K was observed in nickel when a magnetic field of 1.5 T was applied in the vicinity of its Curie temperature (627 K).

In the 1920s, Debye [6] and Giauque [7] independently proposed that low temperatures can be attained via adiabatic demagnetization of a paramagnetic salt. This was first experimentally demonstrated by Giauque and MacDougall in 1933 when they reached a temperature of 0.25 K [8]. Due to his great achievement, Giauque was awarded the Nobel Prize in Chemistry in 1949.

In 1997, the first near-room-temperature, proof-of-concept, magnetic refrigerator was built by Ames Laboratory at Iowa State University [1], using gadolinium material. Encouraged by this great success, scientists and companies worldwide started to develop new materials and systems for near room-temperature magnetic-refrigeration applications.

A major breakthrough came in 2002 when Brück [9] and coworkers at the University of Amsterdam discovered the giant MCE in Fe_2P-type magnetocaloric materials. The $(Mn,Fe)_2(P,As)$ compounds present excellent magnetocaloric properties and are based on abundantly available materials. Further success was made when the toxic element As was replaced by the non-toxic Ge and Si, while maintaining the outstanding magnetocaloric properties. [10–16]

In 2015, Haier, Astronautics, and BASF presented the first commercial prototype of a magnetocaloric wine cooler at the International Consumer Electronics Show in Las Vegas, Nevada. Key to this great success is the use of Fe_2P-type magnetocaloric materials, which are composed of abundantly available and affordable raw materials.

1.2. MAGNETOCALORIC MATERIALS

FOLLOWING the discovery of a sub-room temperature giant MCE in the ternary system Gd-Ge-Si [17], great efforts have been made to search for new classes of materials, which can be used for near room-temperature magnetic refrigeration applications. Some examples of these materials are: $La(Fe,Si)_{13}$-based compounds [18, 19], MnAs-based compounds [20], MnCoGe-based compounds [21], Heusler-type NiMnX-based alloys [22–26], and $(Mn,Fe)_2(P,X)$-based compounds [10–16]. The most prominent feature of these material systems is that they undergo a first-order magnetic phase transition, which leads to a giant MCE in the vicinity of the phase-transition temperature.
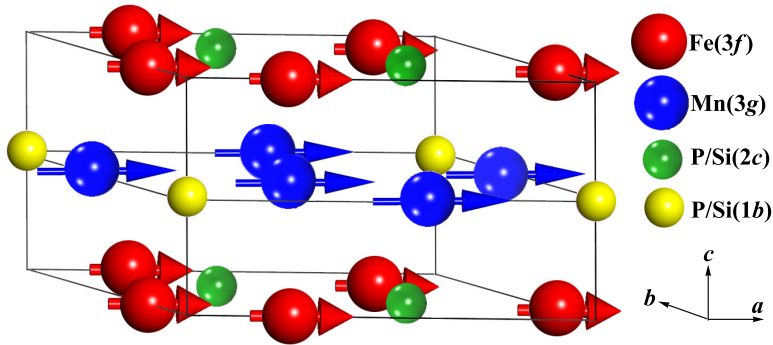
Figure 1.1: Schematic representation of the crystal and magnetic structure for $(\text{Mn,Fe})_2(\text{P,Si})$.

Among the diverse classes of magnetocaloric materials, the $(\text{Mn,Fe})_2(\text{P,Si})$-based compounds have been considered as the most promising materials for room-temperature refrigeration and energy conversion applications due to their combination of tunable working temperature, low hysteresis, corrosion resistance, compositional stability and low material cost.

1.3. CRYSTAL STRUCTURE OF $(\text{Mn,Fe})_2(\text{P,Si})$

THE $(\text{Mn,Fe})_2(\text{P,Si})$ compounds crystallize in the hexagonal Fe_2P-type structure (space group $P\bar{6}2m$), which contains two metallic ($3f$ and $3g$) and two non-metallic ($2c$ and $1b$) sites.

Neutron diffraction experiments and density functional theory (DFT) calculations indicate a preferential occupation of the two transition-metal atoms in the hexagonal structure [27–29]. As illustrated in Fig. 1.1, Mn prefers the $3g$ site with five nonmetal nearest neighbors forming a square pyramid, while Fe favors the $3f$ site surrounded by four nonmetal coordination atoms forming a tetrahedron. The site preference of the non-metal atoms and its influence on the phase transition will be studied in this thesis (*Chapter 3* and *4*).

1.4. MAGNETOELASTIC COUPLING AND MIXED MAGNETISM

THE giant MCE in $(\text{Mn,Fe})_2(\text{P,Si})$ compounds originates from a first-order magnetoelastic transition (FOMT), i.e., the ferromagnetic-paramagnetic (FM-PM) transition is strongly coupled to a structure change without a symmetry change [15, 27, 30, 31]. Due to the strong magnetoelastic coupling in the $(\text{Mn,Fe})_2(\text{P,Si})$ compounds, the phase transition can be tuned by changing the Mn/Fe ratio and P/Si ratio, as well as by doping with small atoms, which are studied in this thesis (*Chapters 3* and *4*). Additionally, the $(\text{Mn,Fe})_2(\text{P,Si})$ compounds show competing

magnetic configurations in the magnetically ordered state. An incommensurate magnetic structure, instead of the common ferromagnetic structure, is observed in some of the $(Mn,Fe)_2(P,Si)$ compounds due to the strong magnetoelastic coupling. This is discussed in *Chapter 7*.

As indicated by DFT calculations [15, 32, 33], the first-order phase transition in $(Mn,Fe)_2(P,Si)$ compounds originates from a unique phenomenon called mixed magnetism. Mn atoms on the $3g$ sites do not undergo a significant reduction in magnetic moment, but only lose the long-range magnetic order above FM to PM transition temperature. In contrast, the magnetic moment of Fe is significantly reduced above the ferromagnetic transition, due to the strong electronic redistribution around the $3f$ site. The appearance of different magnetic behaviors for Fe and Mn atoms in the $(Mn,Fe)_2(P,Si)$ compounds, i.e., mixed magnetism, is a result of the different coordination environments around them, as discussed in Section 1.3.

Mixed magnetism is at the core of the FOMT in the $(Mn,Fe)_2(P,Si)$-based compounds. The tunability of the FOMT, in terms of the critical temperature and the character of the phase transition, is essentially attributed to changes in the mixed magnetism in the $(Mn,Fe)_2(P,Si)$-type compounds.

1.5. THESIS OUTLINE

T HIS thesis aims at shedding light on the magnetoelastic coupling and the phase-transition behavior in $(Mn,Fe)_2(P,Si)$-based compounds.

The experimental techniques (including sample preparation and characterization) employed in this thesis are described in *Chapter 2*.

In *Chapters 3* and *4*, we explore two ways of tailoring the magnetoelastic transition in the $(Mn,Fe)_2(P,Si)$-type compounds through varying the P/Si ratio and doping with small atoms (e.g. B, C and N), respectively. The underlying mechanism can be explained by changes in the mixed magnetism, which are closely related to the competition between chemical bonding and magnetic moment formation.

The study on the thermal-history dependent phase-transition behavior, i.e., the so-called "virgin effect" in the $(Mn,Fe)_2(P,Si)$-type compounds is presented in *Chapter 5*. Based on the experimental results, a thermodynamic model is proposed to describe the virgin effect.

The development of magnetic correlations and their dynamics in the paramagnetic regime of $(Mn,Fe)_2(P,Si)$-type compounds is studied in *Chapter 6*, by means of neutron polarization analysis and muon spin-relaxation techniques.

In *Chapter 7*, an anomalous phase-coexistence phenomenon in some $(Mn,Fe)_2(P,Si)$-based compounds is reported at temperatures below the critical phase-transition temperature. The coexisting phases consist of a stable FM phase

and a metastable incommensurate-magnetic phase, as indicated by neutron diffraction and Mössbauer spectroscopy. The phase coexistence is caused by the kinetic arrest of the first-order phase transition and the competition between different magnetic configurations in some of the $(Mn,Fe)_2(P,Si)$-based compounds. This study provides further insight into the magnetoelastic coupling in $(Mn,Fe)_2(P,Si)$- type compounds.

REFERENCES

[1] C. Zimm, A. Jastrab, A. Sternberg, V. Pecharsky, K. A. Gschneidner, Jr, M. Osborne, and I. Anderson, *Description and performance of a near-room temperature magnetic refrigerator,* in *Advances in Cryogenic Engineering,* Advances in Cryogenic Engineering, Vol. 43, edited by P. Kittel (Springer US, 1998) Chap. 222, pp. 1759–1766.

[2] E. Brück, *Developments in magnetocaloric refrigeration,* J. Phys. D: Appl. Phys. **38**, R381 (2005).

[3] E. Brück, O. Tegus, D. T. C. Thanh, and K. H. J. Buschow, *Magnetocaloric refrigeration near room temperature (invited),* J. Magn. Magn. Mater. **310**, 2793 (2007).

[4] O. Gutfleisch, M. A. Willard, E. Brück, C. H. Chen, S. G. Sankar, and J. P. Liu, *Magnetic materials and devices for the 21st century: stronger, lighter, and more energy efficient,* Advanced Materials **23**, 821 (2011).

[5] P. Weiss and A. Piccard, *Le phénomène magnétocalorique,* J. Phys. Theor. Appl. **7**, 103 (1917).

[6] P. Debye, *Einige bemerkungen zur magnetisierung bei tiefer temperatur,* Ann. Phys. **386**, 1154 (1926).

[7] W. F. Giauque, *A thermodynamic treatment of centain magentic effects. a proposed method of producing temperature considerably below 1° absolute,* J. Am. Chem. Soc. **49**, 1864 (1927).

[8] W. F. Giauque and D. P. MacDougall, *Attainment of temperatures below 1° absolute by demagnetization of $Gd_2(SO_4)_3 \cdot 8H_2O$,* Phys. Rev. **43**, 768 (1933).

[9] O. Tegus, E. Brück, K. H. J. Buschow, and F. R. de Boer, *Transition-metal-based magnetic regrigerants for room-temperature applications,* Nature **415**, 150 (2002).

1

[10] O. Tegus, B. Fuquan, W. Dagula, L. Zhang, E. Brück, P. Z. Si, F. R. de Boer, and K. H. J. Buschow, *Magnetic-entropy change in $Mn_{1.1}Fe_{0.9}P_{0.7}As_{0.3-x}Ge_x$*, J. Alloys Compd. **396**, 6 (2005).

[11] D. T. Cam Thanh, E. Brück, O. Tegus, J. C. P. Klaasse, T. J. Gortenmulder, and K. H. J. Buschow, *Magnetocaloric effect in MnFe(P,Si,Ge) compounds,* J. Appl. Phys. **99**, 08Q107 (2006).

[12] W. Dagula, O. Tegus, X. W. Li, L. Song, E. Brück, D. T. Cam Thanh, F. R. de Boer, and K. H. J. Buschow, *Magnetic properties and magnetic-entropy change of $MnFeP_{0.5}As_{0.5-x}Si_x$ (x = 0-0.3) compounds,* J. Appl. Phys. **99**, 08Q105 (2006).

[13] D. T. Cam Thanh, E. Brück, N. T. Trung, J. C. P. Klaasse, K. H. J. Buschow, Z. Q. Ou, O. Tegus, and L. Caron, *Structure, magnetism, and magnetocaloric properties of $MnFeP_{1-x}Si_x$ compounds,* J. Appl. Phys. **103**, 07B318 (2008).

[14] N. H. Dung, L. Zhang, Z. Q. Ou, and E. Brück, *From first-order magneto-elastic to magneto-structural transition in $(Mn,Fe)_{1.95}P_{0.50}Si_{0.50}$ compounds,* Appl. Phys. Lett. **99**, 092511 (2011).

[15] N. H. Dung, Z. Q. Ou, L. Caron, L. Zhang, D. T. Cam Thanh, G. A. de Wijs, R. A. de Groot, K. H. J. Buschow, and E. Brück, *Mixed magnetism for refrigeration and energy conversion,* Adv. Energy Mater. **1**, 1215 (2011).

[16] F. Guillou, G. Porcari, H. Yibole, N. H. van Dijk, and E. Brück, *Taming the first-order transition in giant magnetocaloric materials,* Adv. Mater. **26**, 2671 (2014).

[17] V. K. Pecharsky and K. A. Gschneidner, Jr, *Giant magnetocaloric effect in $Gd_5(Si_2Ge_2)$,* Phys. Rev. Lett. **78**, 4494 (1997).

[18] F. X. Hu, B. G. Shen, J. R. Sun, Z. H. Cheng, G. H. Rao, and X. X. Zhang, *Influence of negative lattice expansion and metamagnetic transition on magnetic entropy change in the compound $LaFe_{11.4}Si_{1.6}$,* Applied Physics Letters **78**, 3675 (2001).

[19] S. Fujieda, A. Fujita, and K. Fukamichi, *Large magnetocaloric effect in $La(Fe_xSi_{1-x})_{13}$ itinerant-electron metamagnetic compounds,* Appl. Phys. Lett. **81**, 1276 (2002).

[20] H. Wada and Y. Tanabe, *Giant magnetocaloric effect of $MnAs_{1-x}Sb_x$,* Appl. Phys. Lett. **79**, 3302 (2001).

[21] N. T. Trung, V. Biharie, L. Zhang, L. Caron, K. H. J. Buschow, and E. Brück, *From single- to double-first-order magnetic phase transition in magnetocaloric $Mn_{1-x}Cr_xCoGe$ compounds,* Applied Physics Letters **96**, 162507 (2010).

[22] F. X. Hu, B. G. Shen, J. R. Sun, and G. H. Wu, *Large magnetic entropy change in a heusler alloy $Ni_{52.6}Mn_{23.1}Ga_{24.3}$ single crystal,* Phys. Rev. B **64**, 132412 (2001).

[23] T. Krenke, E. Duman, M. Acet, E. F. Wassermann, X. Moya, L. Mañosa, and A. Planes, *Inverse magnetocaloric effect in ferromagnetic Ni-Mn-Sn alloys,* Nat. Mater. **4**, 450 (2005).

[24] J. Liu, T. Gottschall, K. P. Skokov, J. D. Moore, and O. Gutfleisch, *Giant magnetocaloric effect driven by structural transitions,* Nat. Mater. **11**, 620 (2012).

[25] E. K. Liu, W. H. Wang, L. Feng, W. Zhu, G. J. Li, J. Chen, H. W. Zhang, G. H. Wu, C. B. Jiang, H. B. Xu, and F. de Boer, *Stable magnetostructural coupling with tunable magnetoresponsive effects in hexagonal ferromagnets,* Nat. Commun. **3**, 873 (2012).

[26] Z. Y. Wei, E. K. Liu, Y. Li, G. Z. Xu, X. M. Zhang, G.-D. Liu, X. K. Xi, H. W. Zhang, W. H. Wang, G. H. Wu, and X. X. Zhang, *Unprecedentedly wide curie-temperature windows as phase-transition design platform for tunable magneto-multifunctional materials,* Adv. Electron. Mater. **1**, 1500076 (2015).

[27] N. H. Dung, L. Zhang, Z. Q. Ou, L. Zhao, L. van Eijck, A. M. Mulders, M. Avdeev, E. Suard, N. H. van Dijk, and E. Brück, *High/low-moment phase transition in hexagonal Mn-Fe-P-Si compounds,* Phys. Rev. B **86**, 045134 (2012).

[28] M. Hudl, P. Nordblad, T. Björkman, O. Eriksson, L. Häggström, M. Sahlberg, Y. Andersson, E. K. Delczeg-Czirjak, and L. Vitos, *Order-disorder induced magnetic structures of $FeMnP_{0.75}Si_{0.25}$,* Phys. Rev. B **83**, 134420 (2011).

[29] D. M. Liu, Q. Z. Huang, M. Yue, J. W. Lynn, L. J. Liu, Y. Chen, Z. H. Wu, and J. X. Zhang, *Temperature, magnetic field, and pressure dependence of the crystal and magnetic structures of the magnetocaloric compound $Mn_{1.1}Fe_{0.9}(P_{0.8}Ge_{0.2})$,* Phys. Rev. B **80**, 174415 (2009).

[30] X. F. Miao, L. Caron, P. Roy, N. H. Dung, L. Zhang, W. A. Kockelmann, R. A. de Groot, N. H. van Dijk, and E. Brück, *Tuning the phase transition in transition-metal-based magnetocaloric compounds,* Phys. Rev. B **89**, 174429 (2014).

[31] X. F. Miao, L. Caron, Z. Gercsi, A. Daoud-Aladine, N. H. van Dijk, and E. Brück, *Thermal-history dependent magnetoelastic transition in (Mn,Fe)$_2$ (P,Si),* Appl. Phys. Lett. **107**, 042403 (2015).

[32] X. B. Liu, J. Ping Liu, Q. Zhang, and Z. Altounian, *Fe magnetic moment formation and exchange interaction in Fe$_2$P: a first-principles study,* Phys. Lett. A **377**, 731 (2013).

[33] E. K. Delczeg-Czirjak, L. Delczeg, M. P. J. Punkkinen, B. Johansson, O. Eriksson, and L. Vitos, *Ab initio study of structural and magnetic properties of Si-doped Fe$_2$P,* Phys. Rev. B **82**, 085103 (2010).

1

2

EXPERIMENTAL TECHNIQUES

This thesis explores the magnetoelastic coupling in the (Mn,Fe)$_2$(P,Si)-type compounds. A variety of characterization techniques are employed to reveal the structural and magnetic changes accompanied with the phase transition in (Mn,Fe)$_2$(P,Si)-type compounds. The experiment details will be discussed in this chapter.

X-ray powder diffraction monitors the structural changes associated with the phase transition. Neutron powder diffraction is, apart from detecting these crystallographic changes, also able to determine magnetic structure and resolve sublattice magnetic moment. Bulk magnetic properties can be directly characterized by isothermal and isofield magnetization measurements. Mössbauer spectroscopy detects the magnetic interaction and chemical bonding around Fe nuclei in (Mn,Fe)$_2$(P,Si) compounds. Muon-spin relaxation (μSR) technique and neutron polarization analysis reveal the development of short-range magnetic order in the paramagnetic regime.

The combination of these techniques provides insight into the magnetoelastic coupling in (Mn,Fe)$_2$(P,Si)-type compounds.
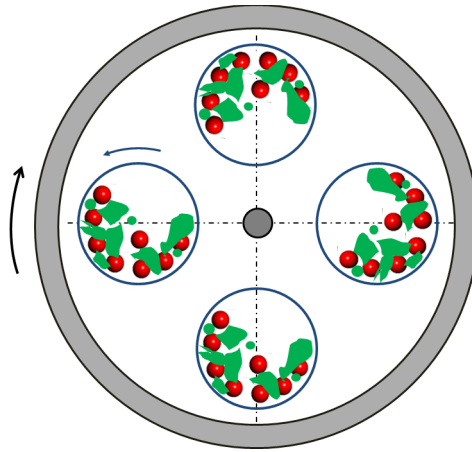
Figure 2.1: Schematic drawing of a planetary ball mill.

2.1. SAMPLE PREPARATION

2.1.1. BALL MILLING

BALL milling is a widely-used technique for mixing, homogenizing, pulverizing and mechanical alloying in material science and engineering. A planetary ball mill (PM100, Retsch) was used in the present work. As illustrated in Fig. 2.1, the grinding jar is arranged eccentrically on the sun wheel of the planetary ball mill. The moving direction of the sun wheel is opposite to that of the grinding jars. The grinding balls in the grinding jars are subjected to superimposed rotational movements. The relative motion between the balls and the grinding jar produces both frictional and impact forces, which releases a high dynamic energy.

The starting materials Fe, Mn, red-P, Fe_3N, Si, B, C (graphite) powders were grinded in tungsten-carbide jars (V ≈ 380 ml) with tungsten-carbide balls (m ≈ 8 g) under argon atmosphere. A ball-milling time of 10 hours and rotation speed of 360 rpm, which had been optimized previously, were used for the present work.

2.1.2. MELT SPINNING

MELT spinning technique is commonly used for rapid cooling of liquids. The cooling rates applied for melt spinning are of the order of 10^4 - 10^7 K/s [1]. As a result, this technique is generally used to develop materials that require extremely high solidification rates, such as metallic glasses. As illustrated in Fig. 2.2, the metal (A) is melted by induction coils (I) and pushed by gas pressure (P). The jet goes through a small nozzle in the crucible (B) over the spinning copper wheel (C), where it is rapidly cooled to form a solid ribbon (D).
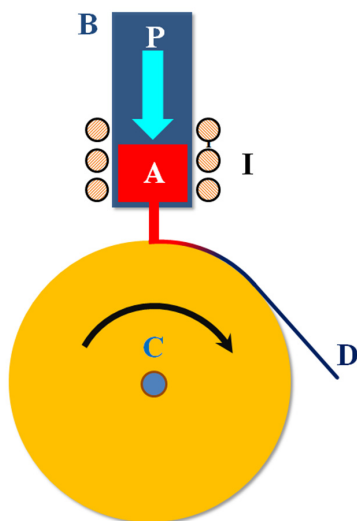
Figure 2.2: Schematic illustration of melt-spinning process. See text for details.

2

Preliminary study on C doping in $(Mn,Fe)_2(P,Si)$ compounds indicated that one can hardly get homogeneous $(Mn,Fe)_2(P,Si,C)$ samples using ball milling. The melt-spinning technique, in which the sample is obtained from a molten state, was used to prepare the $(Mn,Fe)_2(P,Si,C)$ samples (*Chapter 4*) since a high diffusion and reaction rate is expected in the molten state. The melt spinner used in the present study is produced by Edmund Bühler GmbH. The surface velocity of the copper wheel was about 45 m/s. About 5 g of sample can be obtained in a single run.

2.1.3. ANNEALING

THE fine powders obtained after ball milling were pressed into tablets and sealed in quartz ampoules in an Ar atmosphere of 200 mbar. The sealed samples were sintered at 1373 K for 2 h and annealed at 1123 K for 20 h before being oven cooled to room temperature. To improve the homogeneity of ball-milled samples, the annealed samples were heated up to 1373 K again and kept for 20 h before being quenched into water.

The ribbons or flakes prepared by melt spinning were also sealed in quartz ampoules in an Ar atmosphere of 200 mbar. The sealed samples were sintered at 1373 K for 2 h before being quenched into water.

2.2. STRUCTURE CHARACTERIZATION

2.2.1. X-RAY DIFFRACTION

THE X-ray diffraction patterns presented in *Chapter 6* were collected on a Bruker D8 diffractometer at Uppsala University, Sweden. This diffractometer is equipped with a Våntec position-sensitive detector (PSD) using Cu $K_{\alpha1}$ radiation. Measurements were performed in a temperature range from 16 to 300 K using an Oxford PheniX cryostat in a 2θ range of 20 - 90°.

The in-field X-ray diffraction patterns presented in *Chapter 7* were measured on an X-ray diffractometer [2] in the High Field Laboratory for Superconducting Materials, Institute for Materials Research at Tohoku University, Japan. This diffractometer consists of an X-ray source (Cu K_{α} radiation), a detector for the diffracted beam, a cryocooled split-pair superconducting magnet system, and a sample cryostat. The measurements were performed between 10 and 300 K in magnetic fields up to 5 T.

2.2.2. NEUTRON DIFFRACTION

X-RAY diffraction is based on the scattering of incident X-rays by electrons. As a result, it can hardly detect light atoms with a small amount of electrons or distinguish neighboring atoms with a small difference in the number of electrons. Alternatively, neutron diffraction allows for a determination of the occupation of light atoms (e.g., B, C, N) in the structure. It is also able to distinguish Mn from Fe, and P from Si, which provides more structural details for the $(Mn,Fe)_2(P,Si)$-type compounds. Additionally, neutron diffraction can be used to determine the magnetic structure and the sublattice magnetic moment.

The neutron diffraction data presented in *Chapter 3* and *Chapter 4* were recorded on the time-of-flight general materials diffractometer (GEM) [3] with six detector banks at the ISIS pulsed neutron source facility, Rutherford Appleton Laboratory, UK. The powder samples (5 - 10 g) were contained in an 8 mm diameter vanadium can, which was mounted in a cryofurnace.

The neutron diffraction experiments described in *Chapter 5* were performed on the time-of-flight high-resolution powder diffractometer (HRPD) at the ISIS pulsed neutron source facility, Rutherford Appleton Laboratory, UK. This instrument has a $\Delta d/d$ resolution of 4×10^4, which allows for an accurate study on the changes in the interplanar spacings inside the sample through the phase transition. Neutron diffraction data were obtained from the three detector banks after thermal equilibrium of the sample was reached.

The neutron diffraction experiments in *Chapter 7* were performed on the WISH [4] time-of-flight diffractometer at the ISIS pulsed neutron source facility, Rutherford Appleton Laboratory, UK. It is a long-wavelength diffractometer primarily designed for diffraction at long d-spacings with good resolution, which is

well suited for the determination of complicated magnetic structures. The powdered sample of about 6 g was put into a vanadium can mounted in a helium cryostat.

2.3. MAGNETIZATION MEASUREMENTS

MAGNETIZATION measurements in the temperature range of 5 - 370 K were carried out on a superconducting quantum interference device (SQUID) magnetometer (Quantum Design MPMS 5XL). Samples were put into a capsule, which was mounted in a plastic straw. The sweeping rate of temperature on cooling and heating was set to 2 K/min for all measurements performed in this thesis.

2.4. CALORIMETRY MEASUREMENTS

CALORIMETRY measurements were carried out on a differential scanning calorimeter (DSC, TA Instrument Q2000) equipped with a liquid nitrogen cooling system. This calorimeter allows us for a direct determination of the heat capacity with a high precision based on the so-called Tzero DSC technology. All the calorimetry data presented in this thesis were measured with a sweep rate of 10 K/min.

2.5. MÖSSBAUER SPECTROSCOPY

THE energy levels of a nucleus in an atom in a solid state are modified by the environment of the nucleus [5]. Mössbauer spectroscopy enables these energy levels to be investigated by measuring the energy difference of the resonant absorption of gamma rays. This spectroscopic technique is based on the Mössbauer effect. This effect, discovered by Rudolf Mössbauer in 1957 [6], is based on the recoil-free resonant absorption and emission of gamma rays in a solid. A Mössbauer spectrum is characterized by the number, shape, position and relative intensity of the various absorption lines. These features result from the nature of the various hyperfine interactions around the Mössbauer nuclei. A couple of hyperfine parameters (e.g., isomer shift, quadrupole splitting, magnetic hyperfine field) can be derived from the Mössbauer spectrum, which characterize the chemical bonding and magnetic interaction in materials.

The transmission ^{57}Fe Mössbauer spectra, presented in *Chapter 7*, were collected at 300 and 4.2 K with a sinusoidal velocity spectrometer using a ^{57}Co(Rh) source. The velocity calibration was carried out using an α-Fe foil. The source and the absorbing samples were kept at the same temperature during the measurements. The Mössbauer spectra were fitted using the Mosswinn 4.0 software [7].

2.6. MUON-SPIN RELAXATION (μSR) SPECTROSCOPY

A MUON is an elementary particle similar to the electron. Muons carry a positive (μ^+) or negative (μ^-) charge and a spin of 1/2. One interesting feature of the muon is that its spin is aligned antiparallel with respect to its momentum, which is due to the violation of parity involved in its production process [8].

Usually the positive muon is used for condensed matter physics research since the positive muon can be implanted into the region with large electron density, where physicists working on magnetism, superconductivity, etc. are mostly interested in. In μSR experiments, muons with an energy higher than 4 MeV are implanted into the sample. They lose energy to a few keV within 1 ns by ionization of atoms and scattering with electrons. After that, the muons experience successive electron capture and loss reactions within one picosecond, which causes the further decrease in the energy to a few hundred eV. It should be noted that all these thermalized processes are Coulombic in origin and have no effect on the spin-polarization of the muons.[9]

Since muons carry magnetic moment, they will experience Larmor precession with a frequency proportional to the strength of the local magnetic field. As a result, they behave as a local magnetometer. The large magnetic moment of the muon makes it very sensitive to extremely small magnetic fields (down to $\approx 10^{-5}$ T). Additionally, with muon it is also possible to study magnetic disorder or short-range magnetic order. Consequently, muons are well suited to study magnetism.

A muon is an unstable subatomic particle. The implanted muons will decay with a mean lifetime τ_μ of 2.2 μs. A positron is produced during the muon decay process. The decay involves a weak interaction and thus shows parity violation [8]. This phenomenon leads to a propensity for the emitted positron to emerge predominantly along the direction of the muon spin.

A schematic diagram of the μSR experimental geometry is shown in Figure 2.3. A muon is implanted into the sample. The beam direction is antiparallel to its polarization direction. If the muon decays immediately without experiencing the Larmor precession, then a positron will be generated and preferentially emitted into the backward detector. If it lives a little longer, it will have time to precess in the local field inside the sample. For instance, if it precesses for half a revolution, the emitted positron will preferentially be emitted towards the forward detector. The temporal evolution of the positron counts in the forward and backward detectors is described by the functions $N_F(t)$ and $N_B(t)$, respectively. Temporal evolution of the muon polarization can be obtained by the asymmetry function $A(t)$, given by

$$A(t) = \frac{N_B(t) - N_F(t)}{N_B(t) + N_F(t)} \tag{2.1}$$
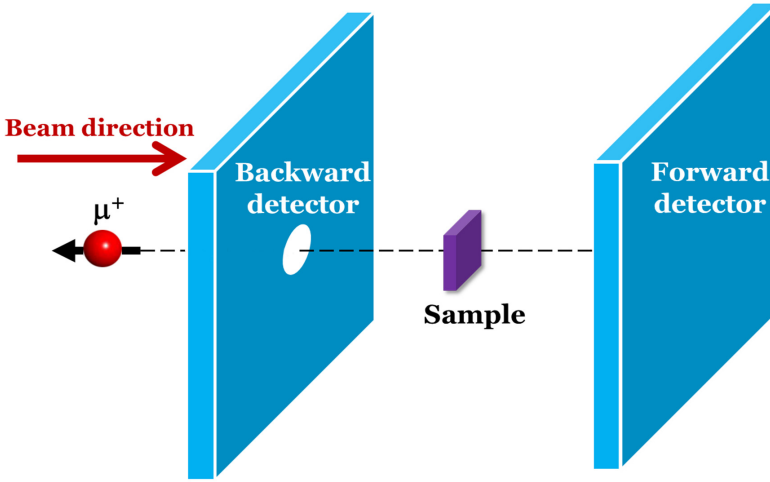
Figure 2.3: Schematic illustration of μSR setup with zero-field geometry.

2

If all the muon spins precess in the same static local field B_{loc}, then according to the Larmor equation, the static asymmetry function, $A^{stat}(t)$ would be

$$A^{stat}(t) = A_0 \left[cos^2\theta + sin^2\theta cos(\gamma_\mu B_{loc} t) \right] \tag{2.2}$$

where A_0 is the initial asymmetry, γ_μ is the gyromagnetic ratio of muon (8.51616×10^8 rad·s^{-1}T^{-1}), and θ is the angle between the muon spin direction and the local magnetic field direction.[10]

For a material in a magnetically disordered state without external field, the local magnetic field is usually considered to be randomly oriented. The resultant asymmetry function would be a spatial average of Eq. 2.2,

$$A^{stat}(t) = A_0 \left[\frac{1}{3} + \frac{2}{3} cos(\gamma_\mu B_{loc} t) \right] \tag{2.3}$$

In the zero-field μSR geometry, if the strength of the static local magnetic field is assumed to show a Gaussian distribution, the muon-spin relaxation function is described by the so-called Kubo-Toyabe function [10–13]

$$A^{stat}(t) = A_0 \left[\frac{1}{3} + \frac{2}{3}(1 - \gamma_\mu^2\Delta^2 t^2) \exp\left(\frac{-\gamma_\mu^2\Delta^2 t^2}{2} \right) \right] \tag{2.4}$$

where Δ is the standard deviation of the Gaussian field distribution.

Muon diffusion and the fluctuations of the local field will cause dynamics of the muon-spin relaxation. This can be evaluated within the framework of the

strong collision model [10–13]. In the slow dynamic limit, the muon-spin relaxation is derived as [10–13]

$$A^{dyn}(t) = A_0 \left[\frac{1}{3} \exp\left(-\frac{2}{3}\nu t\right) + \frac{2}{3}\left(1 - \gamma_\mu^2 \Delta^2 t^2\right) \exp\left(\frac{-\gamma_\mu^2 \Delta^2 t^2}{2}\right) \right] \qquad (2.5)$$

where ν is the local-field correlation frequency due to the muon diffusion and the local-field fluctuations. In the fast dynamic limit, the muon-spin relaxation function is written as [10–13]

$$A^{dyn}(t) = A_0 \exp(-\lambda t) \qquad (2.6)$$

where λ is the muon-spin relaxation rate.

Consequently, the μSR technique is well suited to studying spin dynamics in the PM regime of the $(Mn,Fe)_2(P,Si)$-type compounds. Our μSR experiments were carried out on the general purpose surface-muon instrument (GPS) at the Swiss muon source (SμS) at the Paul Scherrer Institute (PSI), Switzerland.

2.7. POLARIZED NEUTRON DIFFRACTION

Neutron polarization analysis is able to unambiguously separate the magnetic scattering cross section from nuclear coherent and nuclear spin-incoherent contributions, which has been widely used to study magnetic short-range order in materials [14, 15].

The total differential scattering cross section $\left(\frac{d\sigma}{d\Omega}\right)_{total}$ measured in a neutron scattering experiment is a sum of three distinguishable contributions:

$$\left(\frac{d\sigma}{d\Omega}\right)_{total} = \left(\frac{d\sigma}{d\Omega}\right)_{nuc} + \left(\frac{d\sigma}{d\Omega}\right)_{si} + \left(\frac{d\sigma}{d\Omega}\right)_{mag} \qquad (2.7)$$

where the $\left(\frac{d\sigma}{d\Omega}\right)_{nuc}$ is the sum of the nuclear coherent and isotope incoherent cross sections, which has no effect on the neutron spin. The $\left(\frac{d\sigma}{d\Omega}\right)_{si}$ is the nuclear spin-incoherent cross section, which has a probability of 2/3 to flip the neutron spin. The $\left(\frac{d\sigma}{d\Omega}\right)_{mag}$ is the magnetic cross section, which only detects the Fourier component of the magnetization perpendicular to the scattering vector Q. The magnetic scattering may or may not flip the neutron spin, depending on the relative direction between the neutron spin and the magnetization. When the neutron spin is perpendicular to the Fourier component of the magnetization, it will be flipped. When they are parallel to each other, the neutron spin is not flipped. Consequently, the three scattering contributions can be unambiguously separated.

xyz neutron polarization experiments were performed on the D7 diffuse scattering diffractometer [14] at the Institut Laue-Langevin (ILL), with an incident neutron wavelength of 3.12 Å. The powder samples ($\approx$ 10 grams) were put into an aluminum hollow cylinder. Six spin-dependent scattering cross sections were measured for xyz polarization analysis between 150 K $\leqslant T \leqslant$ 500 K. The scattering cross sections were integrated for energy transfers ranging from about -10 to 8.5 meV. The instrument-dependent background was estimated from measurements of an empty sample can and a cadmium sample. Amorphous quartz was measured to establish the polarization efficiency for D7. Vanadium was measured to calibrate the detector efficiencies and to allow the scattering cross sections from the samples to be expressed in absolute units.

A schematic illustration of the neutron polarization analysis is shown in Fig. 2.4. The incident neutron beam is polarized using a focusing Schärpf super-mirror bender. During a non-spin-flip experiment (see Fig. 2.4(a)), the flipper is off. The interaction between neutron and the sample may or may not influence the neutron spin, depending on the different scattering contributions, as discussed above. Only the non-spin flipped neutrons can pass through the analyzer. As a result, the measured scattering cross-section on the detectors is a sum of scattering processes that do not flip the neutron spin. During a spin-flip experiment (see Fig. 2.4(b)), the flipper is on and the measured scattering cross-section is a sum of contributions that flip the neutron spin.

Figure 2.5 shows the geometry of the xyz-polarization analysis experiment on the D7 diffuse scattering diffractometer [14], which has a planar multi-detector in the xy plane. As a result, the incident and scattered neutron wavevectors k_i and k_f and also the scattering vector Q are all constrained to lie in the xy plane. During the experiment, the incident polarization is oriented alternately along the orthogonal x, y and z directions. For each polarization experiment, the non-spin-flip and spin-flip cross sections are measured. The non-spin-flip $\left(\frac{d\sigma}{d\Omega}\right)^{NSF}$ and spin-flip $\left(\frac{d\sigma}{d\Omega}\right)^{SF}$ cross sections for an xyz-polarization analysis measurement can be expressed as [14–16]:

$$\left(\frac{d\sigma}{d\Omega}\right)_x^{NSF} = \frac{1}{2}\sin^2\alpha\left(\frac{d\sigma}{d\Omega}\right)_{mag} + \frac{1}{3}\left(\frac{d\sigma}{d\Omega}\right)_{si} + \left(\frac{d\sigma}{d\Omega}\right)_{nuc} \tag{2.8}$$

$$\left(\frac{d\sigma}{d\Omega}\right)_x^{SF} = \frac{1}{2}\left(1+\cos^2\alpha\right)\left(\frac{d\sigma}{d\Omega}\right)_{mag} + \frac{2}{3}\left(\frac{d\sigma}{d\Omega}\right)_{si} \tag{2.9}$$

$$\left(\frac{d\sigma}{d\Omega}\right)_y^{NSF} = \frac{1}{2}\cos^2\alpha\left(\frac{d\sigma}{d\Omega}\right)_{mag} + \frac{1}{3}\left(\frac{d\sigma}{d\Omega}\right)_{si} + \left(\frac{d\sigma}{d\Omega}\right)_{nuc} \tag{2.10}$$
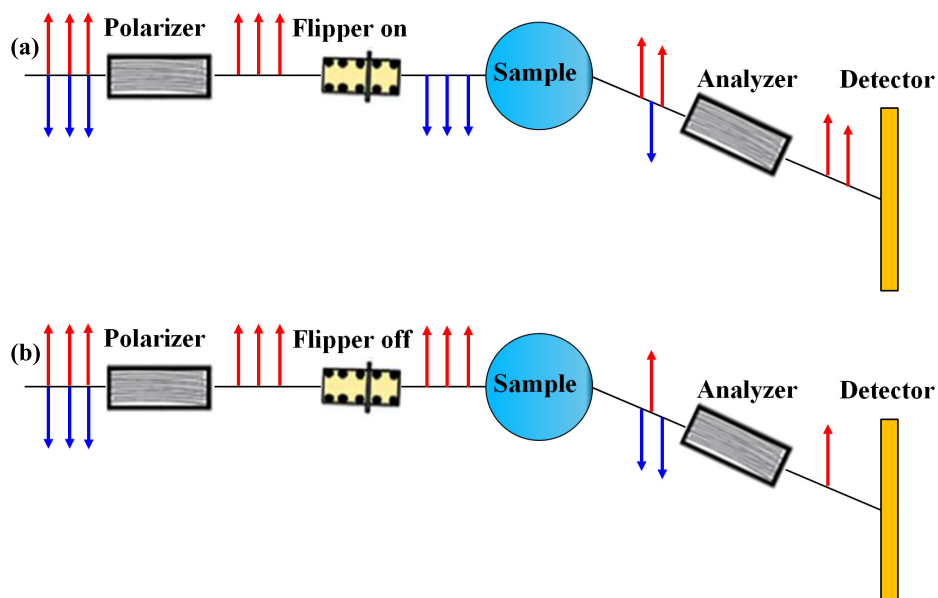
Figure 2.4: Schematic illustration of the non-spin-flip (a) and spin-flip (b) experiments.

Figure 2.5: The geometry of the xyz-polarization analysis experiment on D7 at ILL [14]. The incident polarization is oriented alternately along the orthogonal x, y and z directions. The Schärpf angle, α, is the angle between the scattering vector, Q, and the arbitrarily positioned x axis.

$$\left(\frac{d\sigma}{d\Omega}\right)_y^{SF} = \frac{1}{2}\left(1 + \sin^2\alpha\right)\left(\frac{d\sigma}{d\Omega}\right)_{mag} + \frac{2}{3}\left(\frac{d\sigma}{d\Omega}\right)_{si} \qquad (2.11)$$

$$\left(\frac{d\sigma}{d\Omega}\right)_z^{NSF} = \frac{1}{2}\left(\frac{d\sigma}{d\Omega}\right)_{mag} + \frac{1}{3}\left(\frac{d\sigma}{d\Omega}\right)_{si} + \left(\frac{d\sigma}{d\Omega}\right)_{nuc} \qquad (2.12)$$
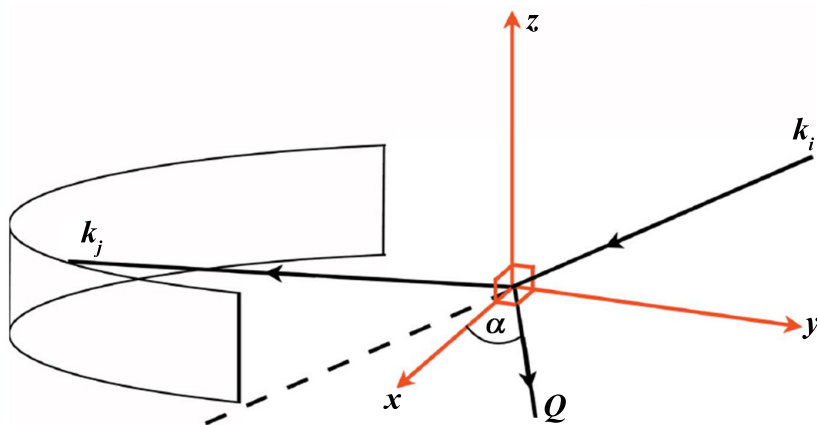
$$\left(\frac{d\sigma}{d\Omega}\right)_z^{SF} = \frac{1}{2}\left(\frac{d\sigma}{d\Omega}\right)_{mag} + \frac{2}{3}\left(\frac{d\sigma}{d\Omega}\right)_{si} \qquad (2.13)$$

The magnetic cross section can independently be calculated in two ways from the above equations:

$$\frac{d\sigma}{d\Omega}_{mag} = 2\left[\left(\frac{d\sigma}{d\Omega}\right)_x^{SF} + \left(\frac{d\sigma}{d\Omega}\right)_y^{SF}\right] - 4\left(\frac{d\sigma}{d\Omega}\right)_z^{SF} \qquad (2.14)$$

or

$$\frac{d\sigma}{d\Omega}_{mag} = 4\left(\frac{d\sigma}{d\Omega}\right)_z^{NSF} - 2\left[\left(\frac{d\sigma}{d\Omega}\right)_x^{NSF} + \left(\frac{d\sigma}{d\Omega}\right)_y^{NSF}\right] \qquad (2.15)$$

The nuclear and the spin-incoherent cross sections can be derived as

$$\frac{d\sigma}{d\Omega}_{nuc} = \frac{1}{6}\left[2\left(\frac{d\sigma}{d\Omega}\right)_{total}^{NSF} - \left(\frac{d\sigma}{d\Omega}\right)_{total}^{SF}\right] \qquad (2.16)$$

$$\frac{d\sigma}{d\Omega}_{si} = \frac{1}{2}\left(\frac{d\sigma}{d\Omega}\right)_{total}^{SF} - \frac{d\sigma}{d\Omega}_{mag} \qquad (2.17)$$

Consequently, the nuclear coherent and isotope incoherent cross sections, magnetic cross section, and spin-incoherent cross section can unambiguously be separated using the six xyz-polarization analysis experiments.

REFERENCES

[1] R. W. Cahn, *Physical Metallurgy*, 3rd ed. (Elsevier Science Publisher B.V., 1983).

[2] K. Watanabe, Y. Watanabe, S. Awaji, M. Fujiwara, N. Kobayashi, and T. Hasebe, *X-ray diffraction investigation in high fields at low temperature for $Nd_{0.5}Sr_{0.5}MnO_3$*, in *Advances in Cryogenic Engineering Materials*, Advances in Cryogenic Engineering, Vol. 44, edited by U. B. Balachandran, D. G. Gubser, K. T. Hartwig, R. P. Reed, W. H. Warnes, and V. A. Bardos (Springer US, 1998) Chap. 98, pp. 747–752.

[3] W. G. Williams, R. M. Ibberson, P. Day, and J. E. Enderby, *GEM - General materials diffractometer at ISIS,* Physica B **241–243**, 234 (1997).

[4] L. C. Chapon, P. Manuel, P. G. Radaelli, C. Benson, L. Perrott, S. Ansell, N. J. Rhodes, D. Raspino, D. Duxbury, E. Spill, and J. Norris, *Wish: the new powder and single crystal magnetic diffractometer on the second target station,* Neutron News **22**, 22 (2011).

[5] D. P. E. Dickson and F. J. Berry, *Mössbauer spectroscopy* (Cambridge University Press, New York, 1986).

[6] R. L. Mössbauer, *Kernresonanzabsorption von gammastrahlung in Ir^{191},* Naturwissenschaften **45**, 538 (1958).

[7] Z. Klencsár, *Mössbauer spectrum analysis by evolution algorithm,* Nucl. Instr. and Meth. in Phys. Res. B **129**, 527 (1997).

[8] R. L. Garwin, G. Gidal, L. M. Lederman, and M. Weinrich, *Space properties of the π meson,* Phys. Rev. **108**, 1589 (1957).

[9] S. J. Blundell, *Spin-polarized muons in condensed matter physics,* Contemp. Phys. **40**, 175 (1999).

[10] R. S. Hayano, Y. J. Uemura, J. Imazato, N. Nishida, T. Yamazaki, and R. Kubo, *Zero- and low-field spin relaxation studied by positive muons,* Phys. Rev. B **20**, 850 (1979).

[11] A. Keren, *Generalization of the abragam relaxation function to a longitudinal field,* Phys. Rev. B **50**, 10039 (1994).

[12] P. Dalmas de Réotier and A. Yaouanc, *Quantum calculation of the muon depolarization function: effect of spin dynamics in nuclear dipole systems,* J. Phys.: Condens. Matter **4**, 4533 (1992).

[13] A. Yaouanc and P. Dalmas de Réotier, *Muon spin rotation, relaxation, and resonance: applications to condensed matter,* International Series of Monographs on Physics (Oxford University Press, New York, 2011).

[14] J. R. Stewart, P. P. Deen, K. H. Andersen, H. Schober, J. F. Barthélémy, J. M. Hillier, A. P. Murani, T. Hayes, and B. Lindenau, *Disordered materials studied using neutron polarization analysis on the multi-detector spectrometer, D7,* J. Appl. Cryst. **42**, 69 (2009).

2

[15] G. Ehlers, J. R. Stewart, A. R. Wildes, P. P. Deen, and K. H. Andersen, *Generalization of the classical xyz-polarization analysis technique to out-of-plane and inelastic scattering,* Rev. Sci. Instrum. **84**, 093901 (2013).

[16] O. Schärpf and H. Capellmann, *The xyz-difference method with polarized neutrons and the separation of coherent, spin incoherent, and magnetic scattering cross sections in a multidetector,* Phys. Stat. Sol. (a) **135**, 359 (1993).

2

3

TUNING THE MAGNETOELASTIC TRANSITION IN $(\text{MN},\text{FE})_2(\text{P},\text{SI})$ COMPOUNDS BY P/SI RATIO

Neutron diffraction experiments on the (Mn,Fe)$_2$(P,Si)-type compounds reveal a site preference of Si atoms in the hexagonal structure. The degree of ordering for Si atoms depends on the Si/P ratio, while it is independent of the Mn/Fe ratio. The ferromagnetic-paramagnetic magnetoelastic transition is closely related to the size of the magnetic moment on the 3f site. A preferred occupation of Si atoms on the 2c site stabilizes and decreases the magnetic moment on the 3f and 3g site, respectively, which is supported by the first-principle density function theory calculations. This effect, together with the contribution from the Si substitution-induced changes in the interatomic distances, leads to a phase transition that is tuneable in temperature and degree of first order in Mn$_{1.25}$Fe$_{0.70}$P$_{1-x}$Si$_x$ compounds. These results provide us with further insight into the relationship between the magnetoelastic phase transition and the local atomic coordination.
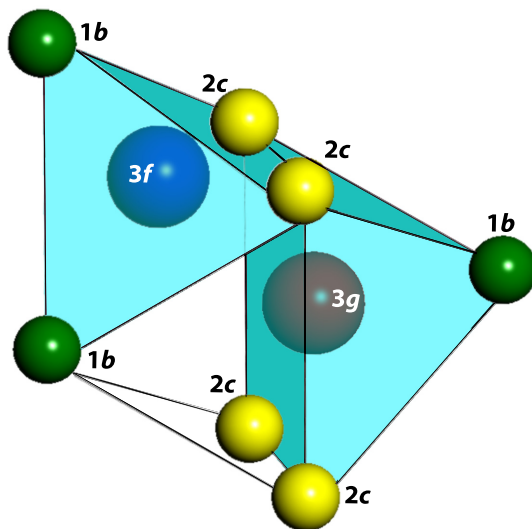
Figure 3.1: Schematic representation of $(Mn,Fe)_2(P,Si)$ crystal structure.

3

3.1. INTRODUCTION

T HE giant magnetocaloric effect (GMCE), associated with a first-order magnetoelastic transition, makes near room-temperature magnetic refrigeration attractive as a highly efficient and environment-benign cooling technology [1–6]. The evolution of $(Mn,Fe)_2(P,Si)$ compounds from the Fe_2P parent phase by partially substituting Mn for Fe and Si for P brings tunable phase transition temperatures and GMCE [7–9]. Neutron diffraction experiments and first-principle calculations indicate the preferential occupation of the two transition metal atoms in the hexagonal structure (space group $P\bar{6}2m$) [10–13]. Mn prefers the $3g$ site with five nonmetal nearest neighbours forming a square pyramid, while Fe favors the $3f$ site surrounded by four nonmetal coordination atoms forming a tetrahedron (see Figure 3.1). Strong and weak magnetism appears on the $3g$ and $3f$ site respectively as a consequence of the different coordination environments.

The site preference of the nonmetal substitution atoms in Fe_2P can be estimated based on the atomic radii [14]. Nonmetal atoms with a larger radius than P (e.g., As and Si) are expected to occupy the $2c$ site, while those having a smaller radius (e.g., B) prefer the $1b$ site. This prediction has been experimentally confirmed in Fe_2P by X-ray diffraction in the case of As substitution [15] and by Mössbauer spectroscopy for B substitution [16]. However, no experimental confirmation of the Si site preference in $Fe_2(P,Si)$-type compounds was found.

The first-order magnetoelastic transition in Fe_2P-type compounds is accompanied by changes in the density of states (DOS) of the transition-metal $3d$ electrons [9, 17, 18]. Mössbauer spectroscopy shows that Si substitution for P in Fe_2P changes the local electronic structure and hyperfine fields of its coplanar Fe atoms [19]. Theoretical calculations in the $(Mn,Fe)_2(P,Si)$ yield higher Fe (Mn) moments when a larger number of coplanar Si nearest neighbors is considered [13]. The interatomic distances also significantly influence the chemical bonding between nearest neighbours, leading to changes in the transition-metal band structure and therefore magnetic moment [10, 18]. In addition, magnetization measurements reveal that the ferromagnetic(FM)-paramagnetic(PM) phase transition temperature (T_C) increases with increasing Si content in $(Mn,Fe)_2(P,Si)$ compounds [8]. This implies that the FM state is stabilized by Si substitution. Consequently, it is necessary to resolve the underlying relation between the tunable phase transition and the changes in local coordination environment around transition metals in the Fe_2P-type compounds upon nonmetal substitution.

In this chapter, temperature-dependent neutron diffraction experiments were performed to monitor the evolution of local magnetic moments and interatomic distances across the FM-PM phase transition in $(Mn,Fe)_2(P,Si)$ compounds. Particular attention is paid to the site preference of Si atoms and its influence on local magnetic moments. Composition specific density function theory (DFT) calculations were performed by Roy and de Groot to verify the experimental results. The influence of Si substitution on phase transition is discussed on the basis of Si site preference and interatomic distances.

3.2. EXPERIMENTAL

T HE $Mn_{1.25}Fe_{0.70}P_{1-x}Si_x$ (x = 0.45, 0.50 and 0.55) compounds were prepared as described in *Chapter 2*. Magnetic characterization was performed using the reciprocating sample option mode (RSO) in a superconducting quantum interference device (SQUID) magnetometer (Quantum Design MPMS 5XL). Calorimetry measurements were performed using a commercial Differential Scanning Calorimeter (TA Instruments Q2000).

In situ time-of-flight neutron powder diffraction was measured on the General Materials Diffractometer (GEM) at the ISIS pulsed neutron source facility, Rutherford Appleton Laboratory, UK. The sample as coarse powder (about 7 g) was contained in an 8 mm diameter vanadium can, which was mounted in a cryofurnace. The diffraction data were collected continuously from six banks during the heating process. The heating rate was about 1 K/min. The temperature ranges were: from 10 to 260 K for the x = 0.45 sample, from 160 to 300 K for the x = 0.50 sample and from 10 to 375 K for the x = 0.55 sample. Nuclear and magnetic structure refinement of the neutron diffraction patterns were performed using
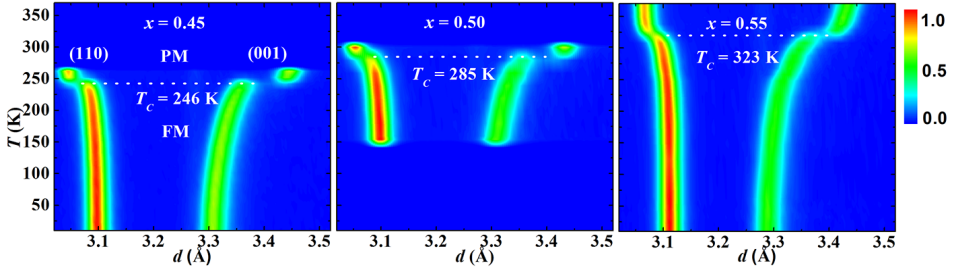
Figure 3.2: Contour plots of neutron diffraction patterns for $Mn_{1.25}Fe_{0.70}P_{1-x}Si_x$. The bar on the right represents the normalised intensity scale.

Fullprof's [20] implementation of the Rietveld refinement method.

For electronic structure calculations, the Projector Augmented Wave (PAW) method implemented in the Vienna Ab-initio Simulation Package (VASP) [21] was used. Exchange interactions were taken into account using the generalized gradient approximation (GGA) by Perdew, Burke and Ernzerhof (PBE) [22]. The Brillouin zone integration was done using a gamma centered k-point mesh of $3 \times 3 \times 8$ k-points in the irreducible part of the Brillouin zone. The cutoff energy of the augmentation function was taken as 500 eV and for smearing, a Gaussian function was used. For all the calculations we relaxed the ionic positions with a force convergence of 0.001 eV/Å for all the atoms. The energy convergence criteria was set at 10^{-7} eV.

3.3. TUNABLE MAGNETOELASTIC TRANSITION

THE temperature-dependent neutron diffraction patterns are shown in Figure 3.2 for the $Mn_{1.25}Fe_{0.70}P_{1-x}Si_x$ ($x = 0.45$, 0.50 and 0.55) compounds. All compounds display a similar evolution of the unit cell parameters with increasing temperature, i.e. a contraction in the ab plane and an expansion along the c-axis. Besides, the diffraction peaks show a discontinuity at T_C. This reveals the first-order nature of the magnetoelastic transition for the $Mn_{1.25}Fe_{0.70}P_{1-x}Si_x$ compounds studied here. With increasing Si content T_C increases, while the first order character of the phase transition, manifest in the jump of the peak positions, decreases. This is consistent with magnetization and X-ray diffraction results previously obtained [8].

The specific heat was measured through the phase transition for the three samples. As presented in Figure 3.3, the thermal hysteresis is strongly reduced from 7 K to 1 K as Si content increases from 0.45 to 0.55, indicating the weakening of the first-order character of the transition. The latent heat also decreases with Si content, reflecting the decrease in the energy barrier associated with the phase
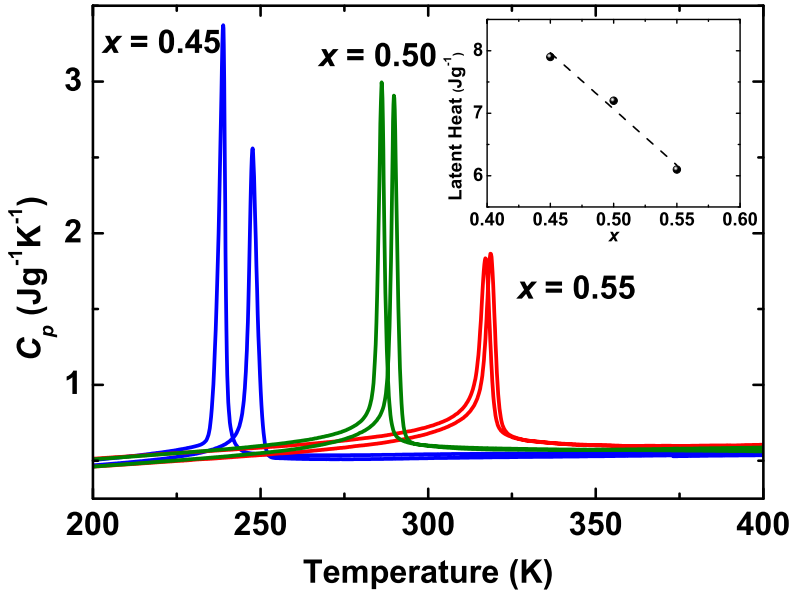
Figure 3.3: Specific heat as a function of temperature for $Mn_{1.25}Fe_{0.70}P_{1-x}Si_x$ (x = 0.45, 0.50 and 0.55). The latent heat of transition for the 3 samples is shown in the inset. The dashed line is the guide to the eye.

transition, in agreement with the thermal hysteresis trend observed. As a result, substituting Si for P stabilizes the FM state of $(Mn,Fe)_2(P,Si)$ compounds, while it weakens the first-order nature of the phase transition.
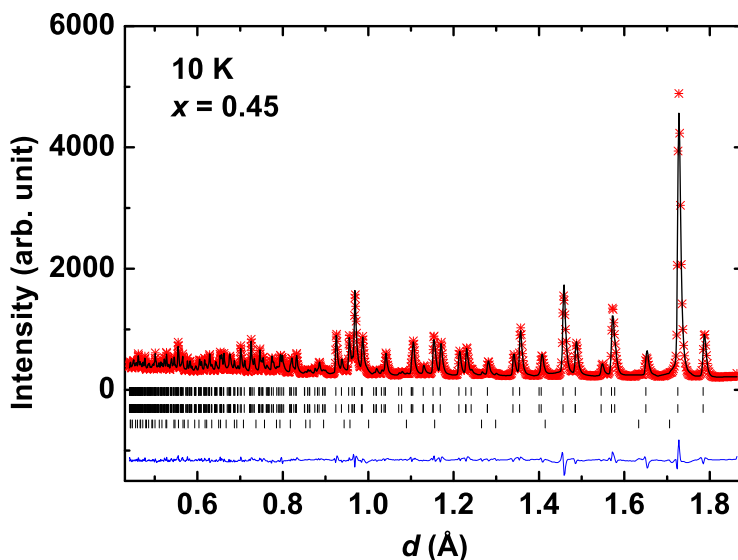
Figure 3.4: Observed and calculated neutron diffraction pattern at the GEM (detector bank 6 with $< 2\theta > \approx 154.40°$) for $Mn_{1.25}Fe_{0.70}P_{0.55}Si_{0.45}$. Vertical lines indicate the peak positions for nuclear (top) and magnetic (middle) structure of the main phase, and the impurity phase $(Mn,Fe)_3Si$ (bottom).

3.4. SITE OCCUPATION OF SI ATOMS

FIGURE 3.4 shows the neutron diffraction pattern of the $x = 0.45$ compound in the FM state as an example. A good fit is obtained for a hexagonal structure model (space group $P\bar{6}2m$) with magnetic moments within the ab plane.

The detailed structure parameters and magnetic moments derived from Rietveld refinements can be seen in Table 3.1. For these Mn-rich samples, the neutron diffraction results reveal a clear site preference of Mn and Fe: the $3g$ sites are completely occupied by Mn atoms, while 72% of the $3f$ sites are taken up by Fe and 28% by Mn. The observed site preference of Mn and Fe is in good agreement with literature reports [10, 12, 13].

The distribution of Si on the $2c$ and $1b$ sites was further studied. The fraction of Si on the $2c$ site with respect to the total Si content, hereafter referred to $f_{2c}(Si)$, for the $Mn_{1.25}Fe_{0.70}P_{1-x}Si_x$ compounds is plotted in Figure 3.5. For the present series of compounds, the $f_{2c}(Si)$ increases linearly with Si content. All three compounds have a $f_{2c}(Si)$ higher than expected for a random Si distribution ($f_{2c}(Si) \approx 67\%$), indicating a preferred occupation of Si on the $2c$ site rather than the $1b$ site. The Si site preference is more pronounced in the higher Si-
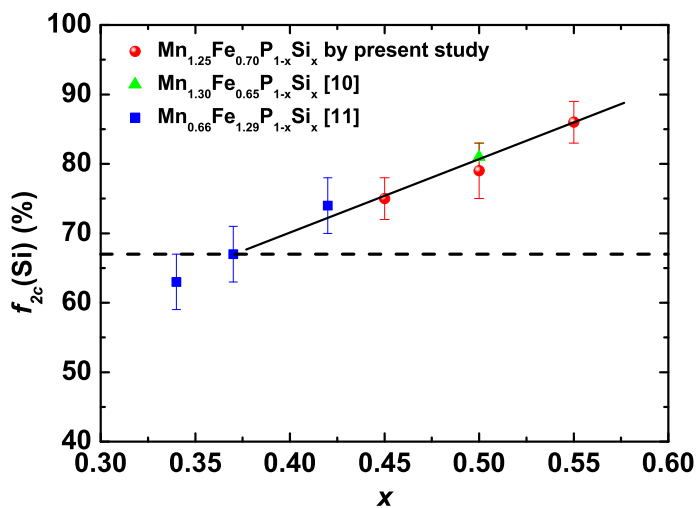
Figure 3.5: Fraction of Si on the $2c$ site in $(Mn,Fe)_2(P,Si)$ derived from neutron diffraction. The solid line is the guide to the eye. The dashed line indicates the $f_{2c}(Si)$ in the case of a random Si distribution.

3

substitution compounds. Interestingly, the $f_{2c}(Si)$ in $Mn_{0.66}Fe_{1.29}P_{1-x}Si_x$ ($x = 0.34$, 0.37 and 0.43) compounds [11] and in the $Mn_{1.30}Fe_{0.65}P_{0.50}Si_{0.50}$ compound [10] also present the same behavior (see Figure 3.5). As a result, the Si distribution is closely related to the Si content in the compounds, while it is independent of the Mn/Fe ratio.

Table 3.1: Structural parameters of $Mn_{1.25}Fe_{0.70}P_{1-x}Si_x$ (x = 0.45, 0.50 and 0.55) in the FM state. Space group: $P\bar{6}2m$. Atomic positions: $3f$ (x_1,0,0); $3g$ (x_2,0,1/2); $2c$ (1/3,2/3,0) and $1b$ (0,0,1/2). Magnetic moments: within ab plane.

	Parameters	x = 0.45(10 K)	x = 0.50(160 K)	x = 0.55(10 K)
Unit cell	a	6.1938(1)	6.1963(2)	6.2226(1)
	c	3.3063(1)	3.3091(2)	3.2894(1)
	V (Å^3)	109.845(4)	110.031(5)	110.303(5)
$3f$	x_1	0.2584(3)	0.2582(5)	0.2593(3)
	n(Fe)/n(Mn)	0.181/0.069(1)	0.177/0.073(1)	0.178/0.072(1)
	$M(\mu_B)$	1.48(8)	1.42(12)	1.57(11)
	B(Å^2)	0.30(4)	0.35(6)	0.33(5)
$3g$	x_2	0.5965(5)	0.59622(7)	0.5968(6)
	n(Mn)/n(Fe)	0.250/0	0.250/0	0.250/0
	$M(\mu_B)$	2.59(8)	2.30(11)	2.30(9)
	B(Å^2)	0.29(6)	0.62(8)	0.42(7)
$2c$	n(P)/n(Si)	0.082/0.085(4)	0.068/0.098(5)	0.048/0.118(4)
	B(Å^2)	0.17(6)	0.41(9)	0.26(9)
$1b$	n(P)/n(Si)	0.056/0.028(4)	0.057/0.027(5)	0.064/0.019(4)
	B(Å^2)	0.10(9)	0.31(13)	0.21(11)
	R_p (%)	3.61	3.65	4.08
	wR_p(%)	4.91	4.84	5.03
	χ^2	6.63	7.57	7.40

The Si distribution was also studied by first-principle DFT calculations. A $2 \times 2 \times 1$ supercell is built with lattice parameters $a = 6.223$ Å and $c = 3.289$ Å taken from the neutron diffraction experiments for $x = 0.55$. The supercell contains 15 Mn, 9 Fe, 7 Si and 5 P atoms, with a composition $Mn_{1.25}Fe_{0.75}P_{0.42}Si_{0.58}$ close to the $x = 0.55$ sample. Atomic configurations for different Si distributions on the $2c$ and $1b$ sites are modeled by filling the 8 $2c$ sites in the supercell with a different number (3, 4, 5, 6 and 7) of Si atoms. The corresponding $f_{2c}(Si)$ are 3/7, 4/7, 5/7, 6/7 and 1. The total energy as a function of the $f_{2c}(Si)$ is presented in Figure 3.6(a). The total energy decreases with increasing $f_{2c}(Si)$. This clearly reveals that Si prefers the $2c$ sites instead of the $1b$ sites, in good agreement with the experimental results and previous theoretical calculation reports [13, 23].

The site preference of Si on the $2c$ site can be understood by the non-metal atomic size factor proposed by Rundqvist [14] since Si has a larger atomic radius than P. However, this size factor is not observed in the case of As substitution in the hexagonal $(Mn,Fe)_2P_{1-x}As_x$ compounds. The substituted As atoms are statistically distributed on the $2c$ and $1b$ sites [24], although the atomic radius of As is much larger than that of P. The strong contrast of the site occupation between As and Si likely arises from their different chemical properties. As and P have the same number of valence electrons, while Si has less. Therefore, while As substitution has no effect on the electronic environment, Si induces a significant electronic reconfiguration. As a result, Si atoms prefer to occupy the lower energy $2c$ site.
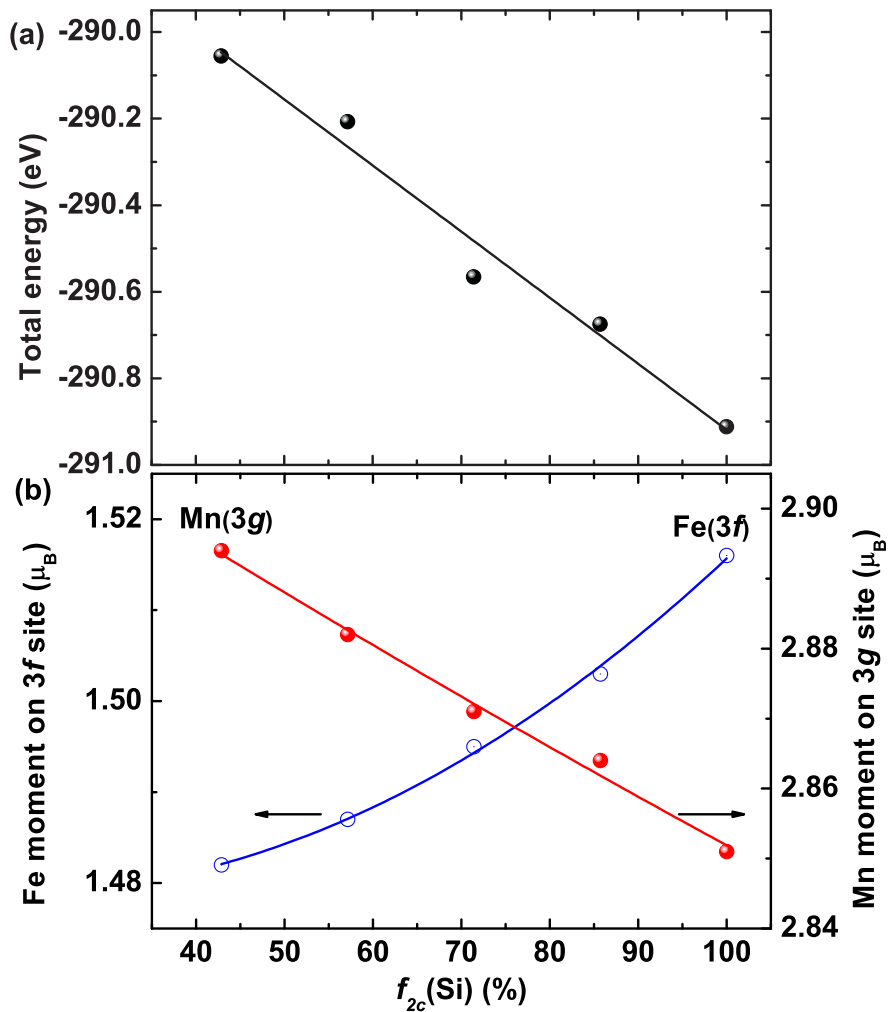
Figure 3.6: The influence of Si distribution on (a) total energy and (b) sublattice magnetic moments for $Mn_{1.25}Fe_{0.75}P_{0.42}Si_{0.58}$ from first-principle DFT calculations. The solid lines are guides to the eye.
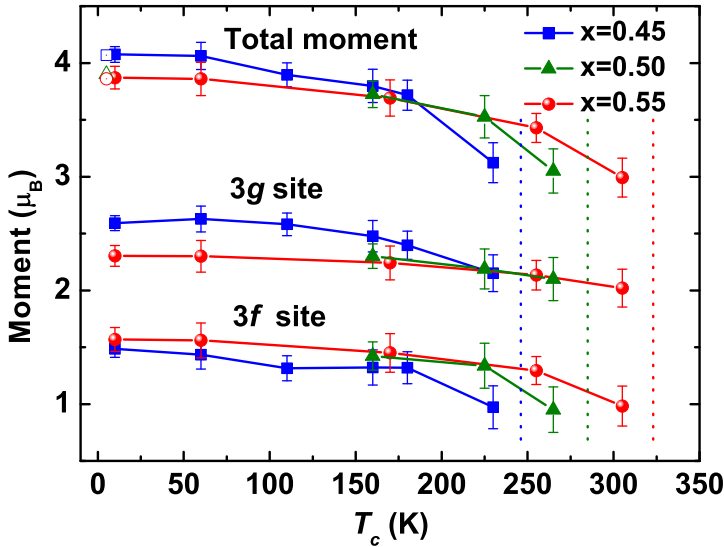
Figure 3.7: Temperature dependence of magnetic moments derived from neutron diffraction for $Mn_{1.25}Fe_{0.70}P_{1-x}Si_x$. Total magnetic moments from magnetization measurements at 5 K are also shown with the open symbols. The dotted lines indicate the position of T_C for each sample.

3

3.5. THERMAL EVOLUTION OF MAGNETIC MOMENTS

F IGURE 3.7 displays the thermal evolution of the sublattice magnetic moments derived from neutron diffraction measurements for $Mn_{1.25}Fe_{0.70}P_{1-x}Si_x$ compounds. The magnetic moment on the $3f$ site shows an increasing trend with increasing Si content, while the moment on the $3g$ site shows the opposite trend. Since the moment in the $3g$ site is roughly double that of the $3f$ site, the total moment decreases with increasing Si substitution, which is consistent with the magnetization measurements.

All compounds display a similar temperature dependence of the magnetic moments on the $3f$ and $3g$ sites. The moment on the $3g$ site is hardly influenced by increasing temperature whereas the moment on the $3f$ site drops with increasing temperature, particularly in the vicinity of T_C. Besides that, previous theoretical calculations [9] indicate that Fe moment on the $3f$ site is significantly reduced after the ferro-paramagnetic magnetoelastic transition, while Mn on the $3g$ site still carries magnetic moment of over $2\mu_B$. These results demonstrate that the magnetoelastic transition in $Mn_{1.25}Fe_{0.70}P_{1-x}Si_x$ compounds is closely linked with the drop of the magnetic moment on the $3f$ site. However, the high-moment

state of the 3f site persists to higher temperatures for the compounds containing more Si atoms. This gives us a clear evidence of the enhancement of the FM state by Si substitution for P in Mn$_{1.25}$Fe$_{0.70}$P$_{1-x}$Si$_x$ compounds. Therefore, the rise in T_C of the FM-PM transition with increasing Si content (see Figure 3.2) can be attributed to the stabilization of the magnetic moment on the 3f site.

The first-order phase transition behavior in the (Mn,Fe)$_2$(P,Si)-type compounds is closely related to the unique mixed magnetism of the system. [9, 10] The preferred occupation of Si on the 2c site causes significant electronic reconfiguration around the 3f and 3g sites, which stabilizes and decreases the magnetic moment on the 3f and 3g site, respectively. This weakens the instability of the moments on the 3f site and the strong magnetism on the 3g site. Thus, by changing Si content the electronic structure is changed, allowing us to effectively tune the mixed magnetism in the system and the phase transition character. Consequently, the site preference of Si can tune the order of phase transition while As atom, having the same number of valence electrons as P and thus being statistically distributed, cannot [25, 26].

The Fe (Mn) magnetic moment formation is in competition with chemical bonding in the Mn$_{1.25}$Fe$_{0.70}$P$_{1-x}$Si$_x$ compounds, which is strongly influenced by the coordination environment around the Fe (Mn) atoms. Two main contributions from the coordination atoms should be taken into consideration: the atomic species and the interatomic distances. Figure 3.6(b) illustrates the magnetic moments on the 3f and 3g sites as a function of f_{2c}(Si) obtained from the DFT calculations. Higher and lower magnetic moments are predicted on the 3f and 3g sites respectively when more Si atoms occupy the 2c sites. According to the electronic structure calculations, (Mn,Fe)$_2$(P,Si) has only Fe and Mn d electrons close to the Fermi level, while P and Si p electrons are located far below [13]. Electron transfer from the Fe and Mn d band to P and Si p band would be expected to fill the P and Si p band, which enhances the splitting of the Fe and Mn d band and thus increases the magnetic moment of the Fe and Mn supplying the electrons. This electron transfer feature is more pronounced for coplanar metal-nonmetal neighbors as indicated by the isomer shift in Mössbauer spectra of Fe$_2$(P,Si) compounds [19]. Since Si has less valence electrons than P, the preferred occupation of Si on the 2c site would bring larger magnetic moments on its coplanar 3f site. These results suggest that larger magnetic moments will develop on the 3f or 3g site when there are more coplanar Si nearest neighbours, which is in accordance with previous theoretical calculation results [13].
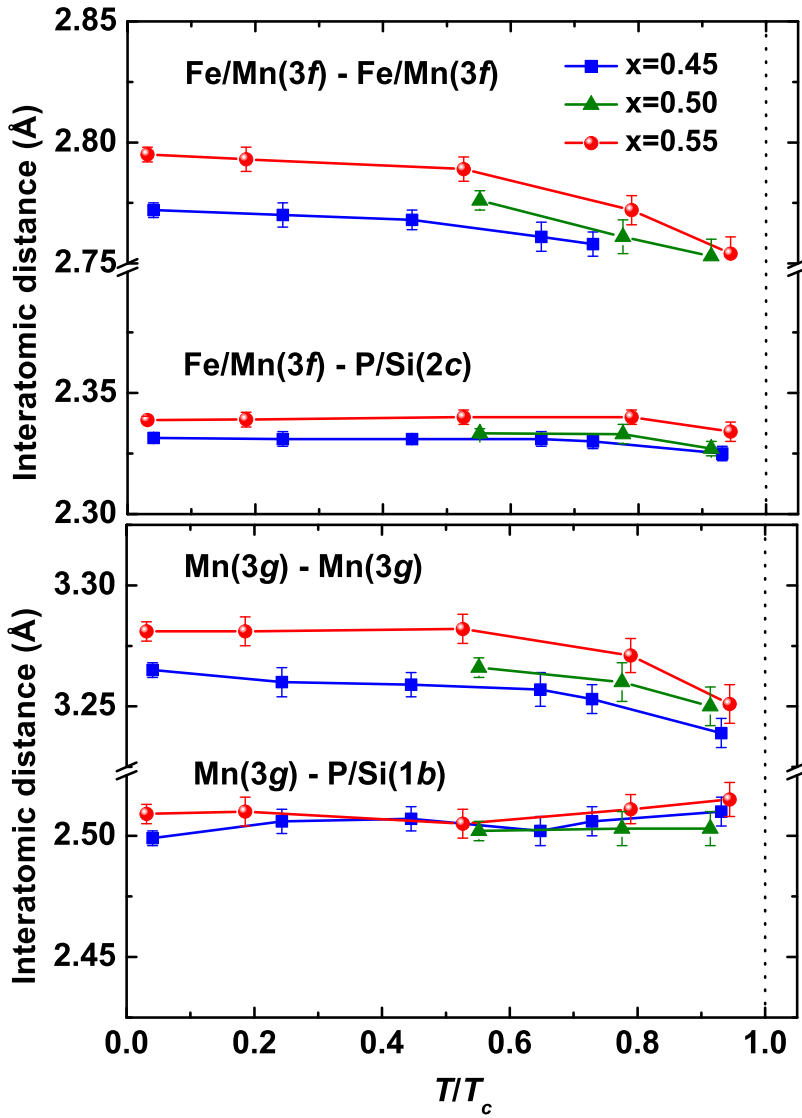
Figure 3.8: Intralayer interatomic distances as a function of temperature derived from neutron diffraction for $Mn_{1.25}Fe_{0.70}P_{1-x}Si_x$. Dotted lines indicate the position of the normalized T_C.

3.6. INTERATOMIC DISTANCES

THE interatomic distance also plays a crucial role in the competition between magnetic moment and chemical bonding. The neutron diffraction experiments reveal that compared with the interlayer interatomic distances, the intralayer interatomic distances show a much stronger dependence on temperature or Si substitution. This probably arises from the reconfiguration of electronic structure during the phase transition or upon Si substitution taking place mainly within the layer. The intralayer interatomic distances decrease with rising temperature, as shown in Figure 3.8. As a result, the magnetic moments decrease with increasing temperature due to the growing overlap of $3d$ states as well as the enhanced metal-nonmetal hybridization (see Figure 3.7). Moreover, the intralayer distances expand when more Si atoms replace P (see Figure 3.8). Larger magnetic moments, therefore, are expected on the $3f$ and $3g$ sites for the higher Si-containing compounds. This is confirmed by the neutron diffraction results for the magnetic moment on the $3f$ site (see Figure 3.7). However, the observed magnetic moment on the $3g$ site shows an unexpected decrease with increasing Si substitution although the Mn($3g$)-Mn($3g$) distance expands. Such a deviation can be understood by the increasing Si occupancy on the $2c$ site with increasing Si content, as indicated in Figure 3.5. In the higher Si-containing samples, less electron transfer occurs between the $3g$-$1b$ coplanar sites and it therefore causes less moment to develop on the $3g$ site (see Fig 3.6b). As a consequence, the changes in the sublattice magnetic moments induced by Si substitution are the results of both Si site preference and the varying interatomic distances.

3.7. CONCLUSIONS

IN summary, the thermal evolution of sublattice moment and nuclear structure in $Mn_{1.25}Fe_{0.70}P_{1-x}Si_x$ (x = 0.45, 0.50 and 0.55) have been monitored across the magnetoelastic transition by means of temperature-dependent neutron diffraction. The Si distribution on the $2c$ and $1b$ sites in the hexagonal $(Mn,Fe)_2(P,Si)$-type compounds can be predicted based on the neutron diffraction results, which is dependent on the Si/P ratio while independent of the Mn/Fe ratio. The FM-PM magnetoelastic transition is accompanied by the decrease of the magnetic moment on the $3f$ site. The clear preference of Si to occupy the $2c$ site stabilizes and decreases the magnetic moment on the $3f$ and $3g$ site, respectively, which is supported by the first-principle calculations. The intralayer interatomic distances are expanded by Si substitution, which also enhances the magnetic moments on the $3f$ sites. The phase transition with tunable degree of first order and critical temperature in $(Mn,Fe)_2(P,Si)$-type compounds is attributed to the Si site preference in combination with changing interatomic distances.

REFERENCES

[1] X. X. Zhang, J. Tejada, Y. Xin, G. F. Sun, K. W. Wong, and X. Bohigas, *Magnetocaloric effect in $La_{0.67}Ca_{0.33}MnO$ and $La_{0.60}Y_{0.07}Ca_{0.33}MnO$ bulk materials,* Appl. Phys. Lett. **69**, 3596 (1996).

[2] V. K. Pecharsky and K. A. Gschneidner, Jr, *Giant magnetocaloric effect in $Gd_5(Si_2Ge_2)$,* Phys. Rev. Lett. **78**, 4494 (1997).

[3] H. Wada and Y. Tanabe, *Giant magnetocaloric effect of $MnAs_{1-x}Sb_x$,* Appl. Phys. Lett. **79**, 3302 (2001).

[4] O. Tegus, E. Brück, K. H. J. Buschow, and F. R. de Boer, *Transition-metal-based magnetic regrigerants for room-temperature applications,* Nature **415**, 150 (2002).

[5] A. Fujita, S. Fujieda, Y. Hasegawa, and K. Fukamichi, *Itinerant-electron metamagnetic transition and large magnetocaloric effects in $La(Fe_xSi_{1-x})_{13}$ compounds and their hydrides,* Phys. Rev. B **67**, 104416 (2003).

[6] E. Brück, *Developments in magnetocaloric refrigeration,* J. Phys. D: Appl. Phys. **38**, R381 (2005).

[7] N. H. Dung, L. Zhang, Z. Q. Ou, and E. Brück, *From first-order magneto-elastic to magneto-structural transition in $(Mn,Fe)_{1.95}P_{0.50}Si_{0.50}$ compounds,* Appl. Phys. Lett. **99**, 092511 (2011).

[8] N. H. Dung, L. Zhang, Z. Q. Ou, and E. Brück, *Magnetoelastic coupling and magnetocaloric effect in hexagonal Mn-Fe-P-Si compounds,* Scripta Mater. **67**, 975 (2012).

[9] N. H. Dung, Z. Q. Ou, L. Caron, L. Zhang, D. T. Cam Thanh, G. A. de Wijs, R. A. de Groot, K. H. J. Buschow, and E. Brück, *Mixed magnetism for refrigeration and energy conversion,* Adv. Energy Mater. **1**, 1215 (2011).

[10] N. H. Dung, L. Zhang, Z. Q. Ou, L. Zhao, L. van Eijck, A. M. Mulders, M. Avdeev, E. Suard, N. H. van Dijk, and E. Brück, *High/low-moment phase transition in hexagonal Mn-Fe-P-Si compounds,* Phys. Rev. B **86**, 045134 (2012).

[11] Z. Q. Ou, L. Zhang, N. H. Dung, L. van Eijck, A. M. Mulders, M. Avdeev, N. H. van Dijk, and E. Brück, *Neutron diffraction study on the magnetic structure of Fe_2P-based $Mn_{0.66}Fe_{1.29}P_{1-x}Si_x$ melt-spun ribbons,* J. Magn. Magn. Mater. **340**, 80 (2013).

3

[12] M. Hudl, P. Nordblad, T. Björkman, O. Eriksson, L. Häggström, M. Sahlberg, Y. Andersson, E. K. Delczeg-Czirjak, and L. Vitos, *Order-disorder induced magnetic structures of FeMnP$_{0.75}$Si$_{0.25}$,* Phys. Rev. B **83**, 134420 (2011).

[13] X. B. Liu and Z. Altounian, *A first-principles study on the magnetocaloric compound MnFeP$_{2/3}$Si$_{1/3}$,* J. Appl. Phys. **105**, 07A902 (2009).

[14] S. Rundqvist, Ark. Kemi **20**, 67 (1962).

[15] A. Catalano, R. J. Arnott, and A. Wold, *Magnetic and crystallographic properties of the system Fe$_2$P$_{1-x}$As$_x$,* J. Solid State Chem. **7**, 262 (1973).

[16] R. Chandra, S. Bjarman, T. Ericsson, L. Häggström, C. Wilkinson, and R. Wäppling, *A mössbauer and X-ray study of Fe$_2$P$_{1-x}$B$_x$ compounds (x<0.15),* J. Solid State Chem. **34**, 389 (1980).

[17] X. B. Liu, J. Ping Liu, Q. Zhang, and Z. Altounian, *Fe magnetic moment formation and exchange interaction in Fe$_2$P: a first-principles study,* Phys. Lett. A **377**, 731 (2013).

[18] Z. Gercsi, E. K. Delczeg-Czirjak, L. Vitos, A. S. Wills, A. Daoud-Aladine, and K. G. Sandeman, *Magnetoelastic effects in doped Fe$_2$P,* Phys. Rev. B **88**, 024417 (2013).

[19] P. Jernberg, A. A. Yousif, L. Häggström, and Y. Andersson, *A Mössbauer study of Fe$_2$P$_{1-x}$Si$_x$ (x<0.35),* J. Solid State Chem. **53**, 313 (1984).

[20] J. Rodríguez-Carvajal, *Recent advances in magnetic structure determination by neutron powder diffraction,* Physica B **192**, 55 (1993).

[21] G. Kresse and J. Furthmüller, *Efficient iterative schemes for ab initio total-energy calculations using a plane-wave basis set,* Phys. Rev. B **54**, 11169 (1996).

[22] J. P. Perdew, K. Burke, and M. Ernzerhof, *Generalized gradient approximation made simple,* Phys. Rev. Lett. **77**, 3865 (1996).

[23] E. K. Delczeg-Czirjak, L. Delczeg, M. P. J. Punkkinen, B. Johansson, O. Eriksson, and L. Vitos, *Ab initio study of structural and magnetic properties of Si-doped Fe$_2$P,* Phys. Rev. B **82**, 085103 (2010).

[24] M. Bacmann, J. L. Soubeyroux, R. Barrett, D. Fruchart, R. Zach, S. Niziol, and R. Fruchart, *Magnetoelastic transition and antiferro-ferromagnetic ordering in the system MnFeP$_{1-y}$As$_y$,* J. Magn. Magn. Mater. **134**, 59 (1994).

3

[25] R. Hermann, O. Tegus, E. Brück, K. H. J. Buschow, F. de Boer, G. Long, and F. Grandjean, *Mössbauer spectral study of the magnetocaloric FeMnP$_{1-x}$As$_x$ compounds,* Phys. Rev. B **70**, 214425 (2004).

[26] O. Beckman and L. Lundgren, in *Handbook of Magnetic Materials,* edited by K. H. J. Buschow (North-Holland, Amsterdam, 1991), Vol. 6, pp. 181-287 .

3

4

TUNING THE MAGNETOELASTIC TRANSITION IN (MN,FE)₂(P,SI) COMPOUNDS BY B, C AND N DOPING

The magnetoelastic transition in (Mn,Fe)₂(P,Si) is tunable by doping the structure with B, C and N atoms. Neutron diffraction experiments reveal that B substitutes Si on the 1b site of the hexagonal P6̄2m structure, C occupies the interstitial 6j and 6k sites, while N distributes on both the 1b and interstitial 6j and 6k sites. The tuning mechanism has been discussed in terms of the subtle variations in electronic configuration around the Fe atoms.

4.1. INTRODUCTION

HEXAGONAL $(\text{Mn,Fe})_2(\text{P,Si})$-type compounds [1–4] are, to date, the most promising materials for refrigeration and energy conversion applications due to the combination of a giant magnetocaloric effect (GMCE) and low material costs. The GMCE in these compounds originates from a first-order magnetoelastic transition (FOMT), i.e., the ferromagnetic (FM) to paramagnetic (PM) transition is strongly coupled with a structure change [2, 5–7].

As indicated by density functional theory (DFT) calculations [2, 8, 9], the FOMT in $(\text{Mn,Fe})_2(\text{P,Si})$-type materials is associated with the electron-density redistribution around Fe atoms on the $3f$ site in the hexagonal structure. Above the ferromagnetic transition temperature T_C, the magnetic moment of Fe is reduced due to the strong electronic redistribution around the $3f$ site. In contrast, the Mn atoms occupying the $3g$ site display strong magnetism, and do not show a significant reduction in magnetic moment. The electronic configuration around the $3f$ site is highly sensitive to its chemical environment, such as the neighboring-atom species and interatomic distances [5, 10]. As a result, the critical temperature as well as the character of FOMT may be tuned through subtle changes in the atomic surroundings of the $3f$ site.

The tunability of the FOMT, triggered by subtle changes in electronic configuration, has already been demonstrated by varying the Mn/Fe and P/Si ratios in $(\text{Mn,Fe})_2(\text{P,Si})$ alloys [2, 11, 12]. Another effective way of tuning the FOMT is through B doping in $(\text{Mn,Fe})_2(\text{P,Si})$ [4], although the structural origin of the tuning by B doping is still unclear. In this chapter, it is shown that the FOMT of $(\text{Mn,Fe})_2(\text{P,Si})$ can also be tuned by doping with C and N atoms. As C and N are much cheaper than B, they are consequently more promising for large-scale commercial applications. Neutron diffraction is employed to resolve the occupancy of B, C and N dopants in the structure, which allows us to explore the relation between structural changes and the tunability of the FOMT. The variation in electronic configuration around the magnetic atoms can be used to tailor the magnetoelastic transition in many materials.

4.2. EXPERIMENTAL

SAMPLES with nominal compositions $\text{MnFe}_{0.95}\text{P}_{0.67}\text{Si}_{0.33}$ (parent compound), $\text{MnFe}_{0.95}\text{P}_{0.67}\text{Si}_{0.33}\text{B}_x$ ($x = 0.03$ and 0.06) and $\text{MnFe}_{0.95}\text{P}_{0.67}\text{Si}_{0.33}\text{N}_y$ ($y = 0.02$ and 0.06) were prepared by ball milling, as described in *Chapter 2*. $\text{MnFe}_{0.95}\text{P}_{0.67}\text{Si}_{0.33}\text{C}_z$ ($z = 0.05$ and 0.10) alloys were prepared by melt-spinning, as described in *Chapter 2*. The starting materials were Mn, Fe, P, Si, Fe_3N, C and B^{11} (isotope) powders with a purity higher than 99.9%. The concentration of C and N in the as-prepared samples were evaluated by the combustion method on

Table 4.1: The C and N concentrations in the as-prepared samples from elemental analysis.

Nominal composition	Nominal w.t.%	Measured w.t.%
$MnFe_{0.95}P_{0.67}Si_{0.33}C_{0.05}$	0.43	0.50_1
$MnFe_{0.95}P_{0.67}Si_{0.33}C_{0.10}$	0.86	0.95_1
$MnFe_{0.95}P_{0.67}Si_{0.33}N_{0.02}$	0.20	0.19_1
$MnFe_{0.95}P_{0.67}Si_{0.33}N_{0.06}$	0.60	0.55_1

a LECO elemental analyzers. The results from the elemental analysis are summarized in Table 4.1, which are in good agreement with the nominal compositions.

Magnetic properties were characterized using a superconducting quantum interference device (SQUID) magnetometer (Quantum Design MPMS 5XL). Time-of-flight powder neutron diffraction data were collected at room temperature on the General Materials Diffractometer GEM [13] at the ISIS pulsed spallation neutron source, Rutherford Appleton Laboratory, UK. For each sample, approximately 10 g of powder was loaded into an 8 mm diameter thin-walled vanadium sample can and data collected for 225 microAmp·hour proton beam current on the ISIS neutron target. Structure refinement was performed using Fullprof's implementation of the Rietveld refinement method [14] using the data collected in all 6 GEM detector banks.

4.3. TUNABLE MAGNETOELASTIC TRANSITION

FIGURE 4.1 shows the temperature-dependent magnetization of the parent and doped compounds. The samples were first cooled in an applied field of 1 T to 5 K, where the magnetization data were collected upon heating up to 350 K before cooling down again to 5 K. After that, isothermal magnetization curves were measured at 5 K for applied fields up to 5 T.

As shown in Fig. 4.1(a), a remarkable thermal hysteresis of about 76 K is apparent for the parent alloy, characteristic for the strong first-order nature of the FOMT. The thermal hysteresis is significantly reduced to 17 K by doping with 3 at.% B and to 5 K by doping with 6 at.% B. A strong increase in T_C is observed for B doping. Similar effects on the thermal hysteresis and T_C are also found upon C doping (see Fig. 4.1(c)), although the influence on the thermal hysteresis is less pronounced compared to B doping. Additionally, the saturated magnetic moment of $MnFe_{0.95}P_{0.67}Si_{0.33}$ is slightly reduced by B doping, while it is hardly influenced by C doping, as shown in Fig.4.1(b) and (d).

Compared to C and B, a striking difference in the influence on the FOMT is observed for N doping. The T_C shifts to lower temperatures upon N doping, while the thermal hysteresis increases (see Fig. 4.1(e)). Another interesting fea-

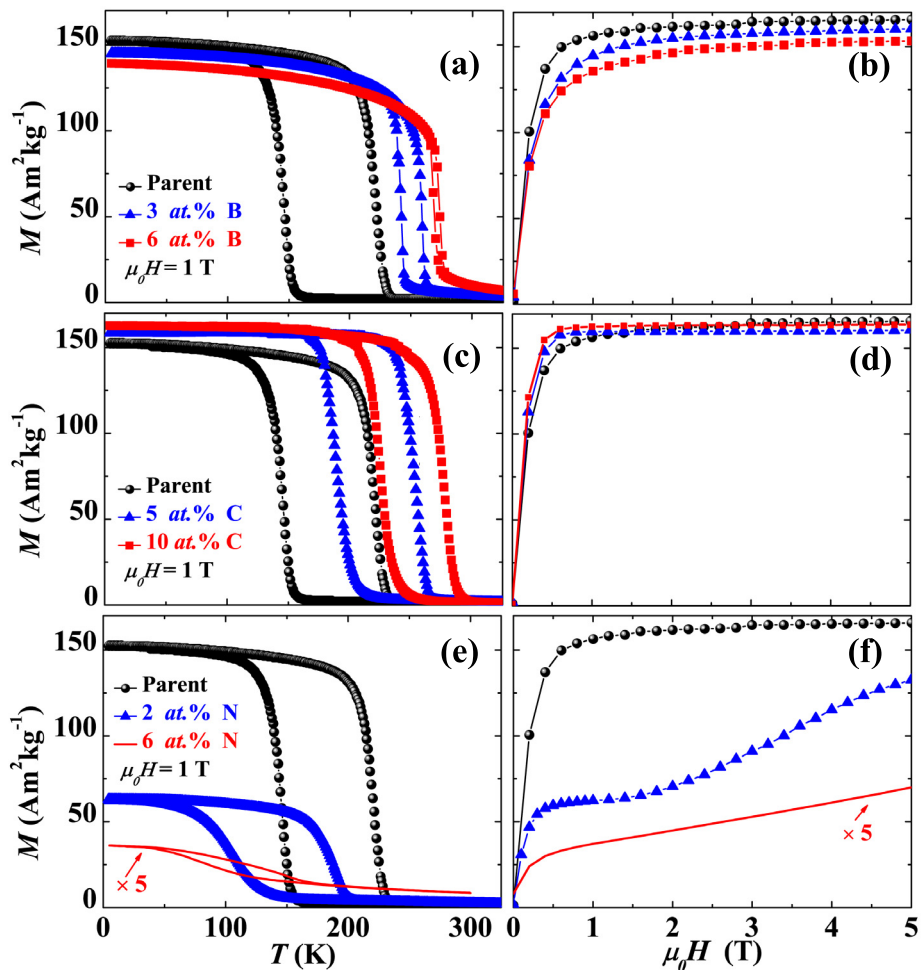Figure 4.1: Magnetization as a function of temperature for $MnFe_{0.95}P_{0.67}Si_{0.33}$ (parent compound) and for different B (a), C (b) and N (c) doping concentrations. (d-f) The corresponding isothermal magnetization curves as a function of applied field at 5 K. Note that the magnetization of the 6 at.% N-doped sample is magnified by a factor of 5 for clarity.

ture of N-doped materials is the notable drop in saturation magnetization at 5 K. The isothermal magnetization curves (see Fig. 4.1(f)) of the N-doped materials also have a different shape than the parent and B and C doped samples. Such an anomaly is due to the kinetic arrest of the FOMT, as presented in *Chapter 7*. The FOMT in $(Mn,Fe)_2(P,Si)$-type materials can be kinetically arrested under certain conditions, leading to a coexistence of a metastable spin-density wave (SDW) phase and a stable ferromagnetic phase below T_C. The rapid increase in magnetization of the 2 at.% N-doped material with increasing magnetic field, as presented in Fig. 4.1(f), is related to the metamagnetic transformation of the metastable SDW phase into the equilibrium FM phase.

4.4. Site occupation of dopant atoms

Due the strong magnetoelastic coupling in $(Mn,Fe)_2(P,Si)$-type materials, variations in T_C and the hysteresis of the PM-FM transition are the result of structural changes upon B, C and N doping. Resolving the occupation of these light dopants in the structure and its influence on the electronic state of the $3f$ site is essential to understand the resultant changes in the FOMT.

These light dopants can be well detected and distinguished from other constituents by neutron diffraction. In Fig. 4.2(a), the neutron diffraction pattern for $MnFe_{0.95}P_{0.67}Si_{0.33}C_{0.10}$ is shown as an example. The diffraction patterns from all samples could be fitted with the Fe_2P-type hexagonal structure (space group P-62m) with 4 different crystallographic sites, i.e., the $3f$ and $3g$ sites for Mn and Fe atoms and the $2c$ and $1b$ sites for P and Si atoms, respectively (see schematic illustration in Fig. 4.2(b)). Non-metal dopants may substitute P/Si on the $2c/1b$ sites, with a specific site preference (depending on the atomic radius of the dopant [15]) or occupy interstitial sites. Since B, C and N atoms have a smaller atomic radius than P and Si, the unit cell will shrink in the case of substitution, while it will expand for the occupation of interstitial sites.

The structure refinements show that B substitutes Si on the $1b$ site, while C occupies the interstitial $6j$ and $6k$ sites (illustrated in Fig. 4.2(b)). This is consistent with a contraction of the unit cell for B doping and an expansion for C doping. Previous DFT calculations show that Si prefers to occupy the $2c$ site (instead of the $1b$ site) in the hexagonal structure, which is confirmed by neutron diffraction experiments [5]. As Si atoms prefer to occupy the $2c$ site, B substitution for Si on the $1b$ site stabilizes the whole structure. The occupation of B and C dopants has also been studied in Fe_2P with the same crystal structure, where B and C are both found to occupy the $1b$ site [16, 17]. The discrepancy in site occupation for C in Fe_2P and $(Mn,Fe)_2(P,Si)$ may be attributed to the different local environment around the $1b$, $6j$ and $6k$ sites in these two materials.

4
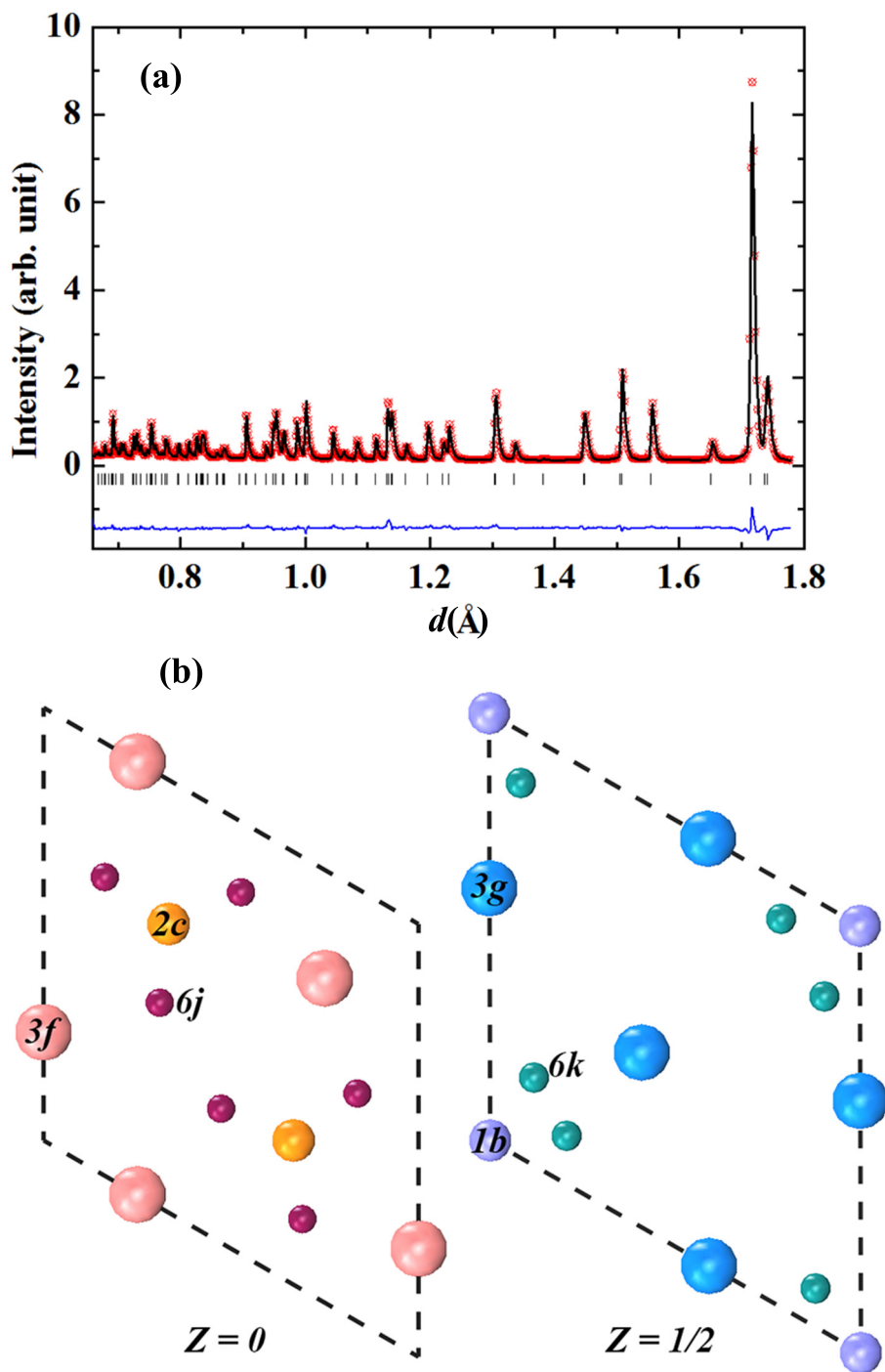
Figure 4.2: (a) Fitted powder neutron diffraction pattern for $MnFe_{0.95}P_{0.67}Si_{0.33}C_{0.10}$ collected at the GEM (detector bank 6 with $< 2\theta > \approx 154.40°$). Red circles indicate observed data points; black line indicates calculated profile; blue line indicates difference (obs-calc); vertical lines indicate Bragg peak positions. (b) Schematic representation of $(Mn,Fe)_2(P,Si)$-type structure in the basal plane at $z = 0$ and $z = 1/2$.

The structural parameters derived from the Rietveld refinement are summarized in Table 4.2. It should be noted that less than 1 wt.% of the Fe_3Si-type impurity phase is found in the samples. The distribution of Mn and Fe atoms in the hexagonal structure has not been influenced by B and C doping. For an increase in B concentration, the Si and P occupation on the $2c$ site is hardly influenced, while the amount of Si on the $1b$ site is decreased. The introduced C atoms are found to be statistically distributed over the $6j$ and $6k$ sites without changing the atomic distribution of P and Si in the structure.

Since N has a smaller atomic radius than C, one would expect that N also enters interstitial sites like C. However, the unit-cell volume remains almost unchanged after N doping, as shown in Fig. 4.3(a). About 20% of the N atoms enter the $1b$ site while the rest enters the $6k$ and $6j$ interstitial sites (see Table 4.2). The competition between the effect of interstitial and substitutional N doping makes the unit-cell volume almost constant. Fig. 4.3(b) presents the evolution of lattice parameters upon B, C and N doping. The unit cell shows a clear contraction along the c-axis and an expansion within the ab-plane upon B and C doping. However, the lattice parameters show no significant change upon N doping, which may be due to the compensating effect of the interstitial and substitutional occupation of N in the structure.

4

Figure 4.3: Lattice parameters (a) and unit-cell volume (b) as a function of the B, C and N concentration for for $MnFe_{0.95}P_{0.67}Si_{0.33}$. Solid lines are a guide to the eye.
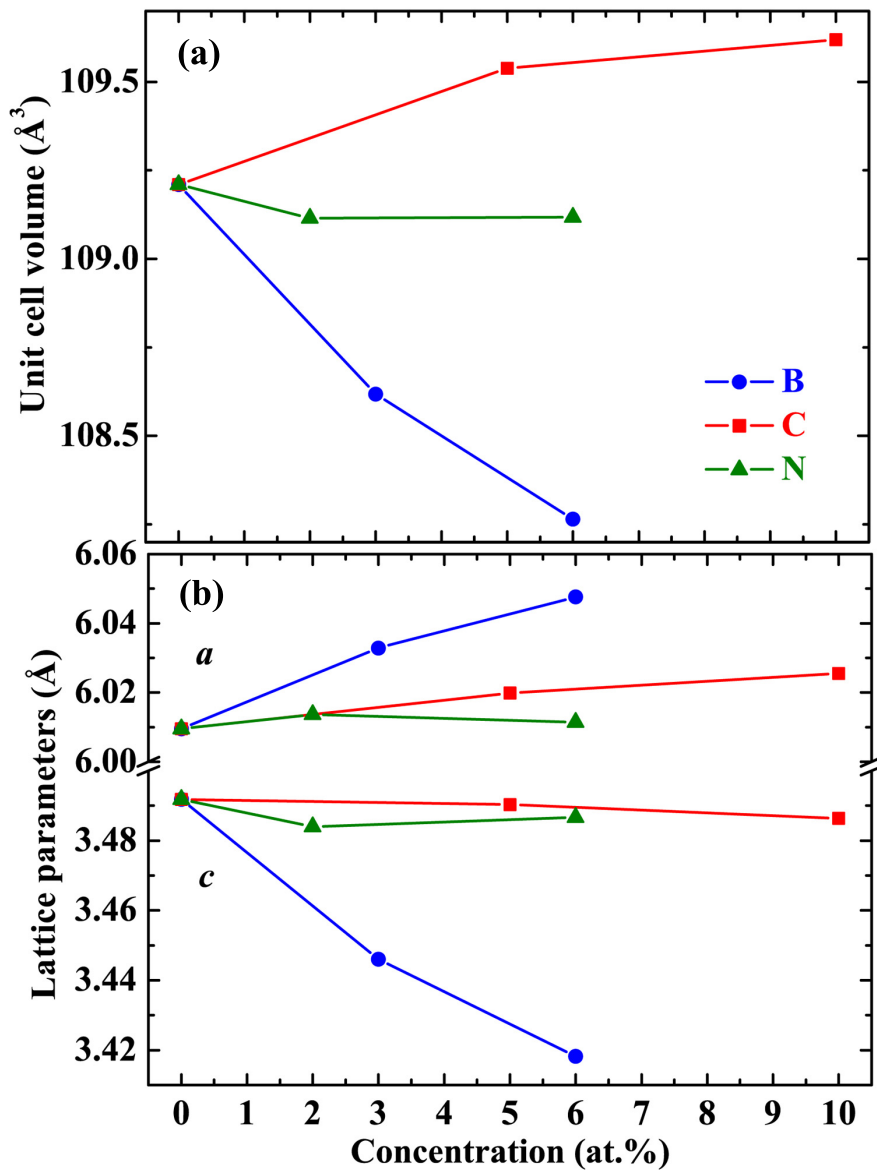
Table 4.2: Structural parameters of Mn$_{1.0}$Fe$_{0.95}$P$_{0.7}$Si$_{0.33}$ parent and B, C, N-doped samples derived from neutron diffraction. Atomic positions: 2c (1/3, 2/3, 0), 1b (0, 0, 1/2), 6j (x_1, y_1, 0) and 6k (x_2, y_2, 1/2). The 3f site: atomic positions (0.2540$_2$, 0, 0) with n(Fe)/n(Mn) = 0.230/0.020$_3$. The 3g site: atomic position (0.5900$_5$, 0, 1/2) with n(Fe)/n(Mn) = 0.020/0.230$_3$

Site	Parameter	Parent	3 at.%B	6 at.%B	5 at.%C	10 at.%C	2 at.%N	6 at.%N
	a (Å)	6.0096_1	6.0329_1	6.0476_1	6.0198_1	6.0255_1	6.0137_1	6.0114_1
	c (Å)	3.4918_1	3.4461_1	3.4182_1	3.4903_1	3.4863_1	3.4840_1	3.4867_1
	v (Å^3)	109.210_3	108.618_4	108.265_4	109.538_3	109.619_3	109.115_4	109.118_5
2c	n(P)	0.113_3	0.108_4	0.110_4	0.113_4	0.113_4	0.113*	0.113*
	n(Si)	0.054_3	0.059_4	0.057_4	0.054_4	0.054_4	0.054*	0.054*
1b	n(P)	0.054_3	0.059_4	0.058_4	0.054_4	0.054_4	0.054*	0.054*
	n(Si)	0.029_3	0.017_4	0.010_4	0.029_4	0.029_4	0.028_1	0.026_1
	n(B/N)	-	0.007_4	0.015_4	-	-	0.001_1	0.003_1
6j	x_1	-	-	-	0.43_1	0.46_1	0.45**	0.45_2
y_1	x_1	-	-	-	0.29_1	0.32_1	0.28**	0.28_2
	n(C/N)	-	-	-	0.007_1	0.013_1	0.002_1	0.006_1
6k	x_2	-	-	-	0.10_2	0.12_1	0.09**	0.09_2
	y_2	-	-	-	0.25_2	0.21_1	0.37**	0.37_1
	n(C/N)	-	-	-	0.006_1	0.012_1	0.002_1	0.006_1
	R_p (%)	4.26	4.73	5.71	7.60	6.08	4.64	5.74
	wR_p (%)	5.05	5.82	7.17	9.27	7.01	5.55	7.62
	χ^2	1.84	3.16	4.98	3.88	3.10	2.68	4.92

* Preliminary Rietveld refinement shows that only the Si on the 1b site is substituted by N, and the Si/P occupancy on the 2c site is not influenced by N dopants. As a result, the Si/P occupancy on the 2c site and the P occupancy on the 1b site are fixed in the final refinement.

** The coordinates of the 6j and 6k sites in the 2 at.% N-doped sample are assumed to be identical to those in 6 at.% N-doped samples.

4.5. INTERATOMIC DISTANCES

THE electronic reconfiguration around the Fe atoms on the $3f$ site is at the core of the FOMT in the (Mn,Fe)$_2$(P,Si)-type compounds. A detailed study of atomic distances between Fe and its neighboring atoms can provide insights into the relationship between the tunability of the FOMT and the structural changes induced by B, C and N doping.

As shown in Fig. 4.4(a) and (b), the introduction of B increases the atomic distance between Fe and its nearest Fe and Si atoms on the same layer, which hinders the overlap of Fe-Fe $3d$ electrons and the formation of the Fe-Si chemical bonds. In addition, the shortening of the Fe($3f$)-Mn($3g$) distance (see Fig. 4.4(c)) enhances the magnetic interaction between Fe and Mn atoms. These structural changes as a result of the B doping promote the formation and development of the Fe moment on the $3f$ site, leading to an increase in the FM transition temperature. The enhancement of the Fe moment weakens the unique mixed magnetism in (Mn,Fe)$_2$(P,Si). A similar effect is also observed when the Si/P ratio increases [5].

The occupation of C atoms on the interstitial $6j$ and $6k$ sites increases the Fe-Fe and Fe-Si distance within the basal plane (see Fig. 4.4(a) and (b)), while it has little influence on the interlayer Fe-Mn distance (see Fig. 4.4(c)). This will reduce the chemical bonding between Fe and its neighbors and stabilize the Fe moment. According to DFT calculations [5, 17] and Mössbauer experiments [18], charge transfer predominantly occurs between the Fe atoms on the $3f$ site and their neighboring non-metal atoms on the same basal plane. Charge transfer may occur from the Fe on the $3f$ site to the coplanar C atom on the $6j$ site in order to fill the p band of C, which increases the splitting of the Fe d band and thus enhances the Fe moment. On the other hand, the possible p-d hybridization between Fe($3f$) and C($6j$) will suppress the Fe moment. The competition between these two opposite effects finally gives rise to the increase in T_C upon C doping. Compared to B and C, a smaller influence on the Fe-Fe, Fe-Si and Fe-Mn distance (see Fig. 4.4(a)-(c)) is observed for N doping. However, the short Fe($3f$)-N($6j$) distance observed in Fig. 4.4(d) (much shorter than the Fe($3f$)-C($6j$) distance) strongly enhances the p-d hybridization between Fe and N($6j$). As a result, the T_C of the FOMT is reduced upon N doping.
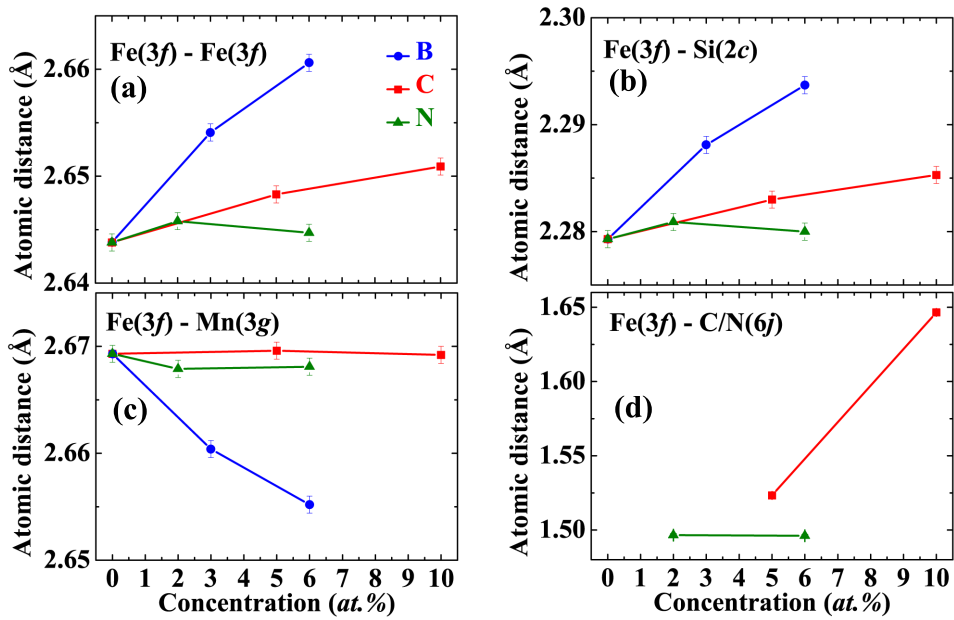
Figure 4.4: Interatomic distances as a function of the B, C and N concentration for $MnFe_{0.95}P_{0.67}Si_{0.33}$. Solid lines are a guide to the eye.

4.6. Conclusions

THE magnetoelastic transition of $(Mn,Fe)_2(P,Si)$ can be tuned by doping with B, C and N atoms. The site occupation of these light dopants in the crystal structure is resolved by neutron diffraction. B substitutes Si on the $1b$ site, while C occupies the interstitial $6j$ and $6k$ sites in the hexagonal structure. N atoms distribute on both on the 1b and the interstitial $6j$ and $6k$ sites. The tuning effect on the FOMT is caused by subtle variations in the electronic configuration, which in turn tailor the mixed magnetism responsible for the excellent magnetocaloric properties in these compounds.

References

[1] O. Tegus, E. Brück, K. H. J. Buschow, and F. R. de Boer, *Transition-metal-based magnetic regrigerants for room-temperature applications,* Nature **415**, 150 (2002).

[2] N. H. Dung, Z. Q. Ou, L. Caron, L. Zhang, D. T. Cam Thanh, G. A. de Wijs, R. A. de Groot, K. H. J. Buschow, and E. Brück, *Mixed magnetism for refrigeration and energy conversion,* Adv. Energy Mater. **1**, 1215 (2011).

[3] E. Brück, N. T. Trung, Z. Q. Ou, and K. H. J. Buschow, *Enhanced magnetocaloric effects and tunable thermal hysteresis in transition metal pnictides,* Scripta Mater. **67**, 590 (2012).

[4] F. Guillou, G. Porcari, H. Yibole, N. H. van Dijk, and E. Brück, *Taming the first-order transition in giant magnetocaloric materials,* Adv. Mater. **26**, 2671 (2014).

[5] X. F. Miao, L. Caron, P. Roy, N. H. Dung, L. Zhang, W. A. Kockelmann, R. A. de Groot, N. H. van Dijk, and E. Brück, *Tuning the phase transition in transition-metal-based magnetocaloric compounds,* Phys. Rev. B **89**, 174429 (2014).

[6] X. F. Miao, L. Caron, Z. Gercsi, A. Daoud-Aladine, N. H. van Dijk, and E. Brück, *Thermal-history dependent magnetoelastic transition in $(Mn,Fe)_2(P,Si)$,* Appl. Phys. Lett. **107**, 042403 (2015).

[7] N. H. Dung, L. Zhang, Z. Q. Ou, L. Zhao, L. van Eijck, A. M. Mulders, M. Avdeev, E. Suard, N. H. van Dijk, and E. Brück, *High/low-moment phase transition in hexagonal Mn-Fe-P-Si compounds,* Phys. Rev. B **86**, 045134 (2012).

[8] X. B. Liu, J. Ping Liu, Q. Zhang, and Z. Altounian, *Fe magnetic moment formation and exchange interaction in Fe_2P: a first-principles study,* Phys. Lett. A **377**, 731 (2013).

[9] E. K. Delczeg-Czirjak, L. Delczeg, M. P. J. Punkkinen, B. Johansson, O. Eriksson, and L. Vitos, *Ab initio study of structural and magnetic properties of Si-doped Fe_2P,* Phys. Rev. B **82**, 085103 (2010).

[10] X. B. Liu and Z. Altounian, *A first-principles study on the magnetocaloric compound $MnFeP_{2/3}Si_{1/3}$,* J. Appl. Phys. **105**, 07A902 (2009).

[11] N. H. Dung, L. Zhang, Z. Q. Ou, and E. Brück, *From first-order magneto-elastic to magneto-structural transition in $(Mn,Fe)_{1.95}P_{0.50}Si_{0.50}$ compounds,* Appl. Phys. Lett. **99**, 092511 (2011).

[12] N. H. Dung, L. Zhang, Z. Q. Ou, and E. Brück, *Magnetoelastic coupling and magnetocaloric effect in hexagonal Mn-Fe-P-Si compounds,* Scripta Mater. **67**, 975 (2012).

[13] W. G. Williams, R. M. Ibberson, P. Day, and J. E. Enderby, *GEM - General materials diffractometer at ISIS,* Physica B **241–243**, 234 (1997).

[14] J. Rodríguez-Carvajal, *Recent advances in magnetic structure determination by neutron powder diffraction,* Physica B **192**, 55 (1993).

[15] S. Rundqvist, Ark. Kemi **20**, 67 (1962).

[16] R. Chandra, S. Bjarman, T. Ericsson, L. Häggström, C. Wilkinson, and R. Wäppling, *A mössbauer and X-ray study of $Fe_2P_{1-x}B_x$ compounds (x<0.15),* J. Solid State Chem. **34**, 389 (1980).

[17] Z. Gercsi, E. K. Delczeg-Czirjak, L. Vitos, A. S. Wills, A. Daoud-Aladine, and K. G. Sandeman, *Magnetoelastic effects in doped Fe_2P,* Phys. Rev. B **88**, 024417 (2013).

[18] P. Jernberg, A. A. Yousif, L. Häggström, and Y. Andersson, *A Mössbauer study of $Fe_2P_{1-x}Si_x$ (x<0.35),* J. Solid State Chem. **53**, 313 (1984).

4

5

THERMAL-HISTORY DEPENDENT MAGNETOELASTIC TRANSITION IN (MN,FE)₂(P,SI) COMPOUNDS

The thermal-history dependence of the magnetoelastic transition in (Mn,Fe)₂(P,Si) compounds has been investigated using high-resolution neutron diffraction. As-prepared samples display a large difference in paramagnetic-ferromagnetic (PM-FM) transition temperature compared to cycled samples. The initial metastable state transforms into a lower-energy stable state when the as-prepared sample crosses the PM-FM transition for the first time. This additional transformation is irreversible around the transition temperature and increases the energy barrier which needs to be overcome through the PM-FM transition. Consequently the transition temperature on first cooling is found to be lower than on subsequent cycles characterizing the so-called "virgin effect". High-temperature annealing can restore the cycled sample to the high-temperature metastable state, which leads to the recovery of the virgin effect. A model is proposed to interpret the formation and recovery of the virgin effect.
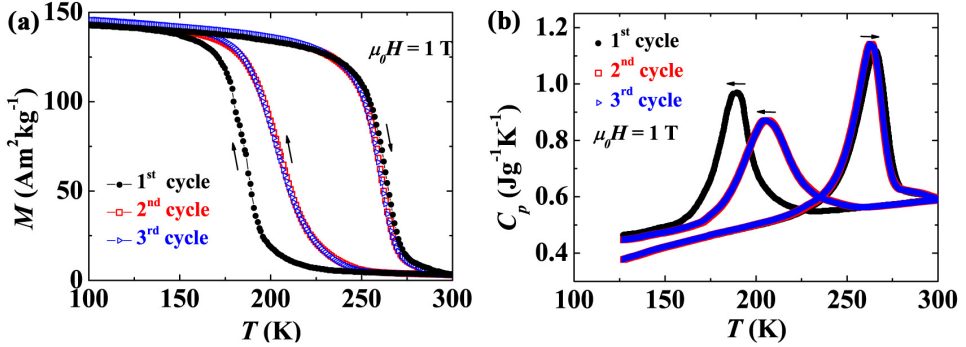
Figure 5.1: Temperature-dependent (a) magnetization and (b) specific heat during the first, second and third thermal cycle of as-prepared $Mn_{1.0}Fe_{0.95}P_{0.60}Si_{0.40}$ sample.

5.1. INTRODUCTION

HEXAGONAL Fe_2P-type compounds, showing a strong spin-lattice coupling and a giant magnetocaloric effect, are of great interest for scientists working on both fundamental research and technological applications. [1–8] $(Mn,Fe)_2(P,Si)$ compounds display a first-order paramagnetic-ferromagnetic (PM-FM) transition coupled with the discontinuous changes in the lattice parameters. [4, 5, 9] The character of the phase transition and the critical temperature can be easily tuned by balancing the Mn/Fe and P/Si ratios.[10] Interestingly, the magnetoelastic transition in the $(Mn,Fe)_2(P,Si)$ compounds shows a peculiar thermal-history dependence. As illustrated in Fig. 5.1, the as-prepared sample has a significantly lower phase transition temperature (T_C) upon first cooling than on second and subsequent cooling cycles. Since this behavior is only observed in as prepared or virgin samples it is termed the "virgin effect". Similar behavior has also been reported in MnAs-based [11], MnCoGe-based [12], $(Mn,Fe)_2(P,Ge)$ [13, 14] and $(Mn,Fe)_2(P,Si,Ge)$ [15] compounds.

The difference in T_C between the first and second cooling processes of the as-prepared sample, hereafter referred to as ΔT_{Ci}, is taken as a measure of how strong the virgin effect is. ΔT_{Ci} values of about 6 K and 13 K were observed in as-prepared MnAs-based and MnCoGe-based compounds, respectively. The virgin effect in these two compounds was proposed to be due to the big volume change (about 2% and 4%) accompanying the magnetostructural transition.[11, 12] However, $(Mn,Fe)_2(P,Si)$ has a stronger virgin effect with a ΔT_{Ci} of about 15 K, while the volume change at the magnetoelastic transition is less than 0.2%. Zhang *et al.*[16] suggested that the virgin effect in $(Mn,Fe)_2(P,Si)$ is due to the swapping of atomic positions during the first cooling of an as-prepared sample,

although no experimental evidence was found. Based on temperature-dependent Mössbauer experiments, Liu *et al.*[13] proposed that the virgin effect observed in $(Mn,Fe)_2(P,Ge)$ may originate from an additional irreversible structural change during the first cooling process of an as-prepared sample. Höglin *et al.*[17] also attributed the virgin effect in $(Mn,Fe)_2(P,Si)$ to irreversible structural changes.

In this chapter, the temperature-dependent high-resolution neutron diffraction was performed to monitor the changes in structural parameters, especially the interplanar spacing, during the first and second thermal cycle of an as-prepared $(Mn,Fe)_2(P,Si)$ sample. A recovery of the virgin effect induced by thermal activation was observed experimentally. The virgin effect in $(Mn,Fe)_2(P,Si)$ can be attributed to the presence of an irreversible structural transformation.

5.2. EXPERIMENTAL

THE $Mn_{1.0}Fe_{0.95}P_{0.60}Si_{0.40}$ compound was prepared as described in *Chapter 2*. The magnetic properties were characterized using a superconducting quantum interference device (SQUID) magnetometer (Quantum Design MPMS 5XL) in the reciprocating sample option (RSO) mode. The specific heat was measured using a commercial differential scanning calorimeter (TA Instrument Q2000) operated at the standard mode. *In-situ* neutron diffraction experiments were carried out on the time-of-flight high-resolution powder diffractometer (HRPD) at the ISIS pulsed neutron source facility, UK. This instrument has a $\Delta d/d$ resolution of $\sim 4 \times 10^{-4}$, which allows us to accurately study the changes in the interplanar spacings inside the sample through the phase transition. Neutron diffraction data were collected from three banks after thermal equilibrium at the following temperatures: 300, 185 ($\sim T_C$) and 120 K for the 1st cooling; 300, 200 ($\sim T_C$) and 120 K for the 2nd cooling. Nuclear and magnetic structure refinement of the neutron diffraction patterns was performed using the Rietveld method implemented in Fullprof [18].

5.3. STRUCTURAL CHANGES DURING THERMAL CYCLING

FIGURE 5.2(a) displays a neutron diffraction pattern of the as-prepared $Mn_{1.0}Fe_{0.95}P_{0.60}Si_{0.40}$ compound measured at 300 K, as an example. Good agreement between the experimental and calculated patterns was achieved assuming a hexagonal Fe_2P-type structure (space group $P\bar{6}2m$). Structural parameters calculated from the Rietveld refinement are summarized in Fig. 5.2(b)-(d) and Table 5.1. As shown in Fig. 5.2(b) and Table 5.1, at 300 K the as-prepared sample has lattice parameters, atomic positions and occupancies very close to those after the first thermal cycle. The evolution of the lattice parameters also shows a similar behavior during the first two cycles, although a significantly lower T_C is
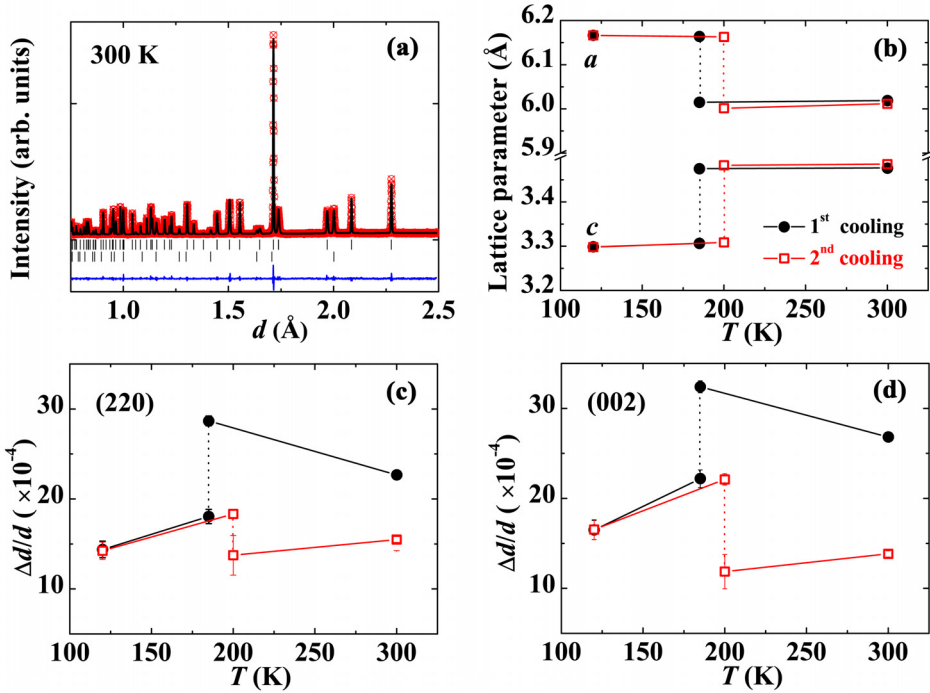
Figure 5.2: (a) Observed and calculated neutron diffraction patterns at the HRPD (detector bank 1 with $<2\theta> \approx 168.33°$) for as-prepared $Mn_{1.0}Fe_{0.95}P_{0.60}Si_{0.40}$. Vertical lines indicate the peak positions for the main phase (top) and the impurity phase $(Mn,Fe)_3Si$ (bottom). Evolution of lattice parameters (b) and deviation of interplanar spacing of (220) atomic planes (c) and (002) atomic planes (d) during the first and second cooling of the as-prepared sample. The dotted line indicates the position of T_C.

observed for the first cooling.

It should be noted that the lattice parameters, atomic positions and occupancies obtained from the Rietveld refinement correspond to averages.[19–21] Local variations only contribute to the peak width. The local variations can be characterized by the variations in interplanar spacing, i.e., $\Delta d/d$. This quantity can be obtained using an anisotropic peak broadening model [22] to describe the peak shape of our high-resolution neutron diffraction patterns. The temperature-dependent $\Delta d/d$ of (220) and (002) planes corresponds to variations within the basal ab plane and along the c axis, respectively (Fig. 5.2(c) and (d)). At 300 K the as-prepared sample has much higher $\Delta d/d$ values for the (220) and (002) planes than after undergoing thermal cycling. The difference is more pronounced along the c axis. A drop in $\Delta d/d$ was observed around T_C (see Fig. 5.2(c) and (d)) during the first cooling. On the contrary, a reversible jump in

Table 5.1: Structural parameters of $Mn_{1.0}Fe_{0.95}P_{0.60}Si_{0.40}$ at 300 K. Space group: $P\bar{6}2m$. Atomic positions: $3f$ $(x_1,0,0)$; $3g$ $(x_2,0,1/2)$; $2c$ $(1/3,2/3,0)$ and $1b$ $(0,0,1/2)$.

	Parameters	As-prepared state	After first cycle
$3f$	x_1	0.2538(2)	0.2538(2)
	$n(Fe)/n(Mn)$	0.225/0.025(1)	0.225/0.025(1)
$3g$	x_2	0.5902(4)	0.5895(4)
	$n(Mn)/n(Fe)$	0.238/0.012(1)	0.238/0.012(1)
$2c$	$n(P)/n(Si)$	0.094/0.073(4)	0.094/0.073(4)
$1b$	$n(P)/n(Si)$	0.056/0.027(4)	0.056/0.027(4)
	$Rp(\%)$	3.43	3.63
	$wRp(\%)$	4.18	4.33
	χ^2	3.69	3.87

$\Delta d/d$ around T_C appears during the second and subsequent cooling processes. This indicates that atoms in the as-prepared sample show a larger spread around their equilibrium crystallographic site, while the spatial variations become significantly smaller when the sample crosses the PM-FM transition for the first time. This additional atomic reconfiguration may increase the energy barrier to be overcome during the first PM-FM phase transition, which leads to a lower T_C. The subtle atomic reconfiguration is irreversible. As a result, a different T_C on cooling can only be observed when the as-prepared sample crosses the phase transition for the first time, being stabilized afterwards. The reversible jump in the $\Delta d/d$ around the T_C during the subsequent thermal cycles is due to the lattice distortion caused by the first-order magnetoelastic transition. Consequently, the same T_C is observed during the second and subsequent cooling processes.

5.4. RECOVERY OF THE VIRGIN EFFECT

THE difference in atomic configuration between the as-prepared and cycled samples can be understood by considering the thermal history of the sample. As-prepared samples undergo a high-temperature sintering and annealing process where the high-temperature phase may be frozen and preserved at lower temperatures. However, the frozen high-temperature phase with a higher structural disorder is not stable at low temperatures and transforms to a more ordered stable phase when the sample crosses the PM-FM phase transition for the first time. This structural transition is irreversible at low temperatures since the activation energy cannot be reached, while high temperature annealing should provide enough energy to restore the initial high-temperature phase. As a consequence, the virgin effect may be recovered. To test this hypothesis, the as-prepared sample was first thermally cycled a few times using liquid nitrogen to

eliminate the virgin effect. Subsequently, the cycled samples were re-annealed at different temperatures for 2 hours before being quenched into water.

The temperature-dependent magnetization of the re-annealed samples is shown in Fig. 5.3, from which the ΔT_C as a function of re-annealing temperature (T_a) can be obtained (see Fig. 5.4(a)). No detectable shift in T_C between the first and second cooling can be observed when T_a is lower than 573 K. At 673 K, a ΔT_C of about 2 K appears, indicating the start of the structural recovery process. ΔT_C increases slowly until $T_a \approx 1123$ K. Above this temperature the recovery process accelerates with increasing re-annealing temperature. ΔT_C is fully recovered at T_a from 1298 K up to the original sintering temperature of 1373 K. Another feature that can be seen from Fig. 5.3 is that the PM-FM transition of the 1298 K re-annealed sample is much sharper than the as-prepared and the low-T_a re-annealed ones. This is due to better compositional homogeneity obtained after the high-temperature re-annealing process.
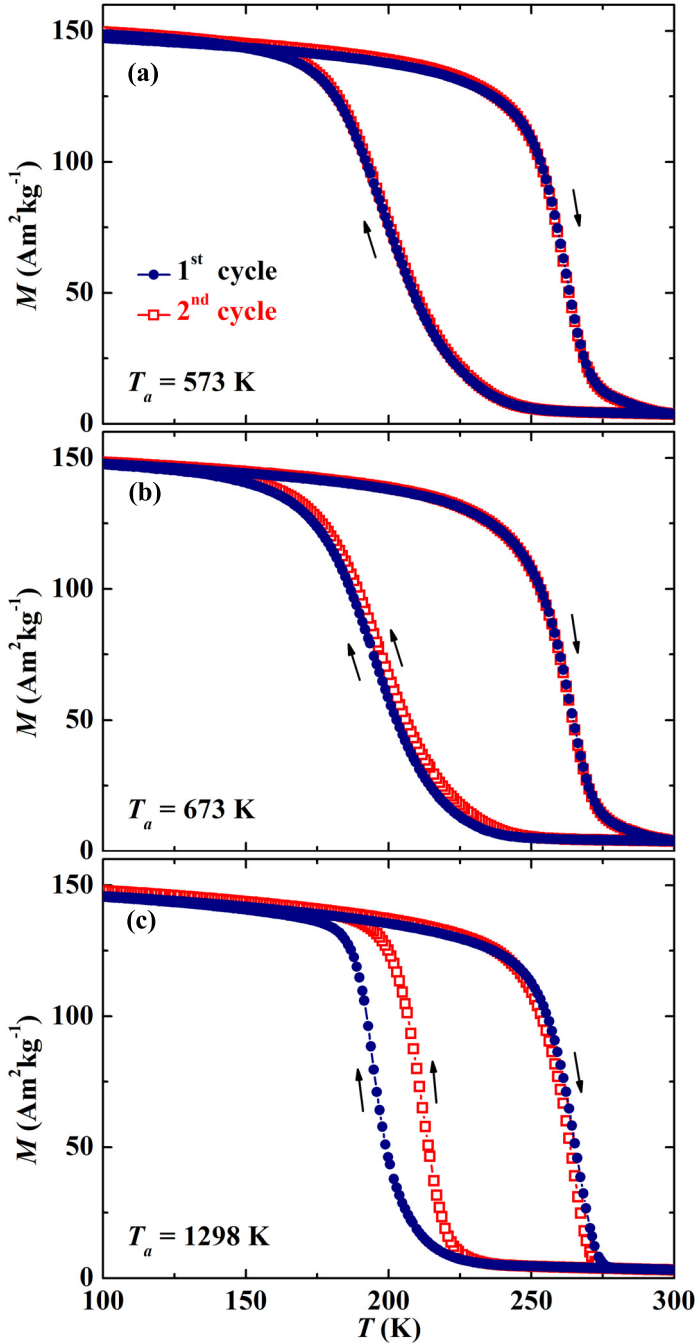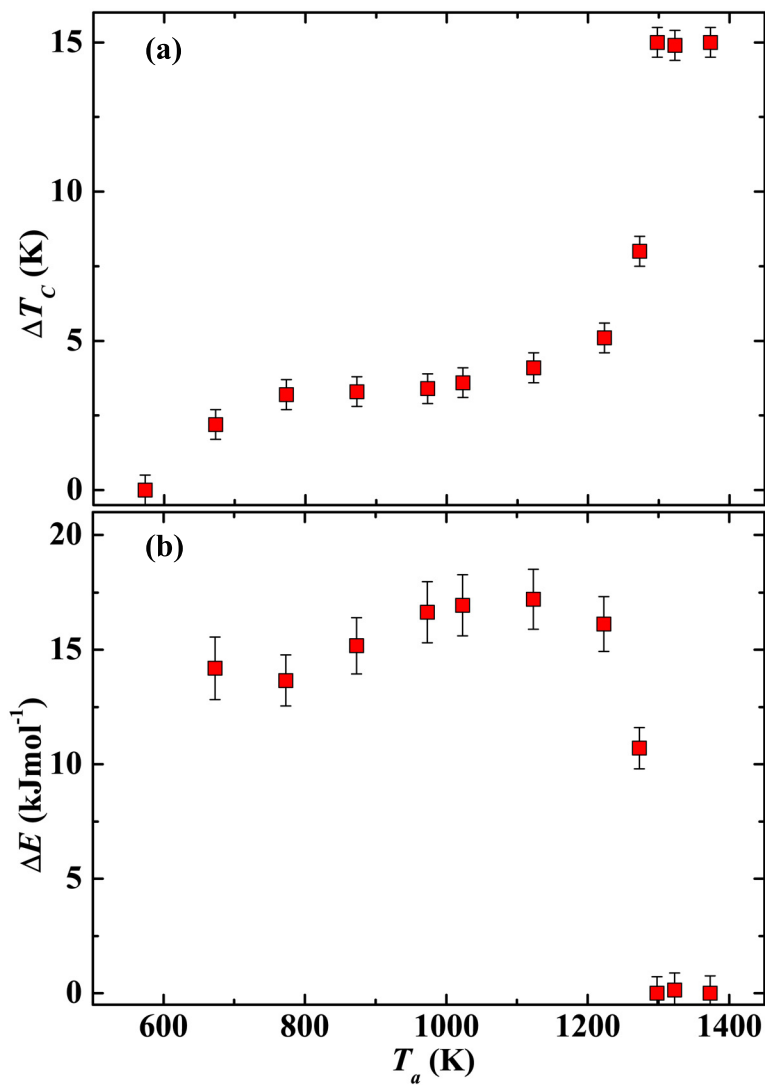
5

Figure 5.3: Isofield magnetization measured at a field of 1 T during the first and second thermal cycle of the $Mn_{1.0}Fe_{0.95}P_{0.60}Si_{0.40}$ samples re-annealed at different temperatures.

Figure 5.4: (a) ΔT_C and (b) energy difference as a function of re-annealing temperature.

5.5. Thermodynamic model

As discussed above, the as-prepared sample has a higher structural disorder that results in an additional irreversible structural transition during the first cooling process. High temperature annealing can restore the metastable phase, and consequently recover the virgin effect. Based on these results, we propose a model to describe the virgin effect in $(Mn,Fe)_2(P,Si)$ compounds.

The high thermal activation energies accessible at elevated temperatures allow atoms to occupy positions which deviate from the crystallographic site described in Table 5.1. There may be two or multiple equivalent energy states in the system at high temperature, which correspond to different atomic coordinates in the structure. Currently, with the experimental error at hand we cannot determine how many sites are involved. In the present model, it is assumed that there are two energetically degenerated states in the system, as illustrated in Fig. 5.5(a). The high-temperature atomic configuration may be preserved in the as-prepared sample after high-temperature sintering and annealing. However, the energy profile has changed at low temperature. The states 1 and 2 are not energetically equivalent probably due to a Jahn-Teller type distortion[23, 24]. An energy difference ΔE appears between state 1 and state 2, see Fig. 5.5(b)). The ΔE is related to the populations N_1 and N_2 of states 1 and 2, respectively, by the Boltzmann factor $N_2/N_1 = e^{-\Delta E/RT}$. R is the gas constant. The strength of virgin effect depends on the relative populations of the two states, which can be described as

$$\Delta T_C = \frac{2N_2\Delta T_{Ci}}{N_1 + N_2} = \frac{2\Delta T_{Ci}}{1 + e^{\Delta E/RT}} \tag{5.1}$$

where ΔT_C and ΔT_{Ci} are the difference in T_C between the first and second cooling for the re-annealed and as-prepared samples, respectively. Using Eq. (5.1) and the data in Fig. 5.4(a), the effective energy difference at different temperatures is calculated and shown in Fig. 5.4(b). The ΔE is almost constant around 15 kJ/mol when the reannealing temperature is below 1123 K. Beyond 1123 K, a sudden drop in the ΔE appears. State 1 and 2 become energetically equivalent when the reannealing temperature is above 1298 K.

As illustrated by Fig. 5.5(b) and (c), during the first cooling of the as-prepared sample, the frozen high-temperature metastable phase transforms to a stable phase through the atomic reconfiguration caused by the magnetoelastic phase transition. After the first thermal cycle only state 1 is occupied (see Fig. 5.5(c)), i.e., $N_1 = 1$ and $N_2 = 0$, which results in a more ordered state as observed by neutron diffraction. The structural transition is irreversible at low temperatures because of the low thermal energy and the high energy barrier. Therefore around room temperature the ΔT_C is always 0 after the first thermal cycle. When the cy-

5
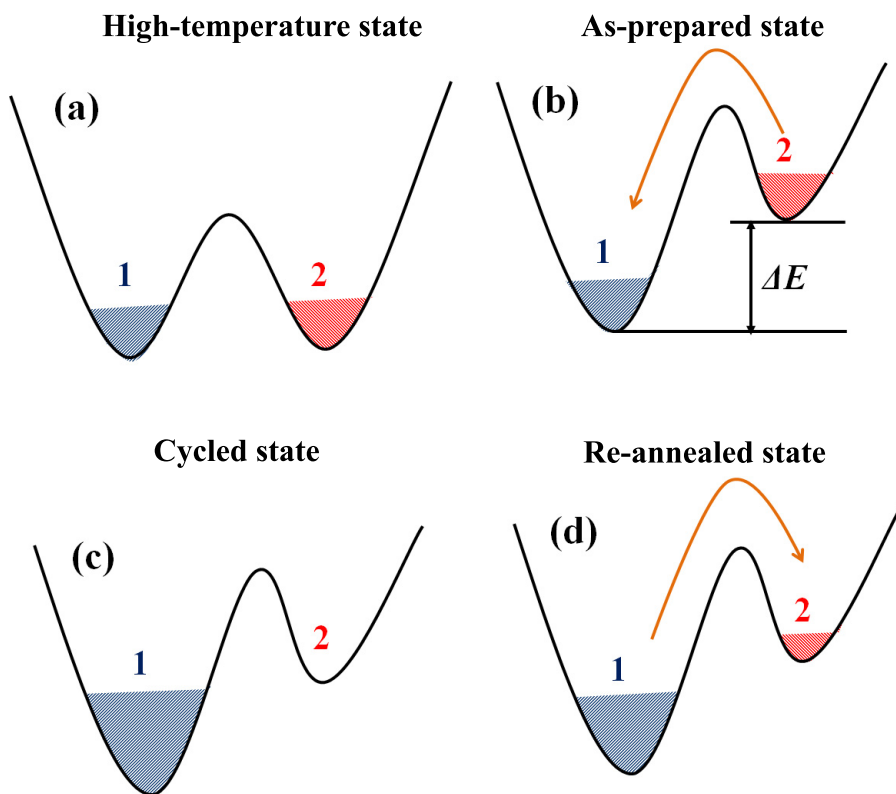
Figure 5.5: Schematic diagram of free-energy profiles for $(Mn,Fe)_2(P,Si)$ during thermal cycling.

cled sample is re-annealed at intermediate temperatures (between 673 and 1123 K as indicated in Fig. 5.4), thermal energy is enough to start overcoming the energy barrier between states 1 and 2. As a result, N_2 increases gradually and so does ΔT_C. At elevated temperatures (above 1123 K), the high-temperature structure without Jahn-Teller type distortion recovers rapidly, leading to a sudden drop in the energy difference and a significant rise in the ΔT_C. As T_a goes above 1298 K, the initial high-temperature structure with equivalent energy states (Fig. 5.5a) is restored and the virgin effect is fully recovered. It should be noted that the ΔT_C shows a time-dependent behavior at high temperatures, but this would not change the overall physical picture illustrated in Fig. 5.5.

The virgin effect of MnCoGe-based and MnAs-based compounds may also originate from a metastable state in the as-prepared sample. As-prepared MnCoGe-based compounds have a hexagonal structure, which is formed at room temperature by quenching the sample from high temperature.[25, 26] The frozen high-temperature phase may have higher disorder giving rise to the virgin effect in a similar way as in Fe_2P-based compounds. MnAs-based compounds crystallize in a re-entrant orthorhombic structure, while showing the same hexagonal structure at both high and low temperatures.[27, 28] The structural transition between the high-temperature hexagonal and the re-entrant orthorhombic phase may cause structural distortions in the as-prepared orthorhombic structure, which increases the energy barrier of the magnetostructural transition between re-entrant orthorhombic and low-temperature hexagonal phases. During the subsequent thermal cycles, the distorted orthorhombic phase does not appear again since the sample does not enter the high-temperature hexagonal region. As a result, a lower T_C is observed only when the as-prepared MnAs-based compound undergoes the orthorhombic to low-temperature hexagonal transition for the first time.

5

5.6. CONCLUSIONS

IN conclusion, the unusual thermal-history dependent phase transition behavior in as-prepared $(Mn,Fe)_2(P,Si)$ compounds, called the "virgin effect" was studied. The virgin effect is found to be related to a metastable state preserved in the as-prepared sample after high-temperature annealing. The as-prepared sample shows larger variations in the atomic positions, as suggested by a structure analysis. The metastable phase transforms irreversibly to the stable low-temperature phase during the paramagnetic-ferromagnetic transition upon first cooling and is afterwards stabilized. Due to this additional transformation the energy barrier which needs to be overcome at the first cooling transition is higher and a lower T_C is observed in relation to subsequent cooling processes. High temperature annealing can restore the high-temperature metastable state, which

leads to the recovery of the "virgin effect". Due to the change in T_C at the first-cooling transition, the as-prepared $(Mn,Fe)_2(P,Si)$ compounds should be precooled to remove the virgin effect before being used in magnetic refrigerators and power generators.

REFERENCES

[1] L. Lundgren, G. Tarmohamed, O. Beckman, B. Carlsson, and S. Rundqvist, *First order magnetic phase transition in Fe$_2$P*, Phys. Scr. **17**, 39 (1978).

[2] O. Tegus, E. Brück, K. H. J. Buschow, and F. R. de Boer, *Transition-metal-based magnetic regrigerants for room-temperature applications*, Nature **415**, 150 (2002).

[3] N. T. Trung, Z. Q. Ou, T. J. Gortenmulder, O. Tegus, K. H. J. Buschow, and E. Brück, *Tunable thermal hysteresis in MnFe(P,Ge) compounds*, Appl. Phys. Lett. **94**, 102513 (2009).

[4] N. H. Dung, L. Zhang, Z. Q. Ou, and E. Brück, *From first-order magneto-elastic to magneto-structural transition in (Mn,Fe)$_{1.95}$P$_{0.50}$Si$_{0.50}$ compounds*, Appl. Phys. Lett. **99**, 092511 (2011).

[5] N. H. Dung, Z. Q. Ou, L. Caron, L. Zhang, D. T. Cam Thanh, G. A. de Wijs, R. A. de Groot, K. H. J. Buschow, and E. Brück, *Mixed magnetism for refrigeration and energy conversion*, Adv. Energy Mater. **1**, 1215 (2011).

[6] E. K. Delczeg-Czirjak, Z. Gercsi, L. Bergqvist, O. Eriksson, L. Szunyogh, P. Nordblad, B. Johansson, and L. Vitos, *Magnetic exchange interactions in B-, Si-, and As-doped Fe$_2$P from first-principles theory*, Phys. Rev. B **85**, 224435 (2012).

[7] Z. Gercsi, E. K. Delczeg-Czirjak, L. Vitos, A. S. Wills, A. Daoud-Aladine, and K. G. Sandeman, *Magnetoelastic effects in doped Fe$_2$P*, Phys. Rev. B **88**, 024417 (2013).

[8] M. Hudl, L. Häggström, E. K. Delczeg-Czirjak, V. Höglin, M. Sahlberg, L. Vitos, O. Eriksson, P. Nordblad, and Y. Andersson, *Strongly enhanced magnetic moments in ferromagnetic FeMnP$_{0.5}$Si$_{0.5}$*, Appl. Phys. Lett. **99**, 152502 (2011).

[9] N. H. Dung, L. Zhang, Z. Q. Ou, L. Zhao, L. van Eijck, A. M. Mulders, M. Avdeev, E. Suard, N. H. van Dijk, and E. Brück, *High/low-moment phase transition in hexagonal Mn-Fe-P-Si compounds*, Phys. Rev. B **86**, 045134 (2012).

5

[10] X. F. Miao, L. Caron, P. Roy, N. H. Dung, L. Zhang, W. A. Kockelmann, R. A. de Groot, N. H. van Dijk, and E. Brück, *Tuning the phase transition in transition-metal-based magnetocaloric compounds,* Phys. Rev. B **89**, 174429 (2014).

[11] W. B. Cui, X. K. Lv, F. Yang, Y. Yu, R. Skomski, X. G. Zhao, W. Liu, and Z. D. Zhang, *Interstitial-nitrogen effect on phase transition and magnetocaloric effect in Mn(As,Si) (invited),* J. Appl. Phys. **107**, 09A938 (2010).

[12] N. H. Trung, *First-order phase transitions and giant magnetocaloric effect,* Ph.D. thesis, Delft, 2010 .

[13] X. B. Liu, Z. Altounian, D. H. Ryan, M. Yue, Z. Q. Li, D. M. Liu, and J. X. Zhang, *Mössbauer spectroscopy study on the magnetic transition in $Mn_{1.1}Fe_{0.9}P_{0.8}Ge_{0.2}$,* J. Appl. Phys. **105**, 07A920 (2009).

[14] E. Brück, O. Tegus, D. T. Cam Thanh, N. T. Trung, and K. H. J. Buschow, *A review on Mn based materials for magnetic refrigeration: structure and properties,* Int. J. Refrig. **31**, 763 (2008).

[15] D. T. Cam Thanh, E. Brück, O. Tegus, J. C. P. Klaasse, T. J. Gortenmulder, and K. H. J. Buschow, *Magnetocaloric effect in MnFe(P,Si,Ge) compounds,* J. Appl. Phys. **99**, 08Q107 (2006).

[16] L. Zhang, O. Može, K. Prokeš, O. Tegus, and E. Brück, *Neutron diffraction study of history dependence in $MnFeP_{0.6}Si_{0.4}$,* J. Magn. Magn. Mater. **290-291**, 679 (2005).

[17] V. Höglin, J. Cedervall, M. S. Andersson, T. Sarkar, P. Nordblad, and M. Sahlberg, *Irreversible structure change of the as prepared $FeMnP_{1x}Si_x$-structure on the initial cooling through the curie temperature,* J. Magn. Magn. Mater. **374**, 455 (2015).

[18] J. Rodríguez-Carvajal, *Recent advances in magnetic structure determination by neutron powder diffraction,* Physica B **192**, 55 (1993).

[19] D. R. Veblen, P. J. Heaney, R. J. Angel, L. W. Finger, R. M. Hazen, C. T. Prewitt, N. L. Ross, C. W. Chu, P. H. Hor, and R. L. Meng, *Crystallography, chemistry and structural disorder in the new high-T_C Bi-Ca-Sr-Cu-O superconductor,* Nature **332**, 334 (1988).

[20] L. M. Rodriguez-Martinez and J. P. Attfield, *Cation disorder and size effects in magnetoresistive manganese oxide perovskites,* Phys. Rev. B **54**, R15622 (1996).

5

[21] B. C. Chakoumakos, B. C. Sales, D. G. Mandrus, and G. S. Nolas, *Structural disorder and thermal conductivity of the semiconducting clathrate $Sr_8Ga_{16}Ge_{30}$,* J. Alloys Compd. **296**, 80 (2000).

[22] P. W. Stephens, *Phenomenological model of anisotropic peak broadening in powder diffraction,* J. Appl. Cryst. **32**, 281 (1999).

[23] H. A. Jahn and E. Teller, *Stability of polyatomic molecules in degenerate electronic states I- orbital degeneracy,* Proc. Roy. Soc. A **161**, 220 (1937).

[24] K. I. Kugel and D. I. Khomskii, *The jahn-teller effect and magnetism: transition metal compounds,* Sov. Phys. Usp. **25**, 231 (1982).

[25] N. T. Trung, L. Zhang, L. Caron, K. H. J. Buschow, and E. Brück, *Giant magnetocaloric effects by tailoring the phase transitions,* Appl. Phys. Lett. **96**, 172504 (2010).

[26] P. E. Markin, N. V. Mushnikov, V. I. Khrabrov, and M. A. Korotin, *Magnetic properties of the $Mn_{1.9-x}Co_xGe$ compounds with a hexagonal crystal structure,* Phys. Met. Metallogr. **106**, 481 (2008).

[27] H. Okamoto, *The As-Mn (arsenic-manganese) system,* Bull. Alloy Phase Diagr. **10**, 549 (1989).

[28] T. Suzuki and H. Ido, *Relation between structural and magnetic properties of compounds $MnAs_{1-x}P_x$,* J. Phys. Soc. Jpn. **51**, 3149 (1982).

5

6

SHORT-RANGE MAGNETIC CORRELATIONS AND SPIN DYNAMICS IN THE PARAMAGNETIC REGIME OF $(MN,FE)_2(P,SI)$ COMPOUNDS

The spatial and temporal correlations of magnetic moments in the paramagnetic regime of (Mn,Fe)$_2$(P,Si) have been investigated by means of polarized neutron diffraction and muon-spin relaxation techniques. Short-range magnetic correlations are present at temperatures far above the ferromagnetic transition temperature (T_C). This leads to deviations of paramagnetic susceptibility from Curie-Weiss behavior. These short-range magnetic correlations extend in space and slow down with decreasing temperature, and finally develop into long-range magnetic order at T_C.
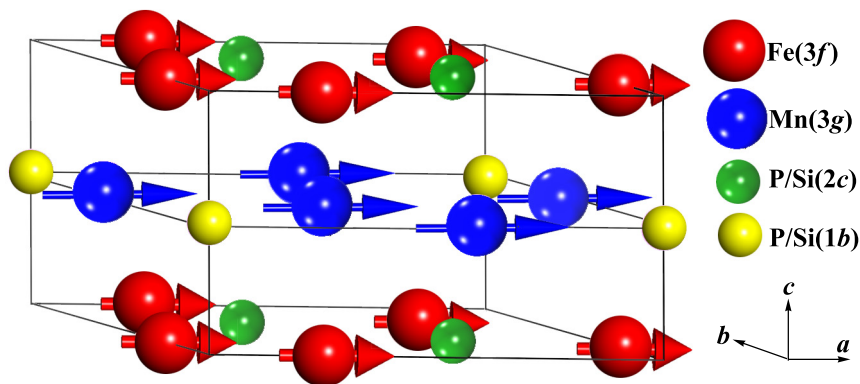
Figure 6.1: Schematic representation of the crystal and magnetic structure for $(Mn,Fe)_2(P,Si)$.

6.1. INTRODUCTION

THE ferromagnetic transition in $(Mn,Fe)_2(P,Si)$ compounds is tied to a structure change due to a strong magnetoelastic coupling without altering the symmetry [1]. A giant magnetocaloric effect is accompanied with the magnetoelastic transition, which makes this material system promising for refrigeration and power conversion applications [2, 3] By balancing the Mn:Fe and P:Si ratios [2], the GMCE can be achieved in a wide composition range, to cover an extensive range of working temperatures required for real applications.

The $(Mn,Fe)_2(P,Si)$ compound crystallizes in a hexagonal Fe_2P-type structure (space group $P\bar{6}2m$) [1], as illustrated in Fig. 6.1. Fe atoms preferentially occupy the tetrahedral $3f$ site, while Mn prefers the pyramidal $3g$ site [1, 4]. The nature of the ferromagnetic (FM) state, e.g. the magnitude and orientation of the magnetic moments, has been studied intensively using neutron diffraction techniques [1, 5–7]. As shown in Fig. 6.1, both the Mn and Fe moments lie within the basal ab plane in the FM phase.

A unique case of mixed magnetism has been revealed in the $(Mn,Fe)_2(P,Si)$ compound by density functional theory (DFT) calculations [2]. Above the ferromagnetic transition temperature T_C, the Mn atoms on the $3g$ sites do not show a significant reduction in magnetic moment. In contrast, the Fe moment changes from a partially quenched value into a large value at the ferromagnetic transition. The DFT calculations [2] indicate that the P and Si atoms play a crucial role in the formation of a sizable magnetic moment for the Fe atoms. In the paramagnetic (PM) state, a covalent bond is formed between the Fe and the neighboring P and Si atoms. As a result, the Fe moment is partially quenched. However, in the FM state, Fe carries a large magnetic moment instead of forming chemical

bonds, due to the redistribution of electron density between the Fe and the P and Si atoms.

Magnetic measurements in the PM regime of $(Mn,Fe)_2(P,Si)$ compounds [7] show that the PM susceptibility strongly deviates from the Curie-Weiss law, which has also been observed in other Fe_2P-type compounds [8–10]. This suggests the presence of a sizable short-range magnetic order in the PM state of the Fe_2P-type compounds. Polarized-neutron diffraction studies on the Fe_2P parent compound confirm the existence of short-range magnetic correlations above T_C [11, 12]. A magnetic correlation length of about 12.6 Å was derived for Fe_2P at $T = 3.7T_C$. Transverse-field muon-spin rotation and relaxation (μSR) experiments on the Fe_2P compound [13] reveal the absence of magnetic correlations with a lifetime longer than 10^{-10} s above a temperature of $1.05T_C$. Compared to Fe_2P, stronger magnetic correlations are expected in the PM state of $(Mn,Fe)_2(P,Si)$ due to the larger magnetic moment of Mn on the $3g$ site [2, 14].

However, how the unusual transition in Fe moment develops from short-range magnetic correlations is still unknown and not accessible by DFT calculations. Also, the influence of short-range magnetic correlations on the nature of the transition is not well understood. The work presented in this chapter aims to characterize the development of short-range magnetic correlations on both length- and time-scales in the PM regime of the $(Mn,Fe)_2(P,Si)$ compounds with both first and second order phase transitions, and further explore their roles in the magnetoelastic transition. Two compositions, which show first- and second-order phase transitions, respectively, were selected for the current study according to the previously derived compositional map [2].

xyz neutron polarization analysis [15–17] was performed in the PM regime of the $(Mn,Fe)_2(P,Si)$ compounds. The unambiguous separation of the magnetic scattering cross section from the nuclear and spin-incoherent contributions allows us to characterize the spatial correlations of magnetic spins in the PM state. Zero-field muon-spin relaxation experiments were used to study the dynamics of the spin correlations in the PM regime. Consequently, this study contributes to a better understanding of the magnetoelastic phase-transition on both length- and time-scales.

6

6.2. Experimental

Polycrystalline samples with nominal compositions $Mn_{1.00}Fe_{0.95}P_{0.67}Si_{0.33}$ and $Mn_{1.70}Fe_{0.25}P_{0.50}Si_{0.50}$ were prepared as described in *Chapter 2*. AC susceptibility measurements were performed on a superconducting quantum interference device (SQUID) magnetometer (Quantum Design MPMS 5XL). The amplitude and frequency of the AC magnetic field were 0.4 mT and 111 Hz, respectively. No DC field was applied during the AC susceptibility measurements. X-ray

diffraction patterns were collected on a Bruker D8 diffractometer using Cu $K_{\alpha 1}$ radiation. Structure refinement of the X-ray diffraction patterns was performed using Fullprof's [18] implementation of the Rietveld refinement method.

xyz neutron polarization experiments were performed on the D7 diffuse scattering diffractometer [16] at the Institut Laue-Langevin (ILL), with an incident neutron wavelength of 3.12 Å. The powder samples ($\approx$ 10 grams) were put into an aluminum hollow cylinder. Six spin-dependent scattering cross sections were measured for xyz polarization analysis between 150 K $\leqslant T \leqslant$ 500 K. The scattering cross sections were integrated for energy transfers ranging from about -10 to 8.5 meV. The instrument-dependent background was estimated from measurements of an empty sample can and a cadmium sample. Amorphous quartz was measured to establish the polarization efficiency for D7. Vanadium was measured to calibrate the detector efficiencies and to allow the scattering cross sections from the samples to be expressed in absolute units.

μSR experiments were carried out on the general purpose surface-muon instrument (GPS) at the Swiss muon source (SμS) of the Paul Scherrer Institute (PSI), Switzerland. Zero-field muon-spin relaxation signals were collected for powder samples ($\approx$ 1 gram) in the temperature range between 50 and 450 K using a closed cycle refrigerator.

6.3. MAGNETIC SUSCEPTIBILITY AND X-RAY DIFFRACTION

As shown in Fig. 6.2(a), the $\text{Mn}_{1.00}\text{Fe}_{0.95}\text{P}_{0.67}\text{Si}_{0.33}$ compound shows a large thermal hysteresis in the bulk susceptibility measurements, which is characteristic for a strong first-order phase transition. In contrast, the reversible PM-FM transition in Fig. 6.2(b) for the $\text{Mn}_{1.70}\text{Fe}_{0.25}\text{P}_{0.50}\text{Si}_{0.50}$ compound suggests a second-order nature of the phase transition, in agreement with the previous work [19]. The T_C values [20] on cooling for the $\text{Mn}_{1.00}\text{Fe}_{0.95}\text{P}_{0.67}\text{Si}_{0.33}$ and $\text{Mn}_{1.70}\text{Fe}_{0.25}\text{P}_{0.50}\text{Si}_{0.50}$ compounds are 130 and 175 K, respectively. Additionally, the $\text{Mn}_{1.00}\text{Fe}_{0.95}\text{P}_{0.67}\text{Si}_{0.33}$ compound shows an antiferromagnetic (AFM) transition at a Néel temperature of $T_N \approx$ 275 K (see the inset of Fig. 6.2(a)). The absence of thermal hysteresis implies that this PM-AFM transition is second order. It should be noted that the AFM intermediate phase has only been found in certain $(\text{Mn},\text{Fe})_2(\text{P},\text{Si})$ compositions (see *Chapter 7*). The formation of the AFM phase is due to the competing magnetic configurations and strong magnetoelastic coupling in $(\text{Mn},\text{Fe})_2(\text{P},\text{Si})$ compounds, as revealed by recent theoretical [21] and experimental (see *Chapter 7*) studies.

The inverse susceptibility in Fig. 6.2(c) and (d) measured above T_C for the $\text{Mn}_{1.00}\text{Fe}_{0.95}\text{P}_{0.67}\text{Si}_{0.33}$ and $\text{Mn}_{1.70}\text{Fe}_{0.25}\text{P}_{0.50}\text{Si}_{0.50}$ compounds, respectively, deviates from the Curie-Weiss law. This reflects the presence and development of short-range magnetic correlations in the PM state [7–10], which was confirmed
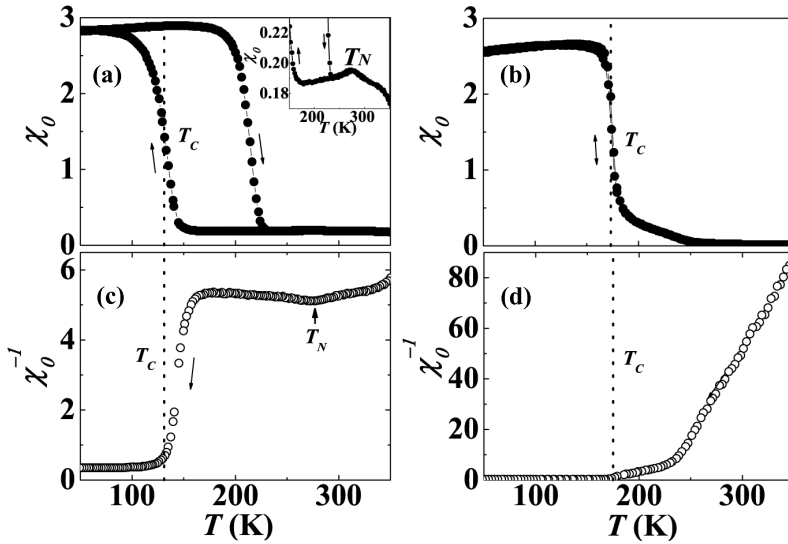
Figure 6.2: Bulk magnetic susceptibility (unitless) for $Mn_{1.00}Fe_{0.95}P_{0.67}Si_{0.33}$ (a) and $Mn_{1.70}Fe_{0.25}P_{0.50}Si_{0.50}$ (b). The corresponding inverse susceptibility is shown in (c) and (d), respectively.

by the neutron (Sec. 6.4) and experiments (Sec. 6.5).

Figure 6.3 shows the contour plots of the X-ray diffraction patterns measured on cooling for the two compounds. The discontinuous and continuous shift in the peak position manifests the first- and second-order phase transition in the $Mn_{1.00}Fe_{0.95}P_{0.67}Si_{0.33}$ and $Mn_{1.70}Fe_{0.25}P_{0.50}Si_{0.50}$ compounds, respectively. The coincidence of structural (see Fig. 6.3) and magnetic (see Fig. 6.2) transitions characterizes the strong magnetoelastic coupling in $(Mn,Fe)_2(P,Si)$ compounds. The lattice parameters derived from Rietveld refinement are presented in Fig. 6.4. The anomalous thermal evolution of the lattice parameters close to T_C in the PM regime, which is a common feature in $(Mn,Fe)_2(P,Si)$ compounds [7, 22], reflects the development of magnetic correlations.

6
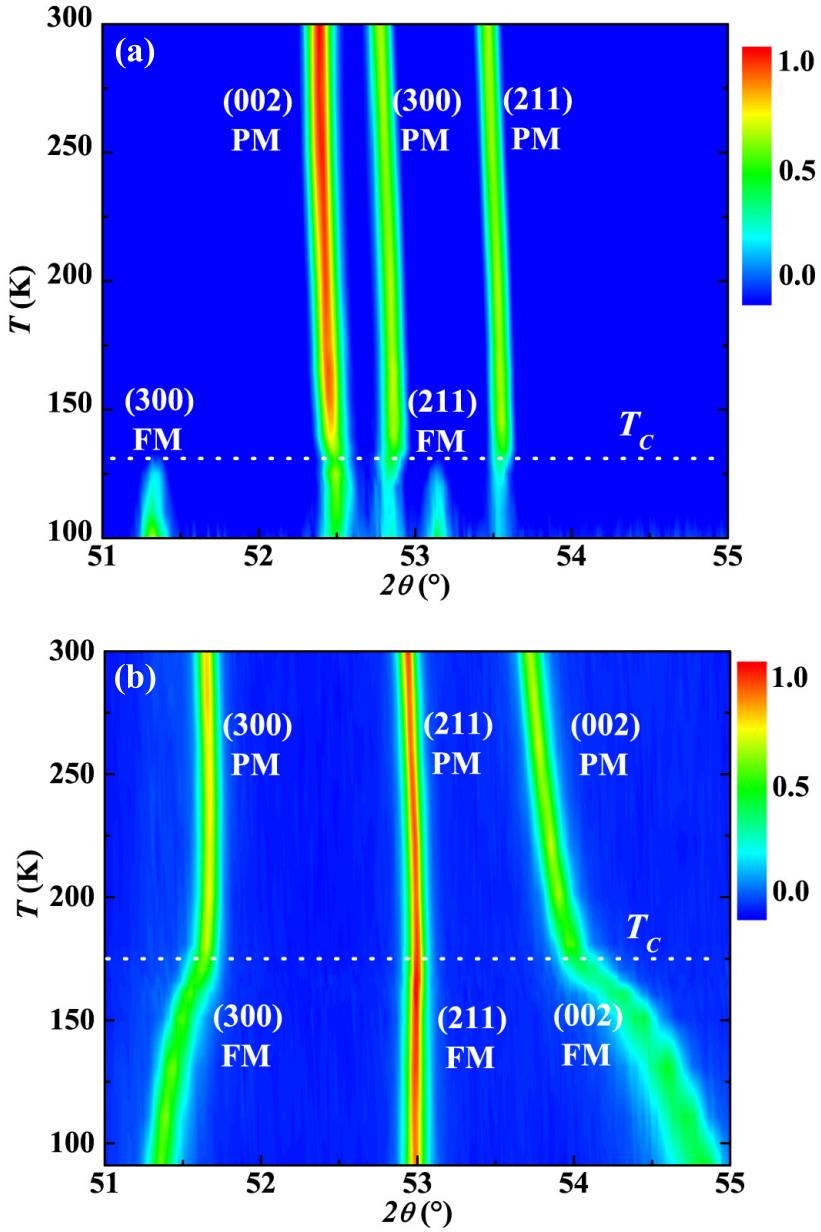
Figure 6.3: Contour plots of the X-ray diffraction patterns measured on cooling for $\mathrm{Mn_{1.00}Fe_{0.95}P_{0.67}Si_{0.33}}$ (a) and $\mathrm{Mn_{1.70}Fe_{0.25}P_{0.50}Si_{0.50}}$ (b). The color bar on the right represents the normalized intensity scale.
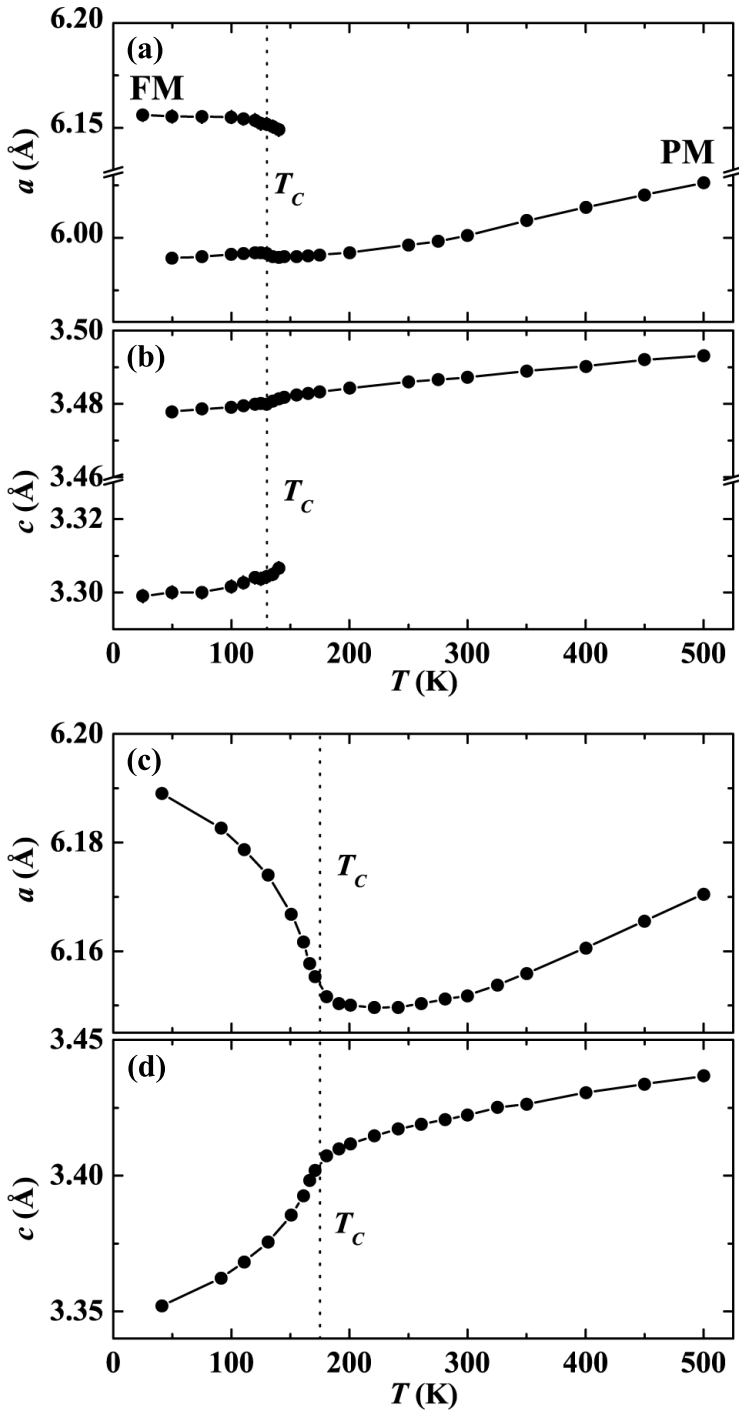
Figure 6.4: Lattice parameters derived from X-ray diffraction for $Mn_{1.00}Fe_{0.95}P_{0.67}Si_{0.33}$ (a-b) and $Mn_{1.70}Fe_{0.25}P_{0.50}Si_{0.50}$ (c-d).

6.4. NEUTRON POLARIZATION ANALYSIS

POLARIZED neutron scattering experiments were performed in the PM regime of the $\text{Mn}_{1.00}\text{Fe}_{0.95}\text{P}_{0.67}\text{Si}_{0.33}$ and $\text{Mn}_{1.70}\text{Fe}_{0.25}\text{P}_{0.50}\text{Si}_{0.50}$ compounds. Fig. 6.5(a) shows the separate magnetic and nuclear scattering cross section at 500 K for the $\text{Mn}_{1.00}\text{Fe}_{0.95}\text{P}_{0.67}\text{Si}_{0.33}$ compound. The clear forward (low-Q) magnetic scattering indicates the presence of weak short-range FM correlations at 500 K (about $3.8T_C$). [12, 23] The magnetic scattering cross section measured at 175 K (see Fig. 6.5(b)) shows a weak peak at $Q \approx 0.4$ Å^{-1}. A similar neutron-diffraction peak has been observed in certain $(\text{Mn,Fe})_2(\text{P,Si})$ compositions, originating from weak incommensurate AFM order (see *Chapter 7*). The nuclear scattering cross section shows slight changes in the peak positions with decreasing temperature due to thermal expansion.

6

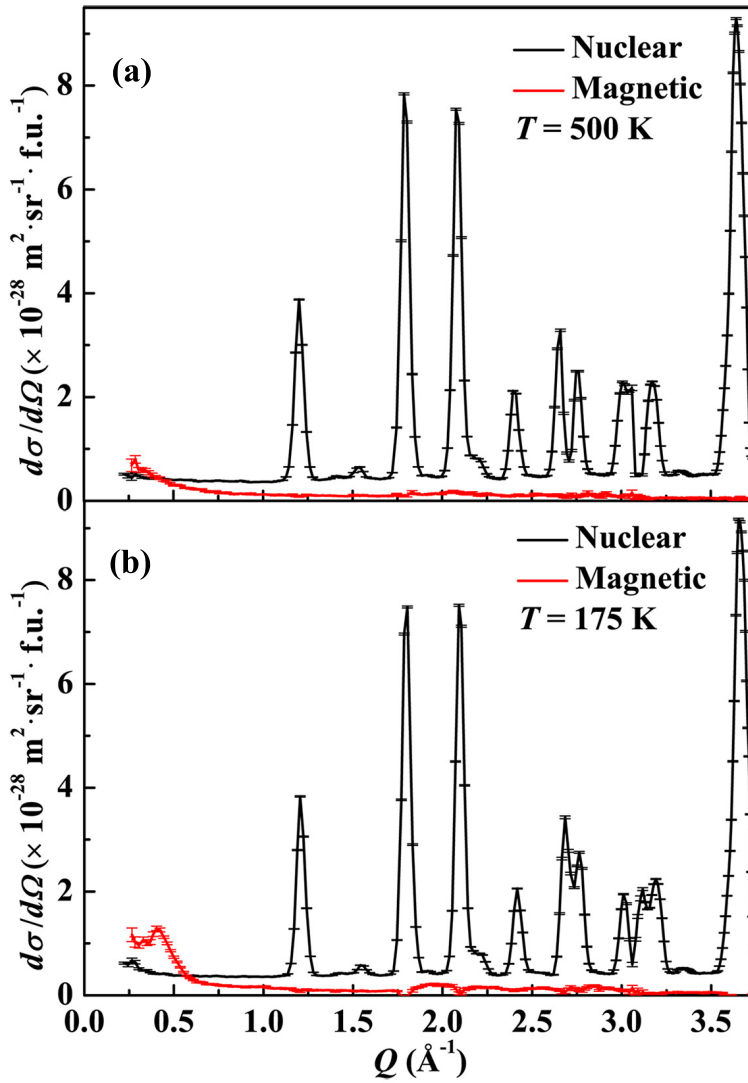Figure 6.5: Magnetic and nuclear scattering cross section for $Mn_{1.00}Fe_{0.95}P_{0.67}Si_{0.33}$ measured at 500 K (a) and 175 K (b).
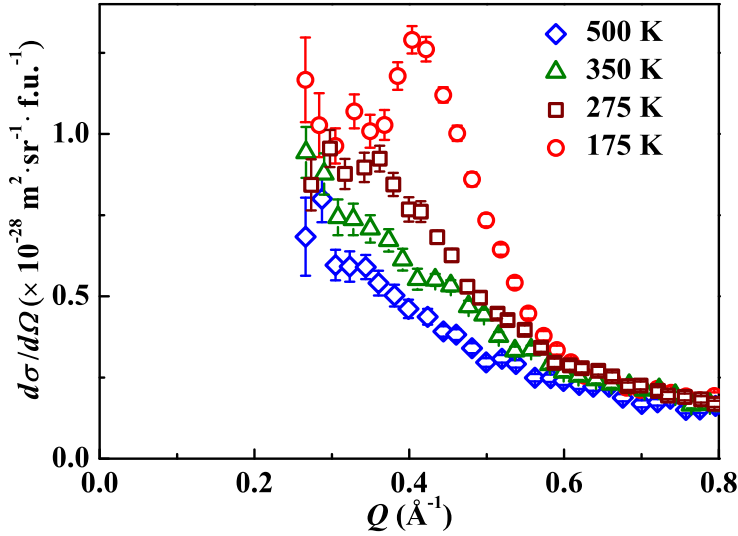
Figure 6.6: Magnetic scattering cross section as a function of temperature for $Mn_{1.00}Fe_{0.95}P_{0.67}Si_{0.33}$.

In order to explore the evolution of magnetic correlations in detail for the $Mn_{1.00}Fe_{0.95}P_{0.67}Si_{0.33}$ compound, the magnetic scattering cross section is plotted at different temperatures upon cooling in Fig. 6.6. The forward scattering becomes more pronounced when the sample is cooled from 500 to 350 K, which is due to the development of magnetic correlations. However, AFM order [23] appears at 275 K, as suggested by the weak peak at $Q \approx 0.36$ Å^{-1}. With a further decrease in temperature, the peak intensity significantly increases and the peak position shifts to larger Q values. This reveals the enhancement of AFM order and variations in the propagation vector of the incommensurate AFM structure. The detected AFM order is consistent with the susceptibility measurements (see the inset of Fig. 6.2 (a)) and the neutron diffraction experiments in *Chapter 7*.

In contrast to the $Mn_{1.00}Fe_{0.95}P_{0.67}Si_{0.33}$ compound, only FM correlations are detected in the $Mn_{1.70}Fe_{0.25}P_{0.50}Si_{0.50}$ compound at 500 and 180 K, as indicated by the forward neutron diffuse scattering [23] in Fig. 6.7(a) and (b). The FM correlations are enhanced with decreasing temperature, manifested by the increasing intensity of the forward scattering in Fig. 6.8(a).

Figure 6.7: Magnetic and nuclear scattering cross section for $Mn_{1.70}Fe_{0.25}P_{0.50}Si_{0.50}$ measured at 500 K (a) and 180 K (b).
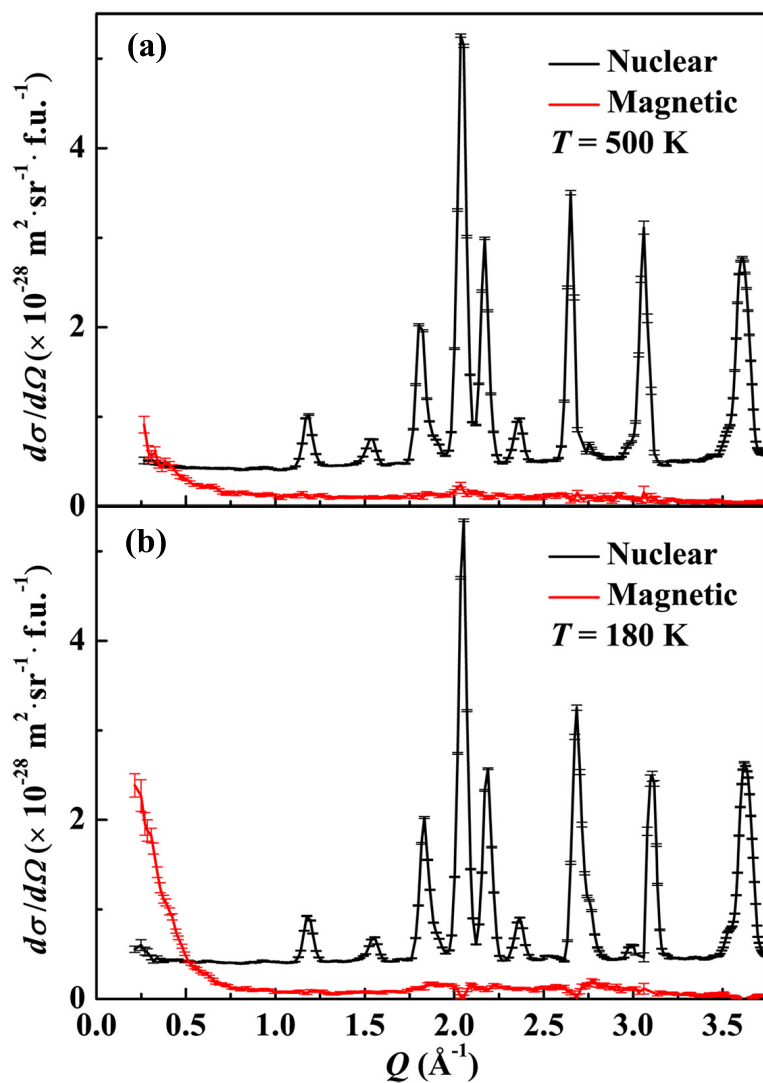
6
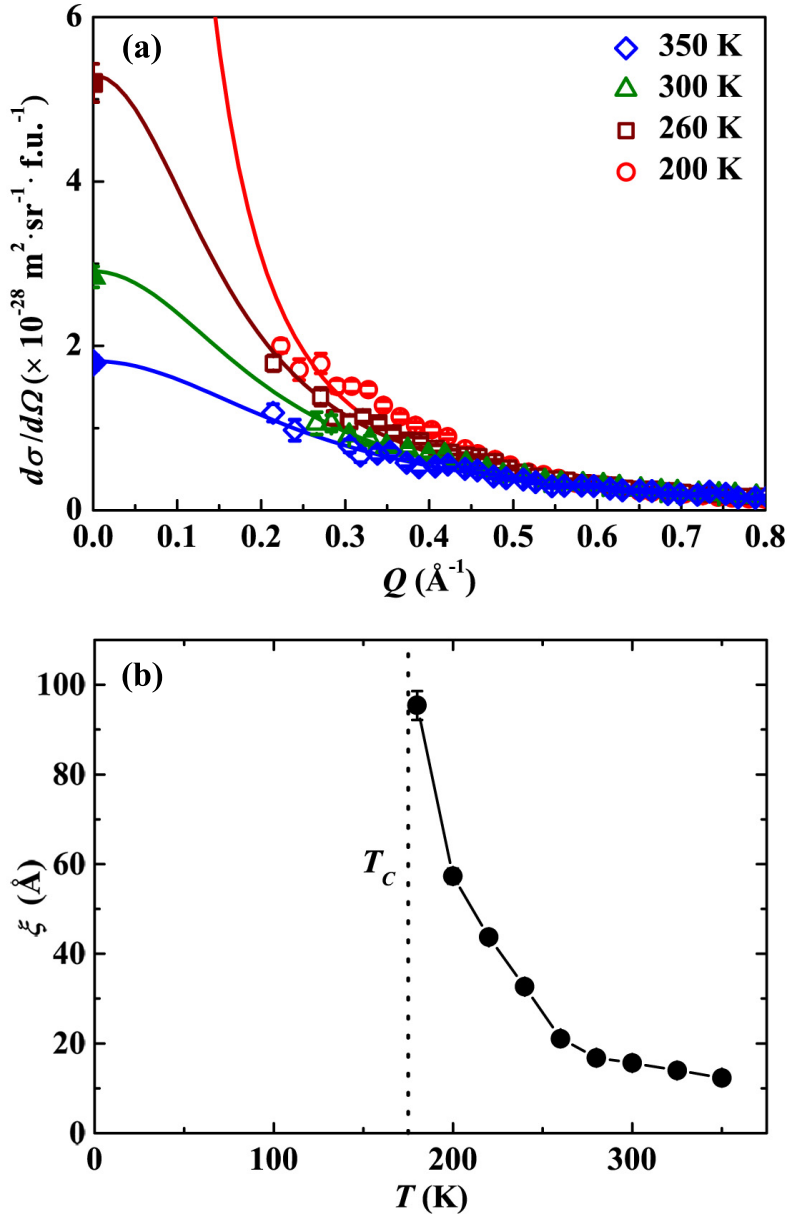
Figure 6.8: Magnetic scattering cross section (a) and the derived magnetic correlation length (b) as a function of temperature for $Mn_{1.70}Fe_{0.25}P_{0.50}Si_{0.50}$. The solid lines in (a) represent fits to the data.

It is assumed that scattering cross sections outside the detection energy window of the D7 diffractometer are negligible. The magnetic cross section in the vicinity of $Q = 0$ for a paramagnetic phase is approximately given by [24]

$$\frac{d\sigma}{d\Omega}(Q) = \frac{2}{3} N \left(\frac{g_n r_0}{4\mu_B} \right)^2 \frac{k_B T M}{\rho N_A \mu_0} \chi(Q) \tag{6.1}$$

where N is the number of magnetic atoms per formula unit, g_n is the neutron g-factor, r_0 is the classical electron radius, μ_B is the Bohr magneton, k_B is the Boltzmann constant, M is the molar mass, ρ is the volumetric-mass density, N_A is the Avogadro constant, μ_0 is the permeability of vacuum, and $\chi(Q)$ is the magnetic susceptibility. The Q-dependence of $\chi(Q)$ is thereafter assumed to be a Lorentzian function. The $\chi(Q \to 0)$ equals the bulk magnetic susceptibility, i.e. the χ_0 shown in Fig. 6.2. As a result, the $\frac{d\sigma}{d\Omega}(0)$ at different temperatures can be calculated from χ_0 using Eq. 6.1.

The forward scattering cross section in Fig. 6.8(a) can be fitted well with the convolution of a Gaussian (instrument resolution[25, 26] with a full width at half maximum of about 0.06 Å^{-1} in the vicinity of $Q = 0$) and the Lorentzian (sample contribution) function. From the full width at half maximum ΔQ of the Lorentzian function, the magnetic correlation length $\xi = 2\pi/\Delta Q$ can be derived at different temperatures. As shown in Fig. 6.8(b), at 350 K (= $2.0 T_C$), the FM correlation length in the $Mn_{1.70}Fe_{0.25}P_{0.50}Si_{0.50}$ compound is 12.4 Å, which is comparable with $\xi = 13.0$ Å observed at $T = 2.1 T_C$ for the Fe_2P compound [12]. The value of ξ rises with the decrease in temperature and reaches 31.6 Å at 240 K (= $1.4 T_C$) for the $Mn_{1.70}Fe_{0.25}P_{0.50}Si_{0.50}$ compound, which is much larger than the $\xi = 16.6$ Å observed at $T = 1.4 T_C$ for the Fe_2P compound [12]. The correlation length further increases to 95.8 Å at 180 K in the $Mn_{1.70}Fe_{0.25}P_{0.50}Si_{0.50}$ compound. The thermal-evolution of the correlation length provides clear evidence for the spatial development of magnetic correlations in the PM regime for $(Mn,Fe)_2(P,Si)$ compounds.

6

6.5. MUON-SPIN RELAXATION ANALYSIS

THE dynamics of the magnetic correlations above T_C was studied by means of muon-spin relaxation experiments for the two compounds.

In the zero-field μSR geometry, when the strength of the static local magnetic field is assumed to show a Gaussian distribution, the muon-spin relaxation function is described by the so-called Kubo-Toyabe function [27, 28]

$$A^{stat}(t) = A_0 \left[\frac{1}{3} + \frac{2}{3}(1 - \gamma_\mu^2 \Delta^2 t^2) \exp\left(\frac{-\gamma_\mu^2 \Delta^2 t^2}{2} \right) \right] \qquad (6.2)$$

where A_0 is the initial asymmetry, γ_μ is the gyromagnetic ratio of the muon $(8.51616 \times 10^8$ rad·s^{-1}T$^{-1})$ and Δ is the standard deviation of the Gaussian field distribution.

Muon diffusion and the fluctuations of the local field will cause dynamics of the muon-spin relaxation. This can be evaluated within the framework of the strong collision model [28–31]. In the slow dynamic limit, the muon-spin relaxation is derived as [28–31]

$$A^{dyn}(t) = A_0 \left[\frac{1}{3} \exp\left(-\frac{2}{3}\nu t \right) + \frac{2}{3} \left(1 - \gamma_\mu^2 \Delta^2 t^2 \right) \exp\left(\frac{-\gamma_\mu^2 \Delta^2 t^2}{2} \right) \right] \qquad (6.3)$$

where ν is the local-field correlation frequency due to the muon diffusion and the local-field fluctuations. In the fast dynamic limit, the muon-spin relaxation function is written as [28–31]

$$A^{dyn}(t) = A_0 \exp(-\lambda t) \qquad (6.4)$$

where λ is the muon-spin relaxation rate.

Considering the large nuclear magnetic moment of Mn and P, nuclear magnetic fields as well as the magnetic fields due to the unpaired electrons of Mn and Fe are probed by the implanted muons. Muon diffusion will cause dynamics for the nuclear contribution. As a first approximation, a slow-dynamics behavior was assumed for the nuclear contribution, which is described by Eq. 6.3. As for the muon-spin relaxation of electronic origin, its dynamics can be caused by the fluctuations of the magnetic correlations. The electronic contribution above T_C is expected to be dominated by fast dynamics, which is described by Eq. 6.4. The nuclear and electronic contributions are independent, and hence the zero-field μSR spectra measured above T_C are fitted by a product of Eqs. 6.3 and 6.4. Fits for both compounds show that muon diffusion is present above 325 K, while it becomes negligible below 325 K. This indicates a static nuclear contribution below 325 K, where the μSR spectra can be fitted by a product of Eqs. 6.2 and 6.4. As
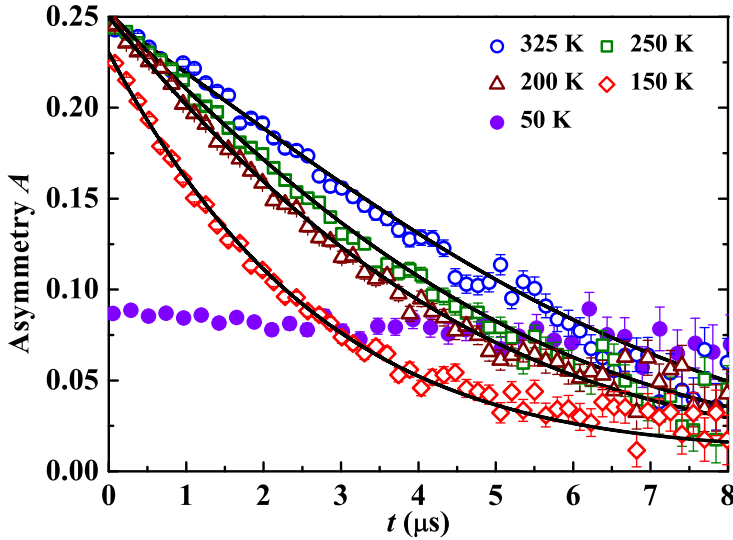
Figure 6.9: Zero-field μSR spectra for $Mn_{1.00}Fe_{0.95}P_{0.67}Si_{0.33}$. The solid lines represent fits to the data.

a consequence, the fluctuations of the magnetic correlations can be unambiguously extracted from the zero-field μSR spectra below 325 K.

Figure 6.9 shows the zero-field μSR spectra measured below 325 K for $Mn_{1.00}Fe_{0.95}P_{0.67}Si_{0.33}$. Above T_C ($\approx$ 130 K), the spectra show a fast damping behavior, suggesting dynamic magnetic fields experienced by the muons. Below T_C, the initial asymmetry in the spectrum drops to 1/3 of that in the PM state without showing any oscillation signals. This reflects the broad distribution of local magnetic fields at different muon sites in the magnetically-ordered polycrystalline sample. The standard deviation of the nuclear field distribution Δ_n derived from the fits is about 0.13 mT. The initial asymmetry in Fig. 6.10(a) shows a decrease for temperatures close to T_C, which suggests that the sample is not magnetically homogeneous due to compositional inhomogeneity. There is also the possibility that the slowing down of the magnetic fluctuations is so strong that the motional narrowing limit assumed by the Eq. 6.4 is no longer valid. The muon-spin relaxation rate, presented in Fig. 6.10(b), gradually increases as T_C is approached from the high-temperature side.

6

Figure 6.10: Temperature dependence of initial asymmetry A_0 (a) and muon-spin relaxation rate λ (b) for $Mn_{1.00}Fe_{0.95}P_{0.67}Si_{0.33}$.

6
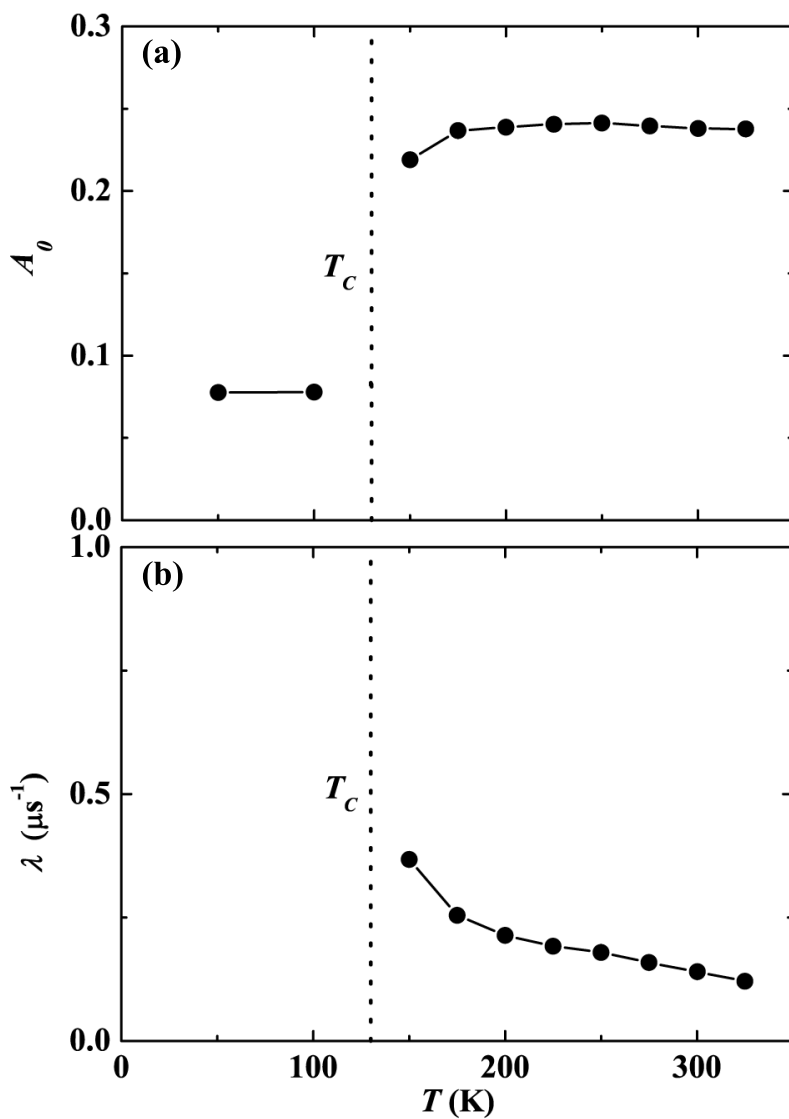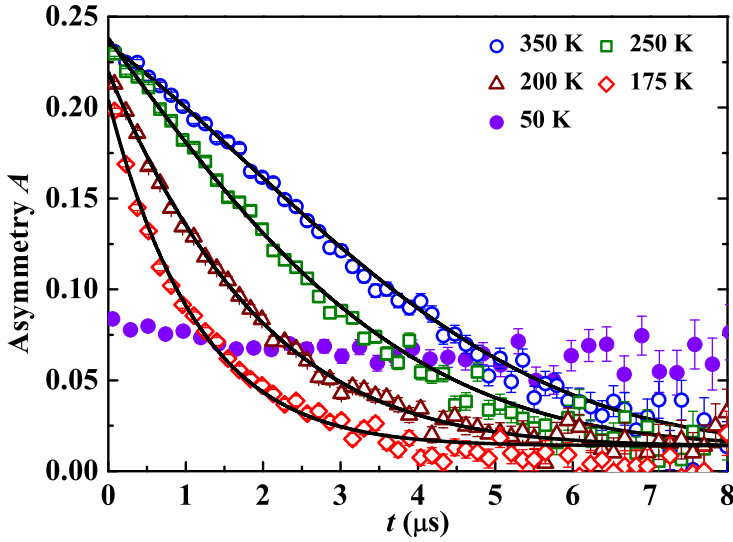
Figure 6.11: Zero-field μSR spectra for $Mn_{1.70}Fe_{0.25}P_{0.50}Si_{0.50}$. The solid lines represent fits to the data.

As shown in Fig. 6.11, the $Mn_{1.70}Fe_{0.25}P_{0.50}Si_{0.50}$ compound shows similar μSR spectra as the $Mn_{1.00}Fe_{0.95}P_{0.67}Si_{0.33}$ compound. The same fitting model is employed and the derived parameters are presented in Fig. 6.12. The standard deviation of the nuclear field distribution Δ_n is about 0.21 mT for the $Mn_{1.70}Fe_{0.25}P_{0.50}Si_{0.50}$ compound. As shown in Fig. 6.12(a), the initial asymmetry starts to decrease above T_C, which is similar to that for the $Mn_{1.00}Fe_{0.95}P_{0.67}Si_{0.33}$ compound. This may be caused by compositional inhomogeneity or indicating that our assumption of motional narrowing limit is no longer applicable. The muon-spin relaxation rate increases with decreasing temperature and tends to diverge close to T_C (see Fig. 6.12(b)).

For isotropic ferromagnetic dynamical correlations with a well-developed maximum of $\chi(Q)$ at $Q = 0$ and assuming a Lorentzian spectral-weight function, the muon-spin relaxation rate measured in zero magnetic field can be written as [31]

$$\lambda = \frac{\mu_0 \gamma_\mu^2}{\pi^2} \left[\left(p - \frac{1}{3} \right)^2 + \frac{2}{9} \right] k_B T \int \chi(Q) \frac{Q^2}{\Gamma_0(Q)} dQ \qquad (6.5)$$

where the p is a constant that depends on the hyperfine constant and the number of neighboring ions coupled to the muon spin through the hyperfine field. As a first approximation, the value of $\left(p - \frac{1}{3} \right)^2 + \frac{2}{9}$ is assumed to be 1, taken as a realistic order of magnitude [31] for the materials studied here. $\Gamma_0(Q)$ is the magnetic
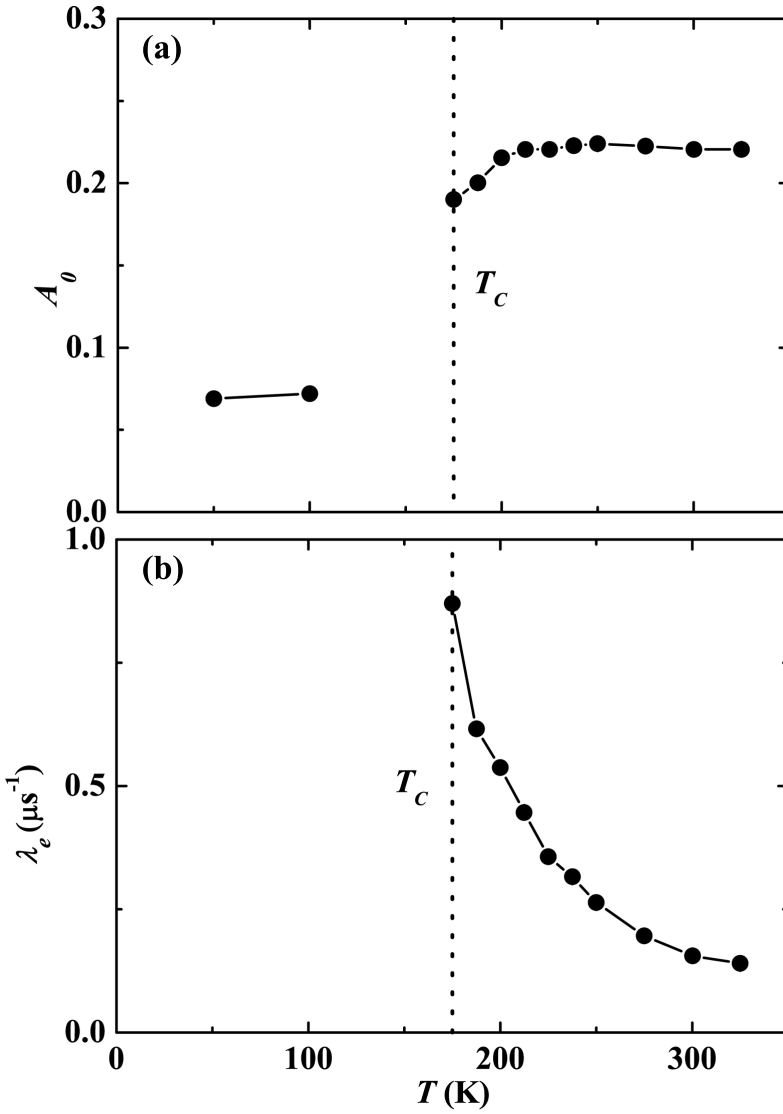
Figure 6.12: Temperature dependence of initial asymmetry A_0 (a) and muon-spin relaxation rate λ (b) for $\text{Mn}_{1.70}\text{Fe}_{0.25}\text{P}_{0.50}\text{Si}_{0.50}$.
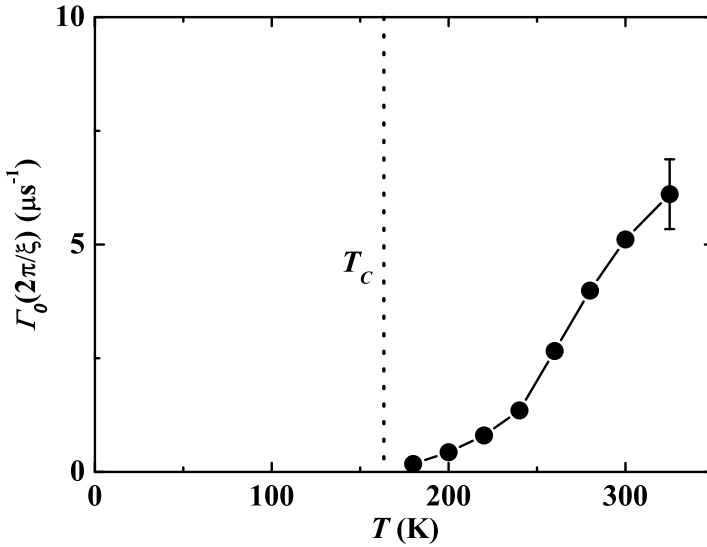
Figure 6.13: Temperature dependence of the magnetic relaxation rate for $Mn_{1.70}Fe_{0.25}P_{0.50}Si_{0.50}$.

fluctuation rate at wave vector Q.

Since short-range magnetic correlations have been clearly observed from neutron diffraction experiments (see Fig. 6.8), $\Gamma_0(Q)$ should be dominated by spin-conserved dynamics [31, 32]. It is assumed that $\hbar\Gamma_0(Q) = D_{sd}Q^2$, i.e. neglecting the high-order terms in Q, [31, 32] where D_{sd} is a proportionality factor. From Eqs. 6.1 and 6.5, the value of Γ_0 for the magnetic correlation with a correlation length of ξ is derived as:

$$\Gamma_0\left(\frac{2\pi}{\xi}\right) = \frac{C}{\hbar}\frac{\int \frac{d\sigma}{d\Omega}(Q)dQ}{\lambda}\left(\frac{2\pi}{\xi}\right)^2 \tag{6.6}$$

where $C = 6.04 \times 10^{-24}$ J·m·s^{-1}. The $\frac{d\sigma}{d\Omega}(Q)$, ξ and λ for the $Mn_{1.70}Fe_{0.25}P_{0.50}Si_{0.50}$ compound are presented in Figs. 6.8(a), 6.8(b) and 6.12(b), respectively. The magnetic relaxation rate Γ_0 is calculated at different temperatures and presented in Fig. 6.13.

The magnetic relaxation rate decreases with decreasing temperature, which characterizes the slowing down of magnetic fluctuations in the PM regime of the $Mn_{1.70}Fe_{0.25}P_{0.50}Si_{0.50}$ compound when T_C is approached. The magnetic correlation time $\tau = 1/\Gamma_0(2\pi/\xi)$ is in the microsecond time range at temperatures
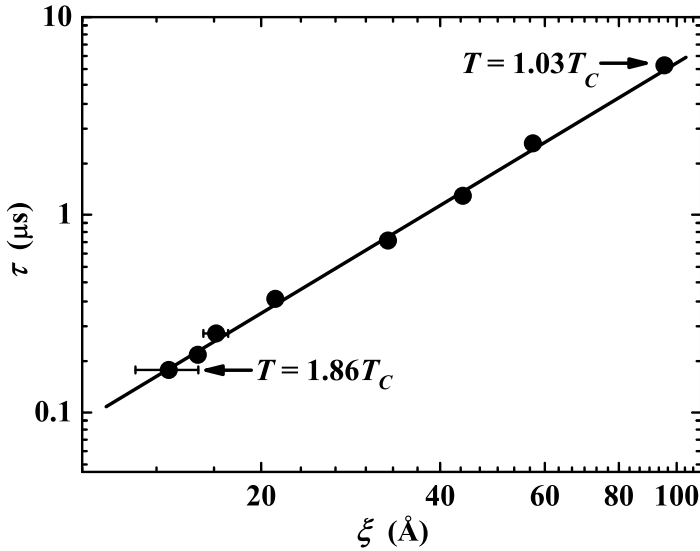
Figure 6.14: Relation between the correlation time and correlation length for $\text{Mn}_{1.70}\text{Fe}_{0.25}\text{P}_{0.50}\text{Si}_{0.50}$. The solid line represents a fit to the data.

$1.03\,T_C \leqslant T \leqslant 1.86\,T_C$ for the $\text{Mn}_{1.70}\text{Fe}_{0.25}\text{P}_{0.50}\text{Si}_{0.50}$ compound, while no correlations with τ longer than 10^{-10} s were detected at $T \geqslant 1.05\,T_C$ for the Fe_2P compound. This confirms stronger magnetic correlations in the $(\text{Mn},\text{Fe})_2(\text{P},\text{Si})$ compound than in the Fe_2P compound. As presented in Fig. 6.14, $\tau \propto \xi^n$ shows a power-law dependence on ξ with an exponent $n = 1.8(0.1)$. Comparing this scaling behavior with Eq. 6.6, it suggests that the ratio between $\int \frac{d\sigma}{d\Omega}(Q)dQ$ and λ is weakly temperature-dependent. With the neutron and muon data at hand, we cannot extracted the correlation time and correlation length above T_C for the $\text{Mn}_{1.00}\text{Fe}_{0.95}\text{P}_{0.67}\text{Si}_{0.33}$ compound due to the appearance of the unexpected intermediate AFM phase.

6

6.6. ROLE OF MAGNETIC CORRELATIONS IN THE MAGNETOE-LASTIC TRANSITION

THE magnetoelastic transition in $(\text{Mn},\text{Fe})_2(\text{P},\text{Si})$ compounds is accompanied by a metamagnetic transition, i.e. a transition from a low-moment state to a high-moment state for the Fe atoms [2, 7]. In contrast, the magnetic moment of the Mn atoms (about 2.6 μ_B) is preserved when crossing the FM-PM transi-

tion [2, 7]. The local magnetic field exerted on the Fe atoms by the Mn atoms triggers the moment formation and magnetic order.[7, 21] Therefore, magnetic correlations between Mn atoms in the PM state will enhance the local magnetic field, promote the formation of Fe magnetic moment and will finally result in long-range magnetic order.

The combination of polarized neutron diffraction and μSR experiments reveals the presence of short-range magnetic correlations in the PM state of $(Mn,Fe)_2(P,Si)$ compounds. This causes a deviation of the PM susceptibility from the Curie-Weiss law, since the molecular field approximation neglects the magnetic correlations in the PM state. The increasing correlation length and slowing down of the magnetic fluctuations with decreasing temperature reflects the enhanced magnetic correlations. Compared to Fe_2P, the $(Mn,Fe)_2(P,Si)$ compound shows stronger magnetic correlations in the paramagnetic state, which benefits the strong metamagnetic transition responsible for the giant magnetocaloric effect. Consequently, the formation and development of short-range magnetic correlations in the PM state plays a crucial role in the magnetoelastic transition in $(Mn,Fe)_2(P,Si)$ compounds.

6.7. Conclusions

THE xyz neutron polarization and muon-spin relaxation studies on $(Mn,Fe)_2(P,Si)$ reveal, both on the length- and time-scales, the presence of short-range magnetic correlations in the PM regime. The short-range magnetic correlations develop in space and slow down with decreasing temperature, and finally become long-range and static at T_C. This study provides a better understanding of the magnetoelastic phase transition in Fe_2P-type compounds.

References

[1] X. F. Miao, L. Caron, P. Roy, N. H. Dung, L. Zhang, W. A. Kockelmann, R. A. de Groot, N. H. van Dijk, and E. Brück, *Tuning the phase transition in transition-metal-based magnetocaloric compounds,* Phys. Rev. B **89**, 174429 (2014).

[2] N. H. Dung, Z. Q. Ou, L. Caron, L. Zhang, D. T. Cam Thanh, G. A. de Wijs, R. A. de Groot, K. H. J. Buschow, and E. Brück, *Mixed magnetism for refrigeration and energy conversion,* Adv. Energy Mater. **1**, 1215 (2011).

[3] F. Guillou, G. Porcari, H. Yibole, N. H. van Dijk, and E. Brück, *Taming the first-order transition in giant magnetocaloric materials,* Adv. Mater. **26**, 2671 (2014).

[4] M. J. Neish, M. P. Oxley, J. Guo, B. C. Sales, L. J. Allen, and M. F. Chisholm,

Local observation of the site occupancy of Mn in a MnFePSi compound, Phys. Rev. Lett. **114**, 106101 (2015).

[5] X. F. Miao, L. Caron, Z. Gercsi, A. Daoud-Aladine, N. H. van Dijk, and E. Brück, *Thermal-history dependent magnetoelastic transition in (Mn,Fe)$_2$ (P,Si),* Appl. Phys. Lett. **107**, 042403 (2015).

[6] Z. Q. Ou, L. Zhang, N. H. Dung, L. van Eijck, A. M. Mulders, M. Avdeev, N. H. van Dijk, and E. Brück, *Neutron diffraction study on the magnetic structure of Fe$_2$P-based Mn$_{0.66}$Fe$_{1.29}$P$_{1-x}$Si$_x$ melt-spun ribbons,* J. Magn. Magn. Mater. **340**, 80 (2013).

[7] N. H. Dung, L. Zhang, Z. Q. Ou, L. Zhao, L. van Eijck, A. M. Mulders, M. Avdeev, E. Suard, N. H. van Dijk, and E. Brück, *High/low-moment phase transition in hexagonal Mn-Fe-P-Si compounds,* Phys. Rev. B **86**, 045134 (2012).

[8] O. Beckman and L. Lundgren, in *Handbook of Magnetic Materials,* edited by K. H. J. Buschow (North-Holland, Amsterdam, 1991), Vol. 6, pp. 181-287 .

[9] R. Zach, M. Guillot, and R. Fruchart, *The influence of high magnetic fields on the first order magneto-elastic transition in MnFe(P$_{1-y}$As$_y$) systems,* J. Magn. Magn. Mater. **89**, 221 (1990).

[10] H. Yabuta, K. Umeo, T. Takabatake, K. Koyama, and K. Watanabe, *Temperature- and field-induced first-order ferromagnetic transitions in MnFe(P$_{1-x}$Ge$_x$),* J. Phys. Soc. Jpn. **75**, 113707 (2006).

[11] H. Fujii, Y. Uwatoko, K. Motoya, Y. Ito, and T. Okamoto, *Neutron scattering investigation of itinerant electron system Fe$_2$P,* J. Phys. Soc. Jpn. **57**, 2143 (1988).

[12] C. Wilkinson, R. Wäppling, and K. R. A. Ziebeck, *Spin fluctuations in Fe$_2$P above its Curie temperature,* J. Magn. Magn. Mater. **78**, 269 (1989).

[13] R. Wäppling, O. Hartmann, E. Wackelgard, and T. Sundqvist, *µSR study of Fe$_2$P in the paramagnetic state,* J. Magn. Magn. Mater. **50**, 347 (1985).

[14] H. Yamada and K. Terao, *First-order transition of Fe$_2$P and anti-metamagnetic transition,* Phase Transit. **75**, 231 (2002).

[15] O. Schärpf and H. Capellmann, *The xyz-difference method with polarized neutrons and the separation of coherent, spin incoherent, and magnetic scattering cross sections in a multidetector,* Phys. Stat. Sol. (a) **135**, 359 (1993).

6

[16] J. R. Stewart, P. P. Deen, K. H. Andersen, H. Schober, J. F. Barthélémy, J. M. Hillier, A. P. Murani, T. Hayes, and B. Lindenau, *Disordered materials studied using neutron polarization analysis on the multi-detector spectrometer, D7*, J. Appl. Cryst. **42**, 69 (2009).

[17] G. Ehlers, J. R. Stewart, A. R. Wildes, P. P. Deen, and K. H. Andersen, *Generalization of the classical xyz-polarization analysis technique to out-of-plane and inelastic scattering*, Rev. Sci. Instrum. **84**, 093901 (2013).

[18] J. Rodríguez-Carvajal, *Recent advances in magnetic structure determination by neutron powder diffraction*, Physica B **192**, 55 (1993).

[19] N. H. Dung, L. Zhang, Z. Q. Ou, and E. Brück, *From first-order magneto-elastic to magneto-structural transition in (Mn,Fe)$_{1.95}$P$_{0.50}$Si$_{0.50}$ compounds*, Appl. Phys. Lett. **99**, 092511 (2011).

[20] T_C is defined as the temperature where the first derivative of susceptibility with respect to the temperature reaches a maximum .

[21] E. K. Delczeg-Czirjak, M. Pereiro, L. Bergqvist, Y. O. Kvashnin, I. Di Marco, G. Li, L. Vitos, and O. Eriksson, *Origin of the magnetostructural coupling in FeMnP$_{0.75}$Si$_{0.25}$*, Phys. Rev. B **90**, 214436 (2014).

[22] N. H. Dung, L. Zhang, Z. Q. Ou, and E. Brück, *Magnetoelastic coupling and magnetocaloric effect in hexagonal Mn-Fe-P-Si compounds*, Scripta Mater. **67**, 975 (2012).

[23] T. J. Hicks, *Magnetism in Disorder*, Oxford Series on Neutron Scattering in Condensed Matter (Oxford University Press, New York, 1995).

[24] S. Lovesey, *Theory of neutron scattering from condensed matter*, International series of monographs on physics, Vol. 2 (Clarendon Press, Oxford, 1984).

[25] G. Caglioti, A. Paoletti, and F. P. Ricci, *Choice of collimators for a crystal spectrometer for neutron diffraction*, Nucl. Instr. **3**, 223 (1958).

[26] A. W. Hewat, *Design for a conventional high-resolution neutron powder diffractometer*, Nucl. Instrum. Methods **127**, 361 (1975).

[27] R. Kubo and T. Toyabe, *A stochastic model for low field resonance and relaxation*, in *Magnetic resonance and relaxation*, edited by R. Blinc (North-Holland) p. 810.

6

[28] R. S. Hayano, Y. J. Uemura, J. Imazato, N. Nishida, T. Yamazaki, and R. Kubo, *Zero- and low-field spin relaxation studied by positive muons,* Phys. Rev. B **20**, 850 (1979).

[29] A. Keren, *Generalization of the abragam relaxation function to a longitudinal field,* Phys. Rev. B **50**, 10039 (1994).

[30] P. Dalmas de Réotier and A. Yaouanc, *Quantum calculation of the muon depolarization function: effect of spin dynamics in nuclear dipole systems,* J. Phys.: Condens. Matter **4**, 4533 (1992).

[31] A. Yaouanc and P. Dalmas de Réotier, *Muon spin rotation, relaxation, and resonance: applications to condensed matter,* International Series of Monographs on Physics (Oxford University Press, New York, 2011).

[32] F. Mezei, *Critical dynamics in isotropic ferromagnets,* J. Magn. Magn. Mater. **45**, 67 (1984).

6

7

KINETIC-ARREST INDUCED PHASE COEXISTENCE AND METASTABILITY IN SOME (MN,FE)₂(P,SI) COMPOUNDS

Neutron diffraction, Mössbauer spectroscopy, magnetometry, and in-field X-ray diffraction are employed to investigate the magnetoelastic phase-transition in hexagonal (Mn,Fe)₂(P,Si) compounds. (Mn,Fe)₂(P,Si) compounds undergo for certain compositions a second-order paramagnetic (PM) to a spin-density-wave (SDW) phase transition before further transforming into a ferromagnetic (FM) phase via a first-order phase transition. The SDW-FM transition can be kinetically arrested, causing the coexistence of FM and untransformed SDW phases at low temperatures. The in-field X-ray diffraction and magnetic relaxation measurements clearly reveal the metastability of the untransformed SDW phase. This unusual magnetic configuration originates from the strong magnetoelastic coupling and the mixed magnetism in hexagonal (Mn,Fe)₂(P,Si) compounds.

7.1. INTRODUCTION

FIRST-order magnetic phase transitions (FOMTs) in magnetic materials bring a variety of interesting phenomena such as giant magnetocaloric effect [1–3], colossal (or giant) magnetoresistance effect [4, 5] and magnetic shape memory effect [6]. The FOMT is characterized by a discontinuous change in the first derivative of the free energy (e.g., magnetization M, entropy S and volume V) triggered by thermodynamic variables (e.g., temperature T, magnetic field H and pressure P). Intrinsic composition disorder broadens the FOMT, causing a coexistence of transformed and untransformed phases over the phase transition region, as indicated by different nano- and micro-scale techniques [7–12] . After crossing the phase transition region, the system reaches an equilibrium state with a homogeneous phase.

Under certain conditions, the FOMT can be kinetically arrested, i.e., the phase coexistence remains beyond the FOMT region. An example of this behavior is reported for doped CeFe$_2$ alloys [13, 14]. When Ce(Fe$_{0.96}$Ru$_{0.04}$)$_2$ is cooled in an appropriate magnetic field, crossing the first-order ferromagnetic (FM) to antiferromagnetic (AFM) transition, the nucleation and growth of the low-T AFM phase is found to be hindered. As a result, a small fraction of the untransformed FM phase is frozen randomly in the stable AFM matrix at temperatures well below the Néel temperature T_N [13]. The supercooled FM phase is energetically metastable, which will be de-arrested and transformed to the stable AFM phase by thermal fluctuations.

A similar phenomenon has been reported in diverse classes of magnetic systems, such as Gd$_5$Ge$_4$ [15], Ni-Mn-X based Heusler alloys [16–18], doped-FeRh [19], Nd$_7$Rh$_{13}$ [20], Tb$_4$LuSi$_3$ [21] and manganites [22–26]. The kinetically-arrested phase transition is associated with a strong magnetostructural coupling in these magnetic systems. For instance, the high-T FM to low-T AFM transition in doped-CeFe$_2$ alloys [13, 14] is coupled with a cubic to rhombohedral structural transformation, while the high-T AFM to low-T FM transition in Gd$_5$Ge$_4$ [15] is accompanied by the Sm$_5$Ge$_4$-type orthorhombic to Gd$_5$Si$_4$-type orthorhombic structural transition.

Recent studies on hexagonal (Mn,Fe)$_2$(P,Si)-type compounds show the coexistence of FM and incommensurate magnetic phases at temperatures far below the T_C [27]. Höglin et al. [27] proposed that the phase coexistence in (Mn,Fe)$_2$(P,Si) originates from a phase segregation in the PM state. The sample consists of two phases with slightly different lattice parameters in the high-temperature PM state [27]. These two phases transform into a FM and an incommensurate magnetic phase upon cooling [27]. However, theoretical calculations revealed that the coexistence of a FM and an incommensurate magnetic phase may be a result of competing magnetic configurations [28, 29]. The incommensurate magnetic

phase is considered to be an intermediate metastable phase, which is formed due to the kinetic arrest of the PM-FM transition [29].

In the present work, the phase coexistence and metastability in some $(Mn,Fe)_2(P,Si)$-type compounds has been investigated using a combination of neutron diffraction, magnetometry, Mössbauer spectroscopy, and in-field X-ray diffraction. This provides further insight into the magnetoelastic coupling and mixed magnetism in $(Mn,Fe)_2(P,Si)$-type magnetocaloric alloys. This study also helps to extend the understanding of the kinetic arrest in FOMT magnetic systems.

7.2. Experimental

POLYCRYSTALLINE samples with nominal compositions $MnFe_{0.95}P_{0.67}Si_{0.33}$ (referred to as "S0"), $Mn_{1.30}Fe_{0.65}P_{0.67}Si_{0.33}$ ("S1"), $MnFe_{0.95}P_{0.71}Si_{0.29}$ ("S2") and $MnFe_{0.95}P_{0.67}Si_{0.33}N_{0.02}$ ("S3") samples were prepared from Mn, Fe, Fe_3N, red-P and Si powders as described in *Chapter 2*. Neutron diffraction experiments were performed on the WISH time of flight diffractometer at the ISIS Facility, Rutherford Appleton Laboratory, UK. The powered sample of about 6 g was put into a vanadium can mounted in a helium cryostat. Diffraction data were collected between 200 and 1.5 K upon cooling. The magnetic properties were characterized using a superconducting quantum interference device (SQUID) magnetometer (Quantum Design MPMS 5XL). X-ray powder diffraction experiments using Cu K_α radiation were performed at 300 and 10 K in magnetic fields up to 5 T [30]. Structure refinement of the X-ray and neutron diffraction patterns was performed using the Rietveld method implemented in the Fullprof package[31]. Transmission ^{57}Fe Mössbauer spectra were collected at 300 and 4.2 K with a sinusoidal velocity spectrometer using a ^{57}Co(Rh) source. The velocity calibration was carried out using an α-Fe foil. The source and the absorbing samples were kept at the same temperature during the measurements. The Mössbauer spectra were fitted using the Mosswinn 4.0 program [32].

7.3. Magnetization measurements

FIGURE 7.1(a) shows the temperature-dependent magnetization (M) of the as-prepared S0 sample during the first two cooling and warming cycles. A lower T_C upon the first cooling than on the second cooling is due to the "virgin effect", which is a common feature in $(Mn,Fe)_2(P,Si)$-type compounds [33]. The observed pronounced thermal hysteresis marks the strong first-order nature of the PM-FM phase transition in the S0 sample. After two cooling and warming cycles, *M-H* curves were measured isothermally at 5 K. The *M-H* curves in Fig. 7.1(b) shows a characteristic soft-ferromagnetic response with a saturation magnetization (M_s)
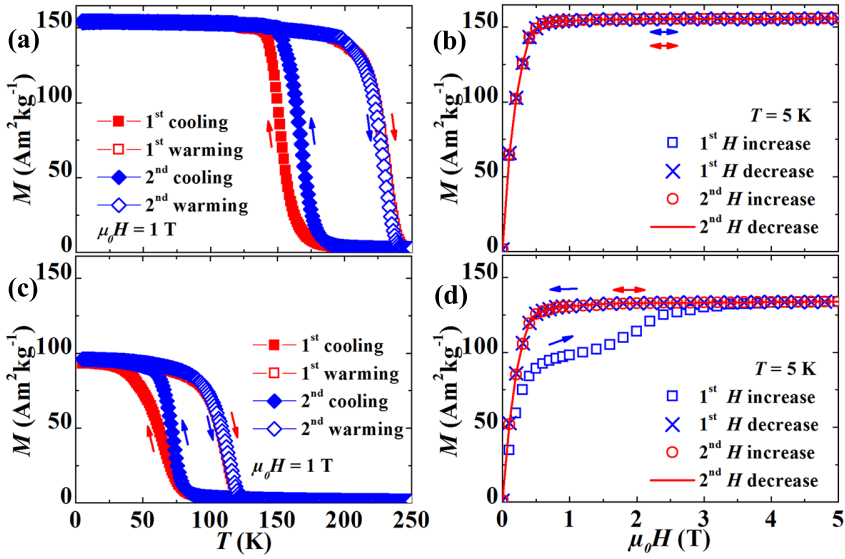
Figure 7.1: *M-T* and *M-H* plots for the S0 (a-b) and S1 (c-d) samples.

of about 155 Am^{2}kg^{-1} at 5 K, which is consistent with previous reports [34].

Previous studies reveal that the phase-transition temperature and the thermal hysteresis of the (Mn,Fe)$_2$(P,Si)-type compounds can be tuned directly by varying the Mn/Fe ratio [35]. With an increase in Mn/Fe ratio from 1.00/0.95 to 1.30/0.65, a rapid decrease in T_C and a reduction in thermal hysteresis is observed in Fig. 7.1(c). Additionally, the increase in the Mn/Fe ratio causes an unexpected and significant drop in the magnetization below T_C. As presented in Fig. 7.1(c), the PM-FM transition is complete at about 60 K for the second cooling. As a result, the S1 sample is expected to be at a pure FM state below 60 K. However, the isothermal *M-H* curve (Fig. 7.1(d)) measured at 5 K after the second cooling shows an unexpected metamagnetic transition when the field is applied for the first time. Below 1 T, the *M-H* curve shows a ferromagnet-like feature. Beyond 1 T, a metamagnetic transition appears and is completed at about 4 T. The decreasing-field curve does not show the reverse metamagnetic transition, nor does the subsequent increasing-field curve show any signature of the metamagnetic transition. Consequently, the initial magnetic state is not recovered after the first increase and decrease in field, suggesting the metastability of the initial magnetic state after cooling.

A similar phenomenon has been observed in a wide compositional range of (Mn,Fe)$_2$(P,Si)-type compounds. For instance, a metamagnetic transition is also present in the isothermal *M-H* curves of the S2 (Fig. 7.2(b)) and S3 (see
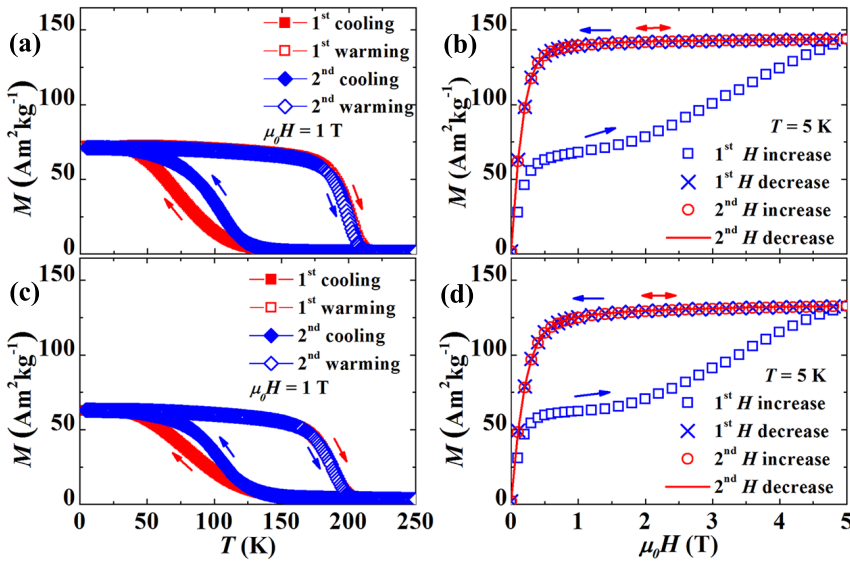
Figure 7.2: *M-T* and *M-H* plots for the as-prepared S2 (a-b), and S3 (c-d) samples.

Fig. 7.2(d)) samples, although the transition is still incomplete up to 5 T. Such anomalies have been observed in a variety of magnetic materials, and originate from incomplete FOMT caused by kinetic arrest [16, 23, 36]. One predominant consequence of the kinetic-arrest effect is the coexistence of transformed and untransformed phases at temperatures far below the phase-transition temperature. The neutron diffraction (Section 7.4) and Mössbauer spectroscopy (Section 7.5) studies provide experimental evidence for this phase coexistence in these $(Mn,Fe)_2(P,Si)$-type compounds.

7.4. NEUTRON DIFFRACTION

N EUTRON diffraction provides a direct and reliable way to determine crystallographic and magnetic structures. Neutron powder diffraction experiments were performed for the as-prepared S1 sample during cooling from 200 to 1.5 K. The contour plot in Fig. 7.3(a) shows the temperature-dependence of the diffraction pattern in the Q range from 1.95 to 2.55 Å^{-1}. At high temperatures, the diffraction peaks correspond to the crystal structure of the PM state, which crystallizes in the hexagonal Fe_2P-type structure (space group $P\bar{6}2m$). At $T \approx 50$ K, a series of new peaks appear beside the initial high-T peaks. The intensities of these new peaks increase with the decrease in temperature, while the intensities of the initial high-T peaks show the opposite trend. Structure refinement reveals that these new peaks belong to a FM phase with the same crystal structure as the

Figure 7.3: (a) Contour plot of the neutron diffraction patterns collected at WISH (detector bank 5 with $\langle 2\theta \rangle \approx 152.83°$) for the S1 sample. The intensity is on a logarithmic scale. (b) The (0.35 0 0) magnetic reflection of the SDW phase at different temperatures recorded at WISH (detector bank 1 with $\langle 2\theta \rangle \approx 27.08°$).
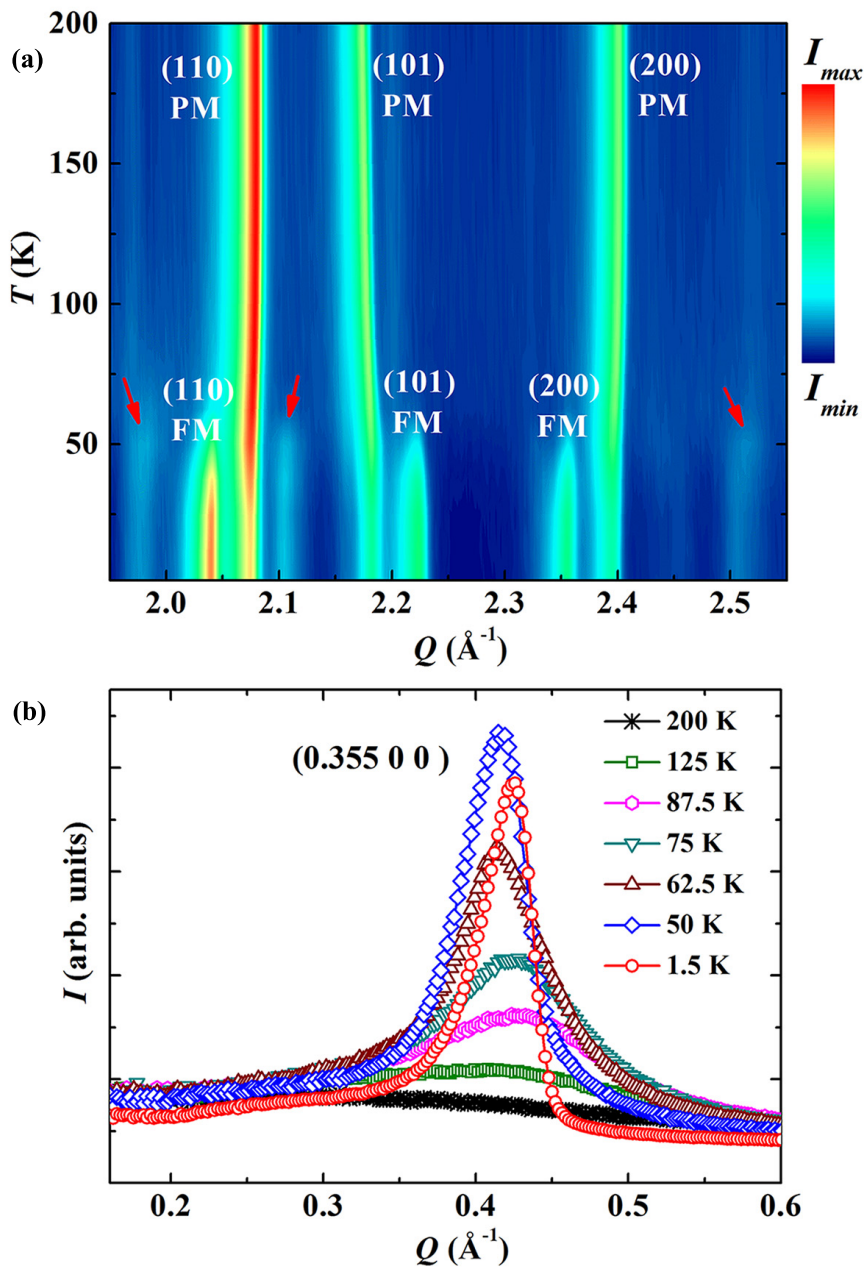
Table 7.1: Structural parameters of the as-prepared S1 sample at 1.5 K derived from neutron diffraction. Space group: $P\bar{6}2m$. Atomic positions: $3f(x_1,0,0)$; $3g(x_2,0,1/2)$; $2c(1/3,2/3,0)$ and $1b(0,0,1/2)$.

	Parameters	FM	SDW
	Fraction(%)	47.4(2)	52.6(2)
	a (Å)	6.1586(1)	6.0582(1)
	c (Å)	3.3304(1)	3.4421(1)
	V (Å^3)	109.394(4)	109.405(5)
$3f$	x_1	0.2601(3)	0.2581(3)
	$n(\text{Fe})/n(\text{Mn})$	0.165/0.085(1)	0.165/0.085(1)
	M (μ_B)	1.5(1)	0.8(2)
$3g$	x_2	0.5965(4)	0.5921(4)
	$n(\text{Mn})/n(\text{Fe})$	0.25/0	0.25/0
	M (μ_B)	2.8(1)	3.1(2)
$2c$	$n(\text{P})/n(\text{Si})$	0.117/0.050(4)	0.117/0.050(4)
$1b$	$n(\text{P})/n(\text{Si})$	0.050/0.033(4)	0.050/0.033(4)
	R_{Mag} (%)	2.68	8.35
	R_p (%)	4.26	
	wR_p (%)	4.90	
	χ^2	7.92	

PM phase, but with different lattice parameters. The Fe and Mn magnetic moments in the FM phase lie within the basal plane with magnitudes of 1.5 and 2.8 μ_B, respectively. The structural details of the FM phase derived from Rietveld refinement are summarized in Table 7.1. Additionally, some weak satellites around the main Bragg peaks appear at low temperature, as indicated by the arrows in Fig. 7.3(a), and a Bragg peak at $Q \approx 0.42$ Å^{-1} develops with the decrease of temperature (see Fig. 7.3(b)). These peaks cannot be indexed by any nuclear Bragg peaks. This strongly suggests the formation of another magnetic phase at low temperatures. An automatic indexing procedure using the k-search program in the Fullprof package [31] was performed to determine the propagation vector k of this magnetic phase. A propagation vector of k = (0.355(1), 0, 0) is derived, which indicates an incommensurate-magnetic structure (i.e., a helical spin configuration or a spin-density wave). The remaining intensities of the initial high-T peaks are from the nuclear structure of this incommensurate-magnetic phase.

In order to resolve the detailed magnetic structure of this incommensurate-magnetic phase, we performed a representation analysis [37, 38] using the *BasIreps* program [31]. Representation analysis yields two nonzero irreducible representations (IRs) for both Fe and Mn moments on the $3f$ and $3g$ sites, re-
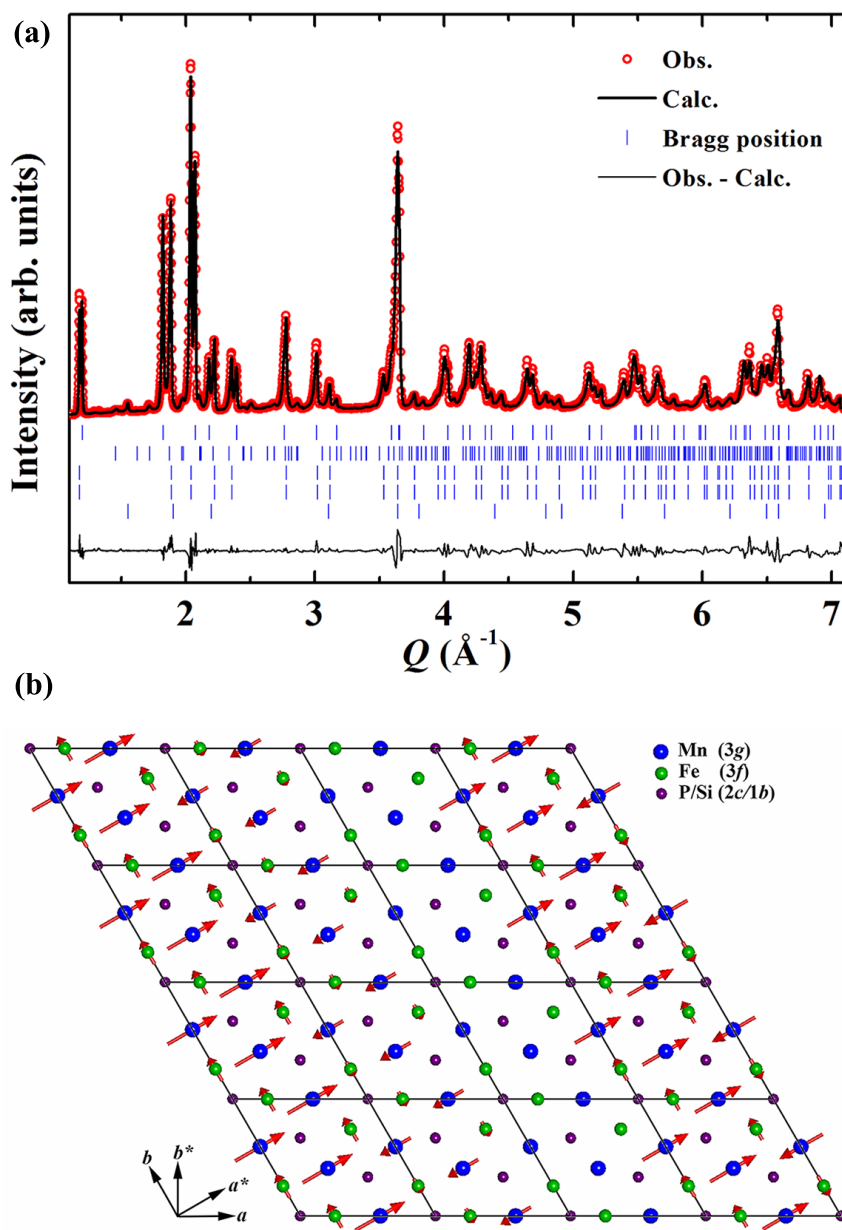
Figure 7.4: (a) Fitted powder neutron diffraction pattern for the S1 sample collected at 1.5 K at WISH (detector bank 3 with $\langle 2\theta \rangle \approx 90°$). Vertical lines indicate the peak positions (from top to bottom) for the nuclear structure of the SDW phase, magnetic structure of the SDW phase, nuclear structure of the FM phase, magnetic structure of the FM phase, and the impurity (Mn,Fe)$_3$Si phase, repectively. (b) Schematic representation (4×4) of magnetic configuration in the basal (ab) plane for the SDW phase. $\boldsymbol{a}^*$ and $\boldsymbol{b}^*$ are the primitive vectors of the reciprocal lattice. The propagation vector $\boldsymbol{k}$ is along $\boldsymbol{a}^*$. The Mn moment is aligned parallel to $\boldsymbol{k}$ and the Fe moment is perpendicular to $\boldsymbol{k}$.

spectively. One IR corresponds to both Fe and Mn moments along the c axis, and the other corresponds to both moments within the *ab* plane. A helical spin configuration with k = (0.355, 0, 0) is not allowed by the IRs. As a result, the incommensurate-magnetic phase can be described by a sinusoidal spin-density wave (SDW) with k = (0.355, 0, 0). We fitted the diffraction patterns using different magnetic configurations (see *Appendix*). The magnetic structure with the Mn and Fe moments parallel and perpendicular to the k, respectively, gives the best fit (see Fig. 7.4(a)) with a magnetic R-factor of 8.4%. A schematic representation of this magnetic structure is presented in Fig. 7.4(b). The structure details of the SDW phase derived from the refinement are summarized in Table 7.1. At 1.5 K, the S1 sample consists of FM and SDW phases with weight fractions of about 47.4% and 52.6%, respectively. The FM phase has larger and smaller dimensions in the basal plane and along the c axis, respectively, in comparison with the SDW phase. The Fe moment in the FM phase is almost twice as large as in the SDW phase, while the Mn moment is almost the same in both phases.

In order to explore the phase-transition in detail for the S1 sample, the Bragg peak at $Q \approx 0.42$ Å^{-1} (see Fig. 7.3(b)) was further analyzed, which is indexed to be the (0.35 0 0) magnetic reflection of the SDW phase. Above 60 K, the Bragg peak transforms into diffuse scattering, suggesting the presence of short-range magnetic correlations. The thermal evolution of the full-width-at-half-maximum (ΔQ) of the (0.35 0 0) peak is presented in Fig. 7.5(a). The correlation length $\xi = 2\pi/\Delta Q$ is estimated to be 30 Å at 200 K, and increases with decreasing temperature to about 180 Å in the magnetically ordered state (see Fig. 7.5(a)). The presence of short-range magnetic ordering above 60 K is also suggested by the bulk susceptibility (see Fig. 7.5(b)), where the inverse susceptibility shows a strong deviation from the Curie-Weiss behavior below 300 K.

The integrated intensity of the (0.35 0 0) peak as a function of temperature is presented in Fig. 7.5(c). The integrated intensity rises with decreasing temperature from 200 to 50 K, which is attributed to the weakening of the magnetic fluctuations. The reduction in the integrated intensity below 50 K is due to the decreasing fraction of the SDW phase caused by the SDW to FM phase transition. Structure refinement reveals that there is no detectable FM phase above 62.5 K, and f_{FM} increases from about 10% at 50 K to around 47% at 1.5 K upon cooling. In order to exclude the influence of the SDW-FM transition on the integrated intensity of the (0.35 0 0) peak, the integrated intensity is normalized by the phase fraction of the SDW phase (see Fig. 7.5(c)). Since the normalized intensity is proportional to M^2, a critical temperature T_{SDW} of about 62.5 K for the PM-SDW transition is derived by taking the derivative of the normalized intensity with respect to temperature.

The lattice parameters at different temperatures are shown in Fig. 7.6. The

7
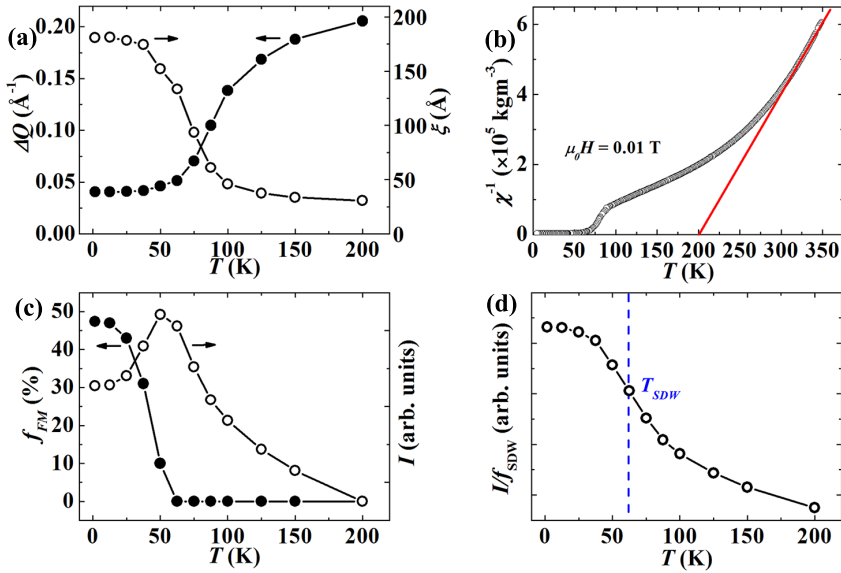
Figure 7.5: (a) Peak width of the (0.35 0 0) magnetic reflection. (b) Temperature-dependent inverse susceptibility. (c) Weight fraction of the FM phase and integrated intensity of the (0.35 0 0) magnetic reflection at different temperatures. (d) Temperature dependence of the normalized intensity of the (0.35 0 0) magnetic reflection.

anomalous thermal expansion of the lattice parameters between 200 and 62.5 K is associated with the development of short-range magnetic correlations. The lattice parameters show a continuous change around the PM-SDW transition temperature ($T_{SDW} \approx 62.5$ K), implying a second-order phase transition. The jump in lattice parameters, which accompanies the SDW-FM transition ($T_C \approx 50$ K), characterizes the first-order nature of the transition and the strong magnetoelastic coupling.

The changes in lattice parameter correspond to variations in the interatomic distances, which are coupled with the magnetic exchange interactions. As shown in Fig. 7.7, the intralayer atomic distances gradually increase with decreasing temperature until the SDW-FM transition temperature is reached, where a jump in the interatomic distances occurs. The interlayer atomic distances show a similar feature, although the change is in the opposite direction. A significant expansion in the intralayer bonds after the SDW-FM transition leads to a stronger localization of Fe and Mn $3d$ electrons and less chemical bonding with neighboring atoms in the FM phase. Also, the smaller distance between Mn and Fe atoms in the FM phase enhances the magnetic exchange interaction. As a result, a ferromagnetic coupling is more favorable at low temperatures.
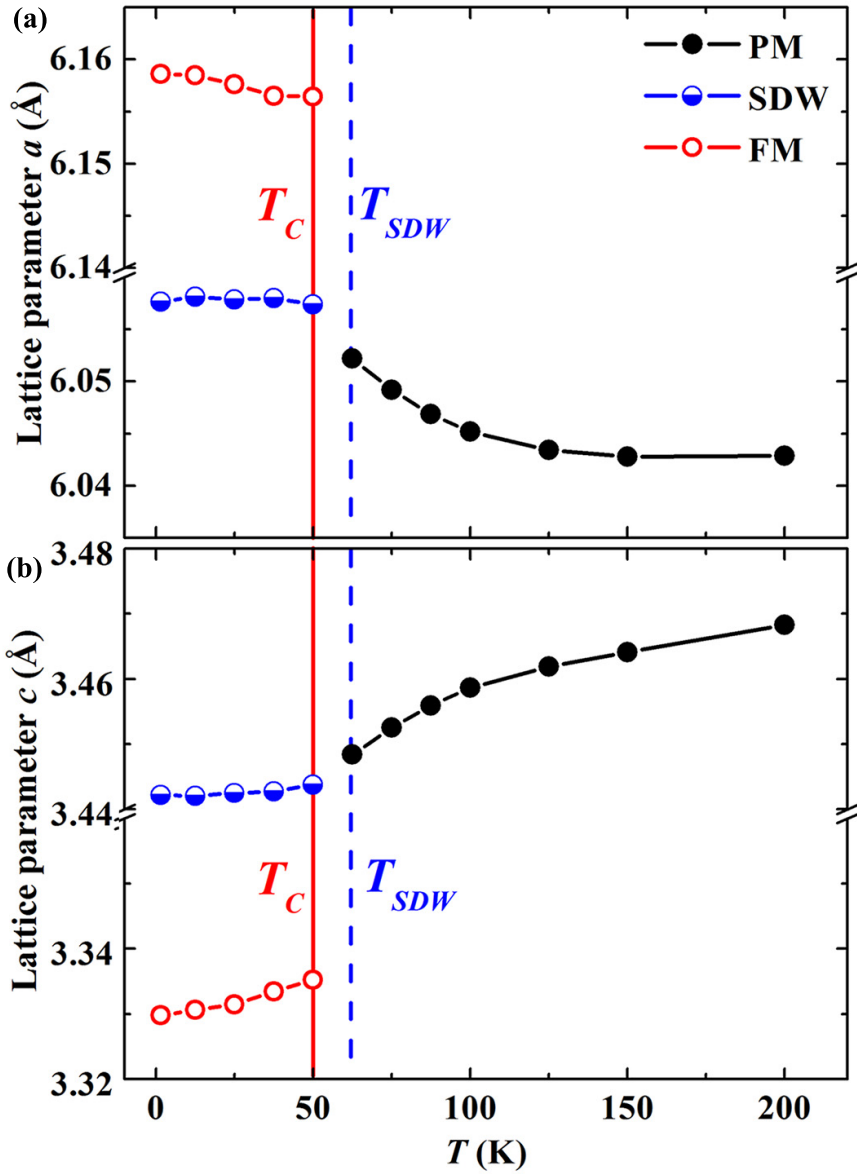
Figure 7.6: Lattice parameters as a function of temperature derived from neutron diffraction for the S1 sample.
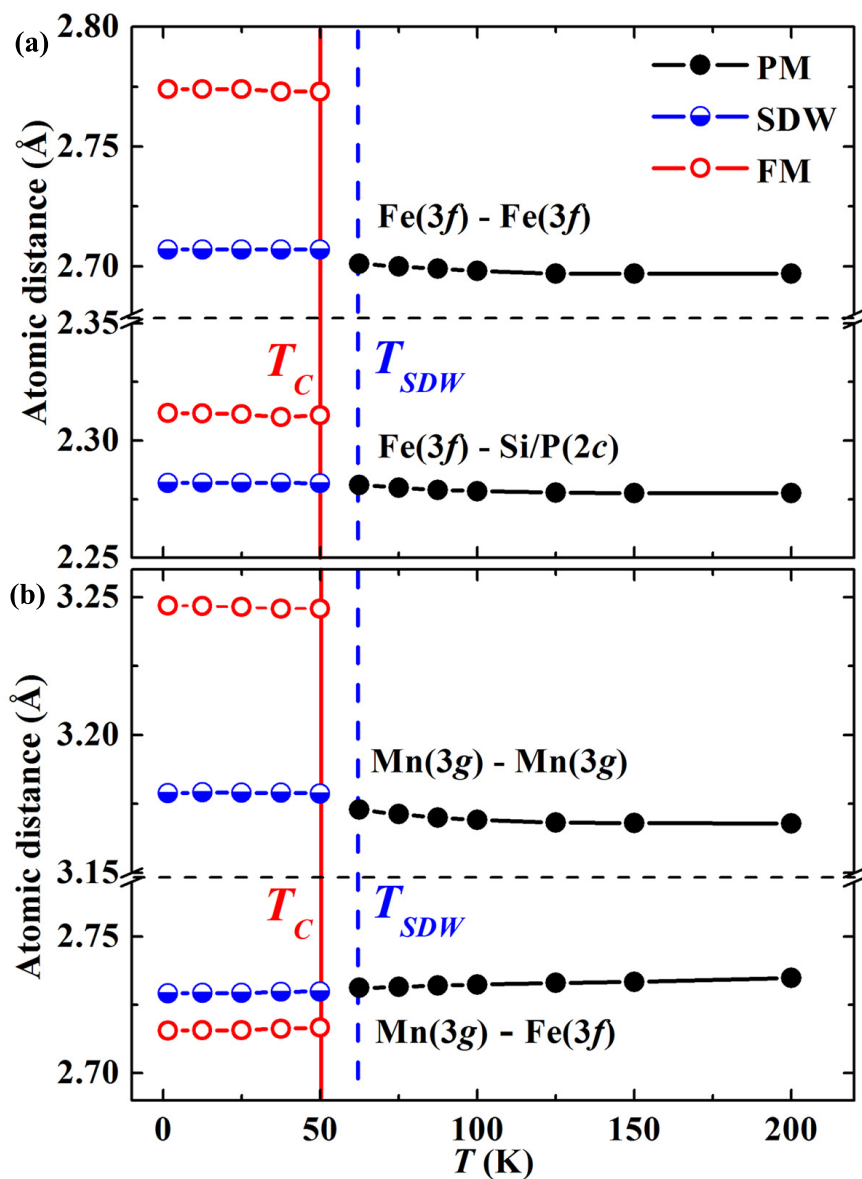
Figure 7.7: Thermal-evolution of interatomic distances extracted from neutron diffraction for the S1 sample.
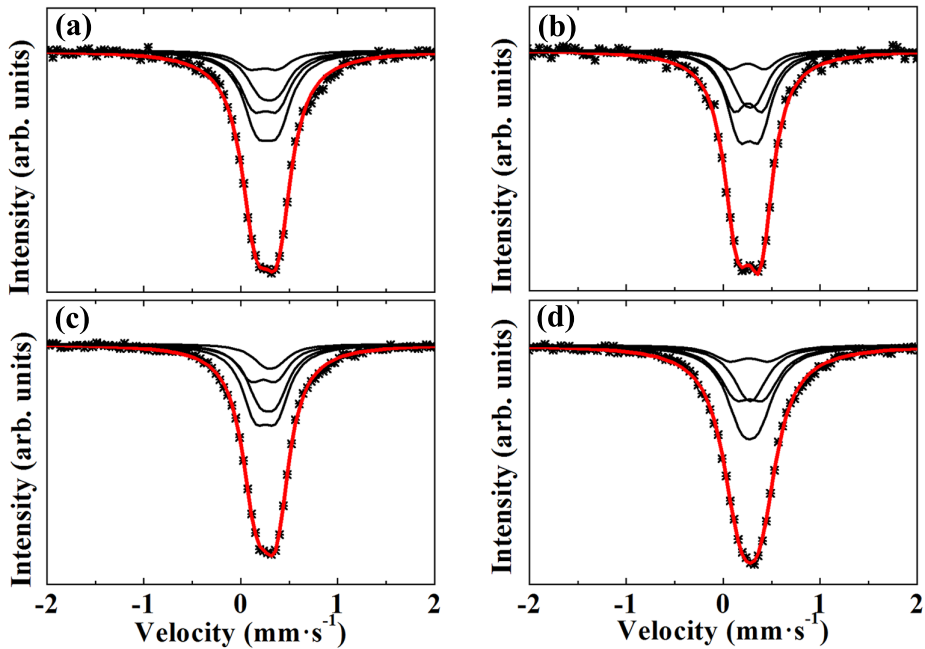
Figure 7.8: Mössbauer spectra collected at 300 K for the as-prepared S0 (a), S1 (b), S2 (c), and S3 (d) samples. The black and red solid lines are individual binomial PM-components and their sum, respectively.

7.5. MÖSSBAUER MEASUREMENTS

THE magnetic ordering of the Fe atoms in the SDW and FM phases can be further investigated using ^{57}Fe Mössbauer spectroscopy. Mössbauer spectra of the as-prepared S0-S3 samples, measured at 300 K are presented in Fig. 7.8(a)-(d), respectively.

All spectra exhibit a paramagnetic feature. According to the neutron diffraction results (see Table 7.1), the P and Si atoms are randomly distributed in the tetrahedral environment around Fe atoms in the studied samples. As a result, there are five different nearest-neighbor Fe configurations, depending on the

7

Table 7.2: Hyperfine parameters at 300 K for the as-prepared S0-S3 samples.

Sample	$\langle\delta\rangle$ (mm/s)	$\langle\Delta\rangle$ (mm/s)	Γ (mm/s)
S0	0.27(1)	0.22(1)	0.34(1)
S1	0.26(1)	0.24(1)	0.30(1)
S2	0.26(1)	0.21(1)	0.32(1)
S3	0.27(1)	0.22(1)	0.39(1)
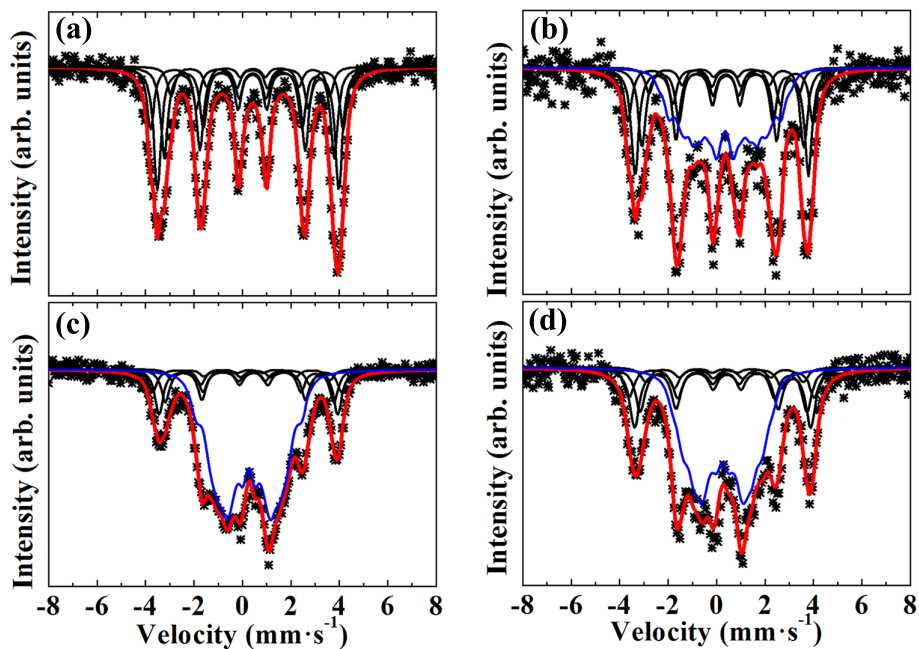
Figure 7.9: Mössbauer spectra obtained at 4.2 K for the as-prepared S0 (a), S1 (b), S2 (c), and S3 (d) samples. The black, blue and red lines are individual binomial FM-components, the SDW component and their sum, respectively.

number (from 0 to 4) of Si atoms in the tetrahedral environment. Their contributions to the Mössbauer spectrum can be described by a binomial distribution model, which has been successfully used for Mössbauer analysis in $(Mn,Fe)_2(P,Si)$-type compounds[39, 40]. Hyperfine parameters obtained from the fitting are presented in Table 7.2. The average isomer shift $\langle\delta\rangle$, average quadrupole splitting $\langle\Delta\rangle$ and line width Γ are in good agreement with previous reports in $(Mn,Fe)_2(P,Si)$-type compounds[39–41].

Fig. 7.9(a) shows the Mössbauer spectrum measured at 4.2 K for the S0 sample after zero-field cooling. The observed sextet with broad spectral lines suggests a strong magnetic ordering with a distribution in hyperfine fields around the Fe nucleus, which can be fitted with a binomial distribution model [40]. In contrast, the 4.2 K Mössbauer spectra of the S1-S3 samples display a complicated shape, as shown in Fig. 7.9(b-d). As revealed by the neutron diffraction results, the S1 sample is a mixture of FM and SDW phases below 50 K. As a result, the 4.2 K Mössbauer spectra of the S1-S3 samples can be decomposed into FM and incommensurate magnetic components. The FM component was fitted with the binomial distribution model [40], and the incommensurate magnetic

component was fitted with a field-distribution model that takes into account the sinusoidally modulated Fe moment. For the incommensurate-magnetic component, the hyperfine field H_{SDW} experienced by an Fe nucleus can be described as

$$H_{SDW} = H_{SDW}^{m} sin\theta \tag{7.1}$$

where H_{SDW}^{m} is the magnitude of the hyperfine field, which is modulated by a sine function. The sign of the hyperfine field has no influence on the spectrum. As a result, the incommensurate-magnetic contribution can be obtained by integration over $0 \leqslant \theta \leqslant \pi/2$ for Eq. 7.1. The above model gives a reasonable fit to the 4.2 K Mössbauer spectra for the S1-S3 samples.

The derived hyperfine parameters are given in Table 7.3. The Mössbauer experiments suggest that the S0 sample is a pure FM phase at 4.2 K. For the S1 sample, the f_{FM} derived from Mössbauer spectrum is about 61%, which is close to the value of 47.4% derived from neutron diffraction measurements (Table 7.1). A smaller fraction of FM phase is present at 4.2 K in the S2 and S3 samples than in the S1 sample, which is consistent with the magnetization results (see Figs. 7.1 and 7.2).

For the S1 sample, the magnitude of the hyperfine fields is about 21.8 and 17.7 T for the FM and SDW phases at 4.2 K, respectively. Using a proportionality factor of 14.2 T/μ_B, as proposed by Eriksson and Svane [42], the Fe moments in the FM and SDW phases are estimated to be 1.5 and 1.2 μ_B, which is in reasonable agreement with the neutron diffraction results (see Table 7.1). Consequently, the SDW to FM transition is accompanied by a significant increase in the Fe moment and a slight change in the Mn moment, which characterizes the unique mixed magnetism in the $(Mn,Fe)_2(P,Si)$-type compounds. The Fe atoms on the $3f$ site show weak magnetism. The development of the Fe moment is in strong competition with the formation of chemical bonds, which in turn depends on the interatomic distances between Fe and its neighbors (shown in Fig. 7.7). The Mn atoms on the $3g$ site show strong magnetism, the Mn moment is less influenced by the interatomic distances.

7

Table 7.3: Hyperfine parameters at 4.2 K for the as-prepared S0-S3 samples.

Sample	$\langle \delta \rangle$ (mm/s)	$\langle \Delta \rangle$ (mm/s)	Γ (mm/s)	$\mu_0 H$ (T)	Phase	Fraction (%)
S0	0.33(1)	-0.17(1)	0.36(1)	22.8(1)	FM	100
S1	0.31(1)	-0.17(1)	0.37(1)	21.8(1)	FM	61(3)
	0.35(1)	-	0.37(1)	17.7(5)	SDW	39(3)
S2	0.35(1)	-0.17(1)	0.42(1)	22.7(1)	FM	35(3)
	0.36(1)	-	0.42(1)	18.8(5)	SDW	65(3)
S3	0.34(1)	-0.16(1)	0.49(1)	22.2(1)	FM	41(3)
	0.35(1)	-	0.50(1)	18.4(5)	SDW	59(3)

7.6. IN-FIELD X-RAY DIFFRACTION

X-ray powder diffraction was measured at 300 and 10 K for the as-prepared S0, S1 and S3 samples. Structure refinement confirms the hexagonal Fe_2P-type structure ($P\bar{6}2m$) at the two temperatures for all the 3 samples. When the as-prepared S0 sample is cooled down from 300 to 10 K, a significant shift in the (210) Bragg peak appears in the XRD pattern (see Fig. 7.10(a)), indicating a strong magnetoelastic coupling. In the X-ray diffraction pattern, there is no detectable phase coexistence in the S0 sample at 10 K. This is in agreement with the Mössbauer results shown in Table 7.3. XRD patterns were then collected for different magnetic fields at a constant temperature of 10 K (see Fig. 7.10(b)). The applied magnetic field has little influence on the XRD patterns.

The XRD pattern of the S1 sample collected at 10 K after zero-field cooling is in strong contrast to that of the S0 sample. Two Bragg peaks appear at 2θ values of 45.0° and 45.8°, respectively. Structure refinement reveals that these two peaks belong to the (210) Bragg peak of two phases having the same crystal structure but with different lattice parameters. For increasing magnetic fields, the peak at $2\theta \approx 45.0°$ grows at the expense of the peak at $\approx 45.8°$ (Fig. 7.10(b)), which clearly demonstrates the field-induced metamagnetic SDW-FM transition. At 5 T, the peak at $2\theta \approx 45.8°$ has almost disappeared. After the XRD measurement in 5 T, the magnetic field was removed and an XRD pattern was collected in 0 T. No change in the XRD pattern is observed after the removal of the magnetic field, nor during the subsequent field-increasing process. This is evidence of the irreversibility of the SDW to FM transition, which is also observed in our magnetization measurements (see Fig. 7.1(d)).

The coexistence of the SDW and FM phases is also observed in the XRD pattern (Fig. 7.10(d)) of the S3 sample measured at 10 K after zero-field cooling. The field-induced SDW-FM transition is manifested by the increasing intensity of the FM (210) peak at $\approx 45.1°$ with increasing magnetic field. The SDW-FM transition is still not complete at 5 T, as indicated by the remaining peak at $2\theta \approx 46.3°$. There is no signature of a recovery of the SDW phase during the subsequent field cycle at 10 K (see Fig. 7.10(e)).
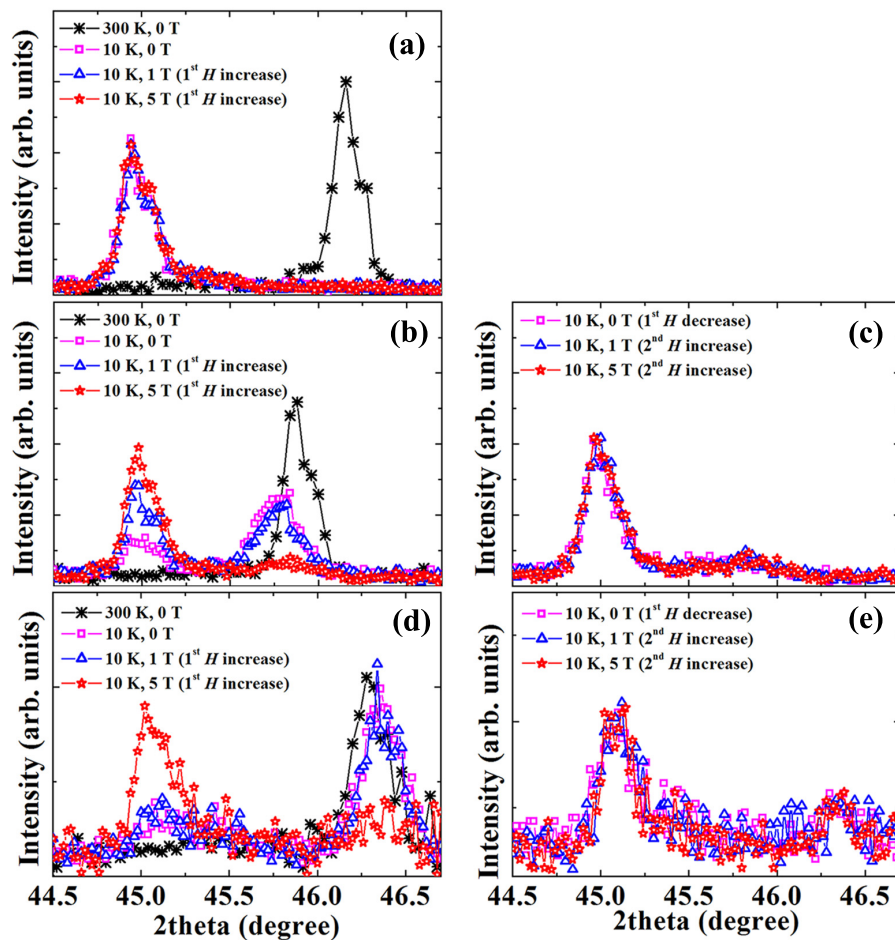
7

Figure 7.10: XRD patterns measured at 300 K and 10 K in different magnetic field for the as-prepared S0 (a), S1 (b-c), and S3 (d-e) samples.

Table 7.4: Structural parameters for the S0, S1 and S3 samples in different magnetic states obtained from X-ray diffraction.

Parameter	Phase	S0	S1	S3
a (Å)	PM	6.013(1)	6.055(1)	6.014(1)
	SDW	-	6.058(1)	6.009(2)
	FM	6.157(1)	6.158(1)	6.142(2)
c (Å)	PM	3.478(1)	3.474(1)	3.484(1)
	SDW	-	3.442(1)	3.474(2)
	FM	3.299(1)	3.331(1)	3.305(2)
c/a	PM	0.578(1)	0.574(1)	0.579(1)
	SDW	-	0.568(1)	0.578(2)
	FM	0.536(1)	0.541(1)	0.538(2)

The structural parameters derived from Rietveld refinement for the S0, S1 and S3 samples are summarized in Table 7.4. The magnetic transition is strongly coupled to variations in the lattice parameters. The FM configuration is in competition with an incommensurate magnetic configuration in the $(Mn,Fe)_2(P,Si)$ compounds, and the relative stability of the two configurations strongly depends on the c/a ratio [28]. The stability of the incommensurate magnetic configuration is enhanced with the increase in c/a ratio [28]. As a result, a metastable incommensurate magnetic configuration forms in the S1 and S3 samples with large c/a ratios at low temperature. Additionally, the S1 and S3 samples have a low T_C, as indicated by the magnetization results shown in Figs. 7.1 and 7.2. Due to the small thermal energy at low temperatures, the phase transition from the metastable incommensurate phase to stable FM phase may be kinetically arrested. As a consequence, the metastable incommensurate SDW phase coexists with the stable FM phase at low temperatures in the S1 and S3 samples. An external magnetic field promotes the FM phase and therefore drives the SDW to FM transition.

7.7. METASTABILITY OF THE SDW PHASE

THE S1 sample was used for further studies on the metastability of the SDW phase, since its SDW-FM transition can be triggered by field and completed below 5 T at low temperatures (see Fig. 7.1(d)). Fig. 7.11(a) compares isothermal M-H curves measured at 5 K after cooling in different magnetic fields. To avoid any thermal- (or field-) history effects, each M-H measurement was performed on a different piece of the sample from the same batch.
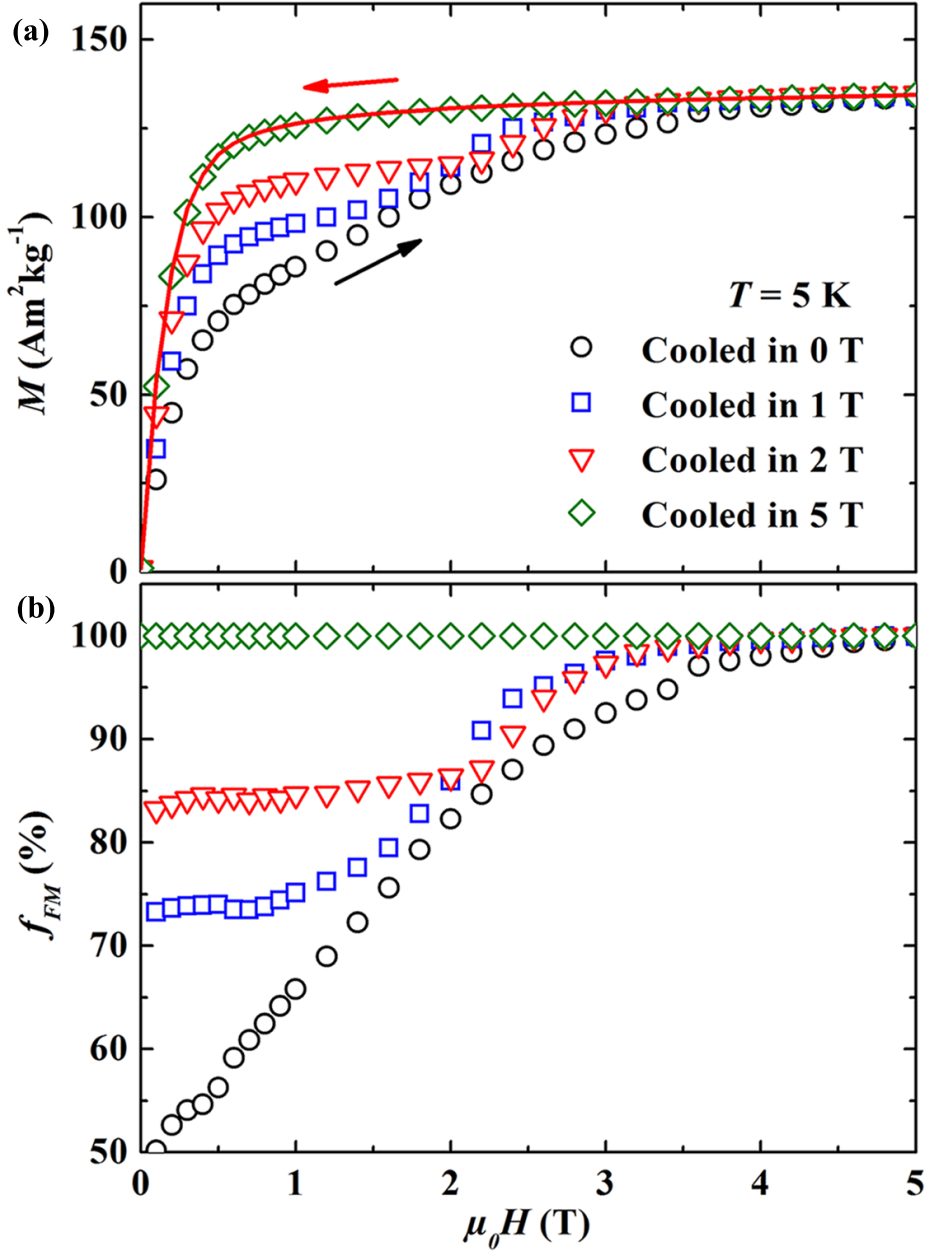
7

Figure 7.11: (a) Isothermal M-H curves for the as-prepared S1 sample cooled in different magnetic fields. Open symbols indicate the magnetization process, and the solid line shows the demagnetization process. The demagnetization curve is the same for all four conditions. (b) Derived f_{FM}-H at 5 K after cooling in different magnetic fields.

7

A field-induced SDW-FM transition is present in all the samples cooled in a magnetic field below 5 T. No metamagnetic transition appears in the subsequent decrease and increase in magnetic field, indicating the formation of a stable FM phase. Since the SDW phase has no net magnetization, the measured magnetization is proportional to the fraction of FM phase (f_{FM}). If we assume that the sample cooled in 5 T is a pure FM phase (i.e., f_{FM} = 100%), then the f_{FM}-H curve at 5 K for samples cooled in different fields can be derived using $M(H)/M_{5T}(H)$. Fig. 7.11(b) shows that the sample cooled in zero magnetic field contains about 50% FM phase at 5 K, which is in good agreement with the neutron diffraction and Mössbauer results (see Table 7.1 and 7.3). The FM fraction increases rapidly with increasing H, reaching 100% at about 4 T. For the samples cooled in 1 and 2 T, the f_{FM} remains nearly constant when the applied magnetic field is lower than the cooling field, as illustrated by the initial plateau in the f_{FM}-H curves. When the applied magnetic field exceeds the cooling field, the SDW-FM transition is triggered and completed at around 4 T. It should be noted that there is a clear difference in the f_{FM} at $\mu_0 H = 1$ T between the samples cooled in 0 T and 1 T (see Fig. 7.11(b)). This difference is due to the kinetic nature of the SDW-FM transition.

The "CHUF" measurement protocol, i.e., cooling and warming in unequal fields, as proposed by Banerjee et al [23, 36], provides a method to identify the kinetic-arrest induced phase coexistence and its metastability. After cooling from 300 to 5 K in 0, 1 and 5 T, respectively, a magnetic field of 1 T was applied and M-T measurements were performed on warming. The M-T curve of the sample cooled in zero field shows an initial increase below 20 K and then merges with the M-T curve of the sample cooled in 1 T (see Fig. 7.12(a)). The initial increase of the magnetization with increasing temperature is associated with the de-arrest of the SDW-FM transition and the resulting increase of the FM fraction. The SDW phase is highly metastable and the increasing T and H converts it to the stable FM phase. A high magnetization is observed for the sample cooled in 5 T due to the absence of the SDW phase, as suggested in Fig. 7.11(b).

Magnetization relaxation measurements at various temperatures provide further evidence for the metastability of the SDW phase. The as-prepared S1 sample was cooled down to various measurement temperatures in zero magnetic field. After that, a magnetic field of 1 T was applied and the magnetization was measured immediately after the field stabilization. As depicted in Fig. 7.12(b), a notable relaxation in the M highlights the metastability of the SDW phase. With the decrease of temperature, the relaxation becomes less pronounced. The Kohlrausch-Williams-Watt (KWW) stretched exponential function [43, 44] $\Phi(t) \propto exp[-(t/\tau)^\beta]$ has been widely used to describe the magnetic relaxation behavior in kinetically-arrested FOMT systems [13, 15, 16], where τ is the characteristic

relaxation time and β is a shape parameter. The relaxation data below 20 K can be fit well using the KWW function with $\beta = 0.18$, while noticeable deviations appear above 20 K. The τ increases markedly with decreasing temperature due to the reduction in thermal fluctuation, as shown in the inset of Fig. 7.12(b). An activation energy of $\Delta E = 0.24(3)$ kJ/mol can be derived from the $\ln(\tau)$-T curve based on the Arrhenius equation.
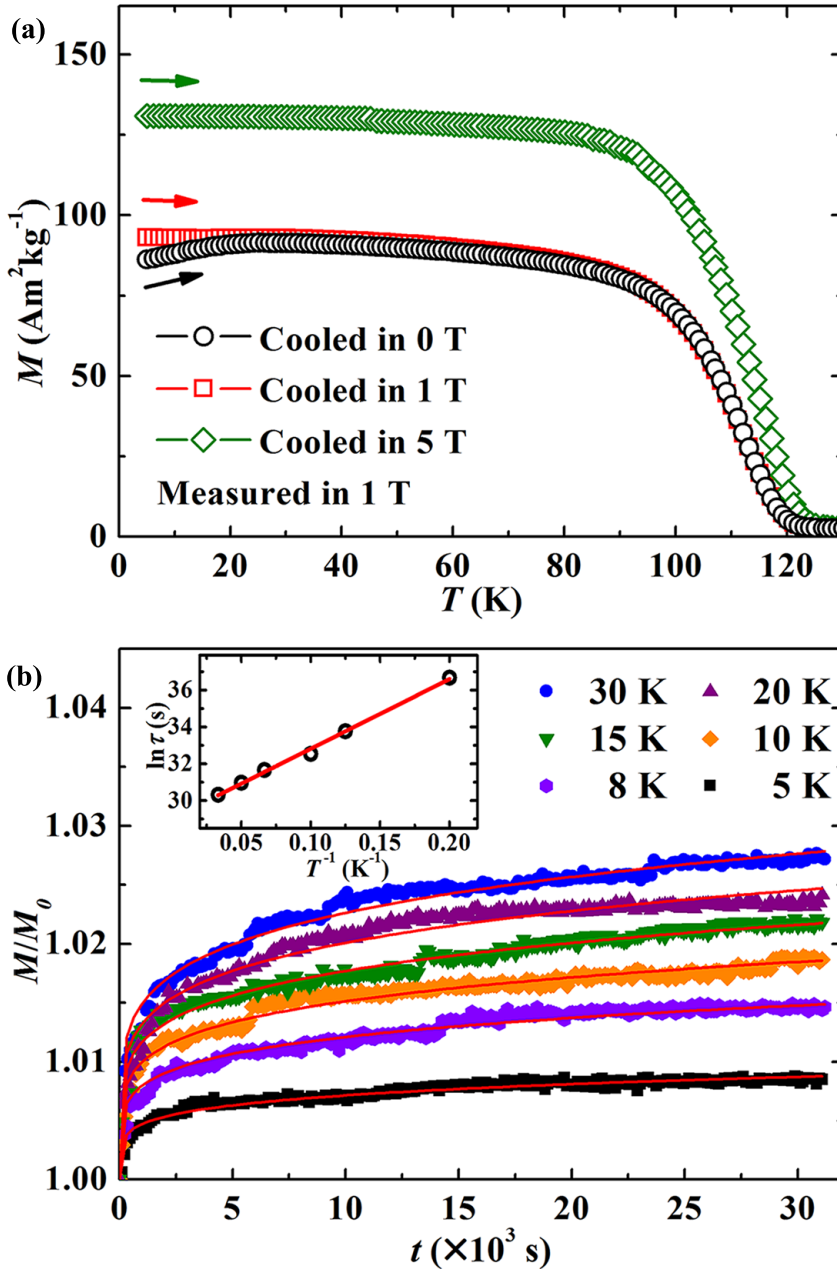
Figure 7.12: (a) Temperature-dependent magnetization of the S1 sample measured during warming after being cooled in different magnetic fields. (b) Magnetization versus time measured at 5 K after zero-field cooling. The temperature-dependence of the characteristic relaxation time is shown in the inset.

7.8. CONCLUSIONS

IN contrast to the common PM-FM phase transition in $(Mn,Fe)_2(P,Si)$ compounds, a PM-SDW-FM transition is observed for some compositions. The PM-SDW transition is second-order and accompanied with continuous changes in the lattice parameters. The SDW-FM transition, first-order in nature, is strongly coupled to discontinuous variations in the lattice parameters. The SDW-FM transition can be kinetically arrested, leading to a coexistence of the FM phase and the untransformed SDW phase at low temperature. The untransformed SDW phase is metastable at low temperatures, and can be converted to the stable FM phase by magnetic field. The formation of the SDW phase originates from the lower stability of FM phase at large c/a ratios. The SDW-FM transition is accompanied by a significant increase in the Fe moment and a slight change in the Mn moment. This study sheds new light on the strong magnetoelastic coupling and mixed magnetism in the $(Mn,Fe)_2(P,Si)$ system.

REFERENCES

[1] V. K. Pecharsky and K. A. Gschneidner, Jr, *Giant magnetocaloric effect in $Gd_5(Si_2Ge_2)$,* Phys. Rev. Lett. **78**, 4494 (1997).

[2] O. Tegus, E. Brück, K. H. J. Buschow, and F. R. de Boer, *Transition-metal-based magnetic regrigerants for room-temperature applications,* Nature **415**, 150 (2002).

[3] A. Fujita, S. Fujieda, Y. Hasegawa, and K. Fukamichi, *Itinerant-electron metamagnetic transition and large magnetocaloric effects in $La(Fe_xSi_{1-x})_{13}$ compounds and their hydrides,* Phys. Rev. B **67**, 104416 (2003).

[4] R. von Helmolt, J. Wecker, B. Holzapfel, L. Schultz, and K. Samwer, *Giant negative magnetoresistance in perovskitelike $La_{2/3}Ba_{1/3}MnO_x$ ferromagnetic films,* Phys. Rev. Lett. **71**, 2331 (1993).

[5] S. Jin, T. H. Tiefel, M. McCormack, R. A. Fastnacht, R. Ramesh, and L. H. Chen, *Thousandfold change in resistivity in magnetoresistive La-Ca-Mn-O films,* Science **264**, 413 (1994).

[6] K. Ullakko, J. K. Huang, C. Kantner, R. C. O'Handley, and V. V. Kokorin, *Large magnetic-field-induced strains in Ni_2MnGa single crystals,* Appl. Phys. Lett. **69**, 1966 (1996).

[7] S. J. Park, H. W. Yeom, J. R. Ahn, and I. W. Lyo, *Atomic-scale phase coexistence and fluctuation at the quasi-one-dimensional metal-insulator transition,* Phys. Rev. Lett. **95**, 126102 (2005).

7

[8] S. B. Roy, G. K. Perkins, M. K. Chattopadhyay, A. K. Nigam, K. J. S. Sokhey, P. Chaddah, A. D. Caplin, and L. F. Cohen, *First order magnetic transition in doped CeFe$_2$ alloys: phase coexistence and metastability,* Phys. Rev. Lett. **92**, 147203 (2004).

[9] D. D. Sarma, D. Topwal, U. Manju, S. R. Krishnakumar, M. Bertolo, S. La Rosa, G. Cautero, T. Y. Koo, P. A. Sharma, S. W. Cheong, and A. Fujimori, *Direct observation of large electronic domains with memory effect in doped manganites,* Phys. Rev. Lett. **93**, 097202 (2004).

[10] A. Soibel, E. Zeldov, M. Rappaport, Y. Myasoedov, T. Tamegai, S. Ooi, M. Konczykowski, and V. B. Geshkenbein, *Imaging the vortex-lattice melting process in the presence of disorder,* Nature **406**, 6 (2000).

[11] M. E. Brown, A. H. Bouchez, and C. A. Griffith, *Direct detection of variable tropospheric clouds near titan's south pole,* Nature **420**, 795 (2002).

[12] W. Wu, C. Israel, N. Hur, S. Park, S. W. Cheong, and A. de Lozanne, *Magnetic imaging of a supercooling glass transition in a weakly disordered ferromagnet,* Nature Mater. **5**, 881 (2006).

[13] M. K. Chattopadhyay, S. B. Roy, and P. Chaddah, *Kinetic arrest of the first-order ferromagnetic-to-antiferromagnetic transition in Ce(Fe$_{0.96}$Ru$_{0.04}$)$_2$: formation of a magnetic glass,* Phys. Rev. B **72**, 180401 (2005).

[14] M. A. Manekar, S. Chaudhary, M. K. Chattopadhyay, K. J. Singh, S. B. Roy, and P. Chaddah, *First-order transition from antiferromagnetism to ferromagnetism in Ce(Fe$_{0.96}$Al$_{0.04}$)$_2$,* Phys. Rev. B **64**, 104416 (2001).

[15] S. B. Roy, M. K. Chattopadhyay, P. Chaddah, J. D. Moore, G. K. Perkins, L. F. Cohen, K. A. Gschneidner, and V. K. Pecharsky, *Evidence of a magnetic glass state in the magnetocaloric material Gd$_5$Ge$_4$,* Phys. Rev. B **74**, 012403 (2006).

[16] V. K. Sharma, M. K. Chattopadhyay, and S. B. Roy, *Kinetic arrest of the first order austenite to martensite phase transition in Ni$_{50}$Mn$_{34}$In$_{16}$: dc magnetization studies,* Phys. Rev. B **76**, 140401 (2007).

[17] R. Y. Umetsu, K. Ito, W. Ito, K. Koyama, T. Kanomata, K. Ishida, and R. Kainuma, *Kinetic arrest behavior in martensitic transformation of NiCoMnSn metamagnetic shape memory alloy,* J. Alloys Compd. **509**, 1389 (2011).

7

[18] W. Ito, K. Ito, R. Y. Umetsu, R. Kainuma, K. Koyama, K. Watanabe, A. Fujita, K. Oikawa, K. Ishida, and T. Kanomata, *Kinetic arrest of martensitic transformation in the NiCoMnIn metamagnetic shape memory alloy,* Appl. Phys. Lett. **92**, 021908 (2008).

[19] P. Kushwaha, A. Lakhani, R. Rawat, and P. Chaddah, *Low-temperature study of field-induced antiferromagnetic-ferromagnetic transition in pd-doped FeRh,* Phys. Rev. B **80**, 174413 (2009).

[20] K. Sengupta and E. V. Sampathkumaran, *Field-induced first-order magnetic phase transition in an intermetallic compound Nd_7Rh_3: evidence for kinetic hindrance, phase coexistence, and percolative electrical conduction,* Phys. Rev. B **73**, 020406 (2006).

[21] K. Mukherjee, S. D. Das, N. Mohapatra, K. K. Iyer, and E. V. Sampathkumaran, *Anomalous butterfly-shaped magnetoresistance loops in the alloy Tb_4LuSi_3,* Phys. Rev. B **81**, 184434 (2010).

[22] H. Kuwahara, Y. Tomioka, A. Asamitsu, Y. Moritomo, and Y. Tokura, *A first-order phase transition induced by a magnetic field,* Science **270**, 961 (1995).

[23] A. Banerjee, A. K. Pramanik, K. Kumar, and P. Chaddah, *Coexisting tunable fractions of glassy and equilibrium long-range-order phases in manganites,* J. Phys.: Condens. Matter **18**, L605 (2006).

[24] K. Kumar, A. K. Pramanik, A. Banerjee, P. Chaddah, S. B. Roy, S. Park, C. L. Zhang, and S. W. Cheong, *Relating supercooling and glass-like arrest of kinetics for phase separated systems: doped $CeFe_2$ and (La,Pr,Ca)MnO_3,* Phys. Rev. B **73**, 184435 (2006).

[25] R. Rawat, K. Mukherjee, K. Kumar, A. Banerjee, and P. Chaddah, *Anomalous first-order transition in $Nd_{0.5}Sr_{0.5}MnO_3$: an interplay between kinetic arrest and thermodynamic transitions,* J. Phys.: Condens. Matter **19**, 256211 (2007).

[26] A. Shahee, D. Kumar, C. Shekhar, and N. P. Lalla, *Kinetic arrest of first-order Rc to Pbnm phase-transition in supercooled $La_xMnO_{3+\delta}$ (x=1 and 0.9),* J. Phys.: Condens. Matter **24**, 225405 (2012).

[27] V. Höglin, M. Hudl, L. Caron, P. Beran, M. H. Sorby, P. Nordblad, Y. Andersson, and M. Sahlberg, *Detailed study of the magnetic ordering in $FeMnP_{0.75}Si_{0.25}$,* J. Solid State Chem. **221**, 240 (2015).

[28] E. K. Delczeg-Czirjak, M. Pereiro, L. Bergqvist, Y. O. Kvashnin, I. Di Marco, G. Li, L. Vitos, and O. Eriksson, *Origin of the magnetostructural coupling in FeMnP$_{0.75}$Si$_{0.25}$,* Phys. Rev. B **90**, 214436 (2014).

[29] G. Li, W. Li, S. Schönecker, X. Li, E. K. Delczeg-Czirjak, Y. O. Kvashnin, O. Eriksson, B. Johansson, and L. Vitos, *Kinetic arrest induced antiferromagnetic order in hexagonal FeMnP$_{0.75}$Si$_{0.25}$ alloy,* Appl. Phys. Lett. **105**, 262405 (2014).

[30] K. Watanabe, Y. Watanabe, S. Awaji, M. Fujiwara, N. Kobayashi, and T. Hasebe, *X-ray diffraction investigation in high fields at low temperature for Nd$_{0.5}$Sr$_{0.5}$MnO$_3$,* in *Advances in Cryogenic Engineering Materials,* Advances in Cryogenic Engineering, Vol. 44, edited by U. B. Balachandran, D. G. Gubser, K. T. Hartwig, R. P. Reed, W. H. Warnes, and V. A. Bardos (Springer US, 1998) Chap. 98, pp. 747–752.

[31] J. Rodríguez-Carvajal, *Recent advances in magnetic structure determination by neutron powder diffraction,* Physica B **192**, 55 (1993).

[32] Z. Klencsár, *Mössbauer spectrum analysis by evolution algorithm,* Nucl. Instr. and Meth. in Phys. Res. B **129**, 527 (1997).

[33] X. F. Miao, L. Caron, Z. Gercsi, A. Daoud-Aladine, N. H. van Dijk, and E. Brück, *Thermal-history dependent magnetoelastic transition in (Mn,Fe)$_2$(P,Si),* Appl. Phys. Lett. **107**, 042403 (2015).

[34] F. Guillou, G. Porcari, H. Yibole, N. H. van Dijk, and E. Brück, *Taming the first-order transition in giant magnetocaloric materials,* Adv. Mater. **26**, 2671 (2014).

[35] N. H. Dung, L. Zhang, Z. Q. Ou, and E. Brück, *From first-order magneto-elastic to magneto-structural transition in (Mn,Fe)$_{1.95}$P$_{0.50}$Si$_{0.50}$ compounds,* Appl. Phys. Lett. **99**, 092511 (2011).

[36] A. Banerjee, K. Kumar, and P. Chaddah, *Conversion of a glassy antiferromagnetic-insulating phase to an equilibrium ferromagnetic-metallic phase by devitrification and recrystallization in al substituted Pr$_{0.5}$Ca$_{0.5}$MnO$_3$,* J. Phys.: Condens. Matter **21**, 026002 (2009).

[37] E. F. Bertaut, *Representation analysis of magnetic structures,* Acta Cryst. A **24**, 217 (1968).

[38] E. F. Bertaut, *On group theoretical techniques in magnetc structure analysis,* J. Magn. Magn. Mater. **24**, 267 (1981).

7

[39] B. Malaman, G. L. Caer, P. Delcroix, D. Fruchart, M. Bacmann, and R. Fruchart, *Magneto-elastic transition and magnetic coupling: a Fe Mössbauer spectroscopy study of the MnFeP$_{1-x}$Asx system,* J. Phys.: Condens. Matter **8**, 8653 (1996).

[40] R. Hermann, O. Tegus, E. Brück, K. H. J. Buschow, F. de Boer, G. Long, and F. Grandjean, *Mössbauer spectral study of the magnetocaloric FeMnP$_{1-x}$As$_x$ compounds,* Phys. Rev. B **70**, 214425 (2004).

[41] M. Hudl, P. Nordblad, T. Björkman, O. Eriksson, L. Häggström, M. Sahlberg, Y. Andersson, E. K. Delczeg-Czirjak, and L. Vitos, *Order-disorder induced magnetic structures of FeMnP$_{0.75}$Si$_{0.25}$,* Phys. Rev. B **83**, 134420 (2011).

[42] O. Eriksson and A. Svane, *Isomer shifts and hyperfine fields in iron compounds,* J. Phys.: Condens. Matter **1**, 1589 (1989).

[43] S. A. Brawer, *Relaxation in Viscous Liquids and Glasses* (The American Ceramic Society, Columbus, OH, 1985) .

[44] S. A. Brawer, *Theory of relaxation in viscous liquids and glasses,* J. Chem. Phys. **81**, 954 (1984).

7

8

APPENDIX

8.1. DETERMINATION OF A MAGNETIC STRUCTURE USING NEUTRON DIFFRACTION

DETERMINATION of magnetic structures using neutron powder diffraction usually follows four steps:

(i) extract the magnetic reflections from the diffraction patterns;

(ii) obtain the propagation vector k of the unknown magnetic structure based on the positions of the magnetic reflections;

(iii) perform representation analysis to get irreducible representations (IRs);

(iv) according to IRs, try different magnetic configurations to find out the reasonable and best solutions.

As discussed in *Chapter 7*, the satellite reflections and the peak at $Q \approx 0.42\,\text{Å}^{-1}$ are the contributions from the unknown magnetic phase (see Fig. 7.3 in *Chapter 7*). An automatic k-indexing procedure was performed using the k-search program in the Fullprof package [1]. A propagation vector of $k = (0.355(1), 0, 0)$ is obtained, which is along the primitive vector a^* in the reciprocal space. This indicates an incommensurate magnetic structure (i.e., a helical spin configuration or a spin-density wave), propagating along the a^* in the reciprocal space.

The representation analysis [2, 3] was performed using the *BasIreps* program in the Fullprof package [1]. Representation analysis yields two nonzero irreducible representations (IRs) for both Fe and Mn moments on the $3f$ and $3g$ sites, respectively. One IR corresponds to both Fe and Mn moments along the c axis, and the other corresponds to both moments within the ab plane. A helical spin configuration with $k = (0.355, 0, 0)$ is not allowed by the IRs. As a result, the incommensurate-magnetic phase can be described by a sinusoidal spin-density wave (SDW) with $k = (0.355, 0, 0)$.

Different magnetic configurations were tried to fit the diffraction patterns, as shown in Table 8.1. The spin density wave with the Mn and Fe moments parallel and perpendicular to $\boldsymbol{k}$, respectively, gives the best fit with a magnetic R-factor of about 8.4%. A schematic representation of this magnetic structure is presented in Fig. 7.4 in *Chapter 7*.

REFERENCES

[1] J. Rodríguez-Carvajal, *Recent advances in magnetic structure determination by neutron powder diffraction,* Physica B **192**, 55 (1993).

[2] E. F. Bertaut, *Representation analysis of magnetic structures,* Acta Cryst. A **24**, 217 (1968).

[3] E. F. Bertaut, *On group theoretical techniques in magnetc structure analysis,* J. Magn. Magn. Mater. **24**, 267 (1981).

8

Table 8.1: Structural details derived from Rietveld refinement using different magnetic configurations for the $Mn_{1.30}Fe_{0.65}P_{0.67}Si_{0.33}$ (S1) sample.

Angle between Fe and Mn moments	Moment directions		Fe moment (μ_B)	Mn moment (μ_B)	R_{Mag}-factor (%)
0°	$M_{Fe} \parallel c$	$M_{Mn} \parallel c$	0.3(5)	1.6(5)	44.4
	$M_{Fe} \parallel a^*$	$M_{Mn} \parallel a^*$	0.7(3)	2.3(3)	24.1
	$M_{Fe} \parallel b$	$M_{Mn} \parallel b$	0.1(4)	3.2(4)	32.9
30°	$M_{Fe} \parallel a$	$M_{Mn} \parallel a^*$	0.7(2)	2.9(2)	11.9
	$M_{Fe} \parallel a^*$	$M_{Mn} \parallel a$	0.5(2)	3.0(2)	12.9
	$M_{Fe} \parallel b$	$M_{Mn} \parallel b^*$	0.5(3)	2.9(3)	24.8
	$M_{Fe} \parallel b^*$	$M_{Mn} \parallel b$	0.8(4)	1.8(4)	37.2
60°	$M_{Fe} \parallel b^*$	$M_{Mn} \parallel a^*$	0.8(2)	3.0(2)	12.9
	$M_{Fe} \parallel a^*$	$M_{Mn} \parallel b^*$	2.6(3)	1.9(3)	19.8
90°	$M_{Fe} \parallel b$	$M_{Mn} \parallel a^*$	0.8(2)	3.1(2)	8.4
	$M_{Fe} \parallel a^*$	$M_{Mn} \parallel b$	2.6(3)	0.7(3)	18.6
120°	$M_{Fe} \parallel b$	$M_{Mn} \parallel a$	0.2(3)	3.1(3)	17.2
	$M_{Fe} \parallel a$	$M_{Mn} \parallel b$	2.3(4)	1.2(4)	31.7

8

SUMMARY

THE $(Mn,Fe)_2(P,Si)$-based compounds show a strong magnetoelastic coupling, in which the ferromagnetic (FM) to paramagnetic (PM) transition is coupled to a structure change without altering the symmetry. A giant magnetocaloric effect is accompanied with the magnetoelastic transition, which makes $(Mn,Fe)_2(P,Si)$-based compounds promising materials for room-temperature refrigeration and energy conversion applications. This thesis stipulates ways of tuning the magnetoelastic transition and clarifies the phase-transition process on both length- and time-scales.

The tunability of the magnetoelastic transition in $(Mn,Fe)_2(P,Si)$-based compounds, triggered by subtle changes in the electronic configuration, is demonstrated by varying the P/Si ratio (*Chapter 3*) and by doping with B, C and N atoms (*Chapter 4*).

The differences in the magnetoelastic transition caused by changing the P/Si ratio is attributed to the Si site preference in combination with changes in the interatomic distances in the $(Mn,Fe)_2(P,Si)$ compounds (*Chapter 3*). The Si distribution on the $2c$ and $1b$ sites of the hexagonal crystal structures depends on the Si/P ratio, while it is independent of the Mn/Fe ratio. The FM-PM magnetoelastic transition is accompanied by a metamagnetic transition of the Fe atoms on the $3f$ site. The clear preference for Si to occupy the $2c$ site stabilizes the Fe moment on the same layer due to the charge transfer between the neighboring Fe and Si atoms. The intralayer interatomic distances expand for increasing Si contents, which also enhances the Fe moment on the $3f$ site. This finding is supported by first-principle electronic structure calculations.

The magnetoelastic transition of $(Mn,Fe)_2(P,Si)$-based compounds can also be tailored by doping with B, C and N atoms (*Chapter 4*). The site occupation of these light dopants within the crystal structure is resolved by neutron diffraction. B substitutes Si on the $1b$ site, while C occupies the interstitial $6j$ and $6k$ sites in the hexagonal lattice. N atoms occupy both the substitutional $1b$ and the interstitial $6j$ and $6k$ sites. The tuning effect on the magnetoelastic transition is caused by subtle variations in the electronic configuration, which in turn modifies the mixed magnetism responsible for the excellent magnetocaloric properties in these compounds.

$(Mn,Fe)_2(P,Si)$-based compounds show an unexpected thermal-history dependent magnetoelastic transition, called the "virgin effect" (*Chapter 5*). The

virgin effect is found to be related to a metastable state preserved in the as-prepared sample after high-temperature annealing. The as-prepared samples show larger variations in their atomic positions, as found by a structure analysis. The metastable phase transforms irreversibly to the stable low-temperature phase during the PM-FM transition upon the first cooling and is afterwards stabilized. Due to this additional transformation the energy barrier that needs to be overcome at the first cooling transition is higher and a lower T_C is observed in comparison to subsequent cooling processes. High temperature annealing can restore the high-temperature metastable state, which leads to the recovery of the virgin effect. Due to the change in T_C at the first-cooling transition, the as-prepared $(Mn,Fe)_2(P,Si)$ compounds should be precooled to remove the virgin effect before being used in magnetic refrigerators and power generators.

Neutron and muon studies on the magnetic correlations in the PM regime of $(Mn,Fe)_2(P,Si)$ provides, on both length- and time-scales, a better understanding of the magnetoelastic transition (*Chapter 6*). Short-range magnetic correlations are present at temperatures far above T_C both for first and second-order magnetic transitions. The short-range magnetic correlations extend in space and slow down with decreasing temperature, and finally develop into long-range magnetic order at T_C.

Due to the strong magnetoelastic coupling, $(Mn,Fe)_2(P,Si)$-based compounds may be magnetically ordered in different magnetic configurations. In contrast to the common PM-FM phase transition, an intermediate spin-density-wave (SDW) phase is observed for some compositions (*Chapter 7*). The PM-SDW transition is of second-order and accompanied with continuous changes in the lattice parameters. The SDW-FM transition, first-order in nature, is strongly coupled to discontinuous variations in the lattice parameters. The SDW-FM transition can be kinetically arrested, leading to a coexistence of the FM phase and the untransformed SDW phase at low temperature. The untransformed SDW phase is metastable at low temperatures, and can be converted into the stable FM phase by applying a magnetic field. The SDW-FM transition is accompanied by a significant increase in the Fe moment and a slight change in the Mn moment. This experimental finding fosters the strong magnetoelastic coupling and Fe moment instability (the theoretically predicted mixed magnetism) in the $(Mn,Fe)_2(P,Si)$ system.

SAMENVATTING

O<small>P</small> (Mn,Fe)$_2$(P,Si) gebaseerde materialen vertonen een sterke magneto-elastische koppeling, waardoor de faseovergang van de ferromagnetische (FM) naar de paramagnetische (PM) toestand gekoppeld wordt aan een structuurverandering, waarbij de kristalsymmetrie behouden blijft. Een reuze magneto-calorisch effect gaat gepaard met de magneto-elastische faseovergang, wat op (Mn,Fe)$_2$(P,Si) gebaseerde stoffen veelbelovende materialen maakt voor koeling bij kamertemperatuur en toepassingen op het gebied van energieconversie. Dit proefschrift definieert manieren om de magnetoelastische faseovergang af te stemmen en verduidelijkt het mechanisme van de faseovergang op zowel lengte- als tijdschalen.

De afstembaarheid van de magneto-elastische overgang in op (Mn,Fe)$_2$(P,Si) gebaseerde stoffen, teweeggebracht door subtiele veranderingen in de elektronenconfiguratie, wordt belicht door de P/Si verhouding te variëren (*Hoofdstuk 3*) en toevoeging van B, C en N atomen (*Hoofdstuk 4*).

De verschillen in de magneto-elastische overgang, veroorzaakt door de P/Si verhouding te veranderen, worden toegeschreven aan de voorkeur van Si voor posities in de kristalstructuur in combinatie met veranderingen in de interatomaire afstanden in de (Mn,Fe)$_2$(P,Si) materialen (*Hoofdstuk 3*). De verdeling van Si over de $2c$ en $1b$ posities in de hexagonale kristalstructuur hangt af van de Si/P verhouding, terwijl deze niet afhangt van de Mn/Fe verhouding. De FM-PM magneto-elastische overgang gaat gepaard met een reductie van het magnetisch moment op de $3f$ positie boven T_C. De duidelijke voorkeur van Si om de $2c$ positie te bezetten stabiliseert het Fe magnetisch moment op dezelfde laag door een ladingsoverdracht tussen de aangrenzende Fe en Si atomen. De afstanden tussen atomen van opeenvolgende lagen nemen toe bij toenemende Si concentratie, wat ook de magnetische momenten op de $3f$ positie vergroot. Deze bevinding wordt ondersteund door "ab initio" berekeningen van de elektronenstructuur. De verschillen in de magneto-elastische overgang, veroorzaakt door de P/Si verhouding te veranderen, worden toegeschreven aan de voorkeur van Si voor posities in de kristalstructuur in combinatie met veranderingen in de interatomaire afstanden in de (Mn,Fe)$_2$(P,Si) materialen (*Hoofdstuk 3*). De verdeling van Si over de $2c$ en $1b$ posities in de hexagonale kristalstructuur hangt af van de Si/P verhouding, terwijl deze niet afhangt van de Mn/Fe verhouding. De FM-PM magneto-elastische overgang gaat gepaard met een reductie van het magnetisch

moment op de $3f$ positie boven T_C. De duidelijke voorkeur van Si om de $2c$ positie te bezetten stabiliseert het Fe magnetisch moment op dezelfde laag door een ladingsoverdracht tussen de aangrenzende Fe en Si atomen. De afstanden tussen atomen van opeenvolgende lagen nemen toe bij toenemende Si concentratie, wat ook de magnetische momenten op de $3f$ positie vergroot. Deze bevinding wordt ondersteund door "ab initio" berekeningen van de elektronenstructuur.

De magneto-elastische overgang van op $(Mn,Fe)_2(P,Si)$ gebaseerde materialen kan ook worden gevarieerd door toevoeging van B, C en N atomen (*Hoofdstuk 4*). De door deze lichte atomen bezette posities in de kristalstructuur is bepaald met behulp van neutronenverstrooiing. B substitueert Si op de $1b$ positie, terwijl C de interstitiële $6j$ en $6k$ posities in het hexagonale rooster bezet. N atomen bezetten zowel de substitutionele $1b$ als de interstitiële $6j$ en $6k$ posities. De afstemming van de magneto-elastische overgang wordt veroorzaakt door subtiele variaties in de elektronenconfiguratie, die op hun beurt het "mixed magnetism" veranderen, wat verantwoordelijk is voor de excellente magneto-calorische eigenschappen in deze materialen.

Op $(Mn,Fe)_2(P,Si)$ gebaseerde stoffen vertonen een onverwachte afhankelijkheid van de thermische historie op de magneto-elastische overgang, dat bekend staat als het "virgin effect" (*Hoofdstuk 5*). Het virgin effect blijkt samen te hangen met een metastabiele toestand, die bewaard blijft in het "as-prepared" monster na temperen bij hoge temperatuur. Structuuranalyse toont aan dat "as-prepared" monsters grotere variaties in hun atoomposities vertonen. Tijdens de eerste afkoeling de metastabiele fase transformeert irreversibel in de stabiele lage-temperatuur fase bij de PM-FM overgang waarna de stabiele fase behouden blijft. Wegens deze extra transformatie is de energiebarrière die overschreden moet worden hoger bij de overgang tijdens de eerste koeling en wordt een lagere T_C waargenomen in vergelijking met de daaropvolgende koelingen. Temperen bij hoge temperatuur kan de metastabiele toestand herstellen, wat leidt tot terugkeer van het virgin effect. Wegens de afwijking in T_C gedurende de eerste koeling, moeten $(Mn,Fe)_2(P,Si)$ materialen vooraf gekoeld worden om het virgin effect te elimineren, voordat zij gebruikt kunnen worden voor magnetische koelapparaten en elektriciteitsgeneratoren.

Studies met behulp van neutronen en muonen aan de magnetische correlaties in het PM regime van $(Mn,Fe)_2(P,Si)$ verschaffen een beter begrip , op zowel lengte- als tijdschalen, van de magneto-elastische overgang (*Hoofdstuk 6*). Magnetische correlaties van korte dracht zijn aanwezig bij temperaturen ver boven T_C zowel voor eerste-orde als tweede-orde magnetische faseovergangen. De korte-dracht magnetische correlaties breiden zich uit in ruimte en duur bij afnemende temperatuur en ontwikkelen zich tenslotte tot lange-dracht magnetische ordening bij T_C.

Dankzij de sterke magneto-elastische koppeling kunnen $(Mn,Fe)_2(P,Si)$ gerelateerde materialen magnetisch ordenen in verschillende magnetische configuraties. In tegenstelling tot de gewone PM-FM faseovergang wordt voor sommige samenstellingen een spindichtheidsgolf (SDW) fase waargenomen voordat ferromagnetisme optreedt (*Hoofdstuk 7*). De PM-SDW faseovergang is een tweede-orde overgang en gaat vergezeld van continue veranderingen in de roosterparameters. De SDW-FM overgang is een eerste-orde overgang en vertoont discontinue veranderingen in de roosterparameters. De SDW-FM overgang kan kinetisch geremd worden, wat leidt tot een co existentie van de FM fase en de niet-getransformeerde SDW fase bij lage temperatuur. Het ongetransformeerde deel van de SDW fase is metastabiel bij lage temperatuur en kan omgezet worden in de stabiele FM fase door een magnetisch veld aan te leggen. De SDW-FM overgang gaat vergezeld van een significante toename van het Fe moment en een kleine verandering in het Mn moment. Deze experimentele bevinding is een bevestiging voor de sterke magneto-elastische koppeling en de instabiliteit van het Fe moment (het theoretisch voorspelde "mixed magnetism") in het $(Mn,Fe)_2(P,Si)$ systeem.

ACKNOWLEDGEMENTS

Staying in Delft in the past four years is the most memorable experience in my life so far. Time flies much faster than I feel and expect, but the happy times remain for ever. I feel proud of the improvements that I have made in both personal and professional senses. I cannot imagine what my PhD life would be like if I did not get the help, support and encouragement from my supervisors, colleagues, friends and family. Let me take this opportunity to express my gratitude to them.

First of all, I would like to thank my promotor Prof. Dr. Ekkes Brück, who provided me this great opportunity to work in his group. I will never forget the time when he taught me with great patience how to give a good presentation, especially his quotes "*Never do things in a rush*". He always encourages me to go to conferences and summer schools to exchange ideas with others. These external resources greatly benefit my PhD research. For instance, the speciallized training on neutron techniques and experiment-proposal writing skills in Oxford neutron school helped me to get valuable beamtime at large facilities, which allowed the acquisition of the neutron and muon data presented in this thesis. Ekkes is also easygoing and responsible for his students. I really appreciate his continuous negotiations with the graduate school on my defence date in order to reduce the unnecessary and long waiting time.

I sincerely appreciate the guidance of Dr. Niels van Dijk. I am deeply impressed by his strong expertise in solid-state physics, material science, neutron/X-ray techniques and so on. He always enlightened me on the insight into a scientific question, which makes a young scientist grow and become qualified. It was really enjoyable to hear about the funny and exotic stories in science and culture that he shared with us. Dear Niels, thank you for correcting my manuscripts extremely carefully every time, even an extra space between words. The attitude towards science that I learned from you will definitely benefit my scientific career.

I thank my daily supervisor Dr. Luana Caron, who keeps encouraging and inspiring me even after she left the group. She brings me a lot positive energy when I feel frustrated. She is always willing to share her knowledge and experience with me. She encouraged me to give presentations at international conferences and build my own academic network and collaborations. Her advice on research as well as on my career is priceless.

Many collaborators with different expertise made great contributions to my

PhD project. Prasenjit Roy and Prof. Dr. Robert de Groot contributed very beautiful work on theoretical calculations. The combination of my experimental results with their calculations provides explicit and in-depth understanding of many intriguing phenomena. Thank Dr. Iulian Dugulan and Michel Steenvoorden, who helped me with Mössbauer measurements. I deeply appreciate my colleague Dr. Paul Gubbens, and the collaborators Dr. Pierre Dalmas de Réotier and Alain Yaouanc at CEA Grenoble in France for the valuable discussions on the μSR data analysis. I acknowledge the low-temperature X-ray measurements by Johan Cedervall at Uppsala University in Sweden and the in-field X-ray measurements by Dr. Yoshifuru Mitsui at Kagoshima University in Japan. I would also like to thank the instrument scientists Dr. Winfried Kockelmann, Dr. Ron Smith and Dr. Pascal Manuel at ISIS in the UK, Andrew Wildes at ILL in France, Dr. Alex Amato and Dr. Luetkens Hubertus at PSI in Switzerland for their assistance in the neutron and muon experiments. The discussions with Dr. Juan Rodriguez-Carvajal at ILL about Rietveld refinement using Fulllprof served me a lot in the neutron/X-ray data analysis.

I enjoyed very much working in RID with so many lovely colleagues. Anton is such an important person that he is always the first person coming to my mind whenever I have troubles and need helps in the labs. I thank Dr. Jouke Heringa not only for his technical maintenance on the computer and softwares but also the advice on my research and career development. The great administrative supports from Ilse, Nicole and Trudy made my PhD life easier. It was so fun to enjoy the coffee time with the colleagues from all over the world, Anca, Anna, Swapna, Jose, Dũng, Giacomo, Thắng, Maurits, Steven, Prasad, Maik, Michael, Francesco, Francois, Dimitris, Lambert, Jeroen, Henk, Michel, Fred, Evgenii, Bert and Ben. It was also a great time to play cards/mahjong, have BBQ and share tasty food with my Chinese friends and colleagues in TU Delft: Zhiqiang Ou, Kun Shen, Hao Chen, Xiaoyu Zhang, Shasha Zhang, Chuanqing Shi, Wenqing Shi, Jiayi Chen, Chuang Yu, Yaolin Xu, Bo Peng, Zhaolong Li, Mengqiu Zheng, Haixing Fang, Tiantian Yao, Yibole, Xinmin You, Jiawei Lai, Bowei Huang, Zhou Zhou, Shan Shen, Qiao Pan, Bei Tian, Hongde Luo, Zheng Liu, Nan Zhong, Lian Zhang and Lily. These interesting social activities successfully defeated my sense of homesickness.

I would like to give my special gratitude for a group of people who made my PhD life so colorful: the RID pingpong team! Thắng, as a representative and the most active player, showed an incredible progress from a beginner to a RID-high-level player. His dream of beating Peter-Paul and Carla, who are the famous RID pingpong players, may come true after some practice. We are creative in RID pingpong rules and enthusiastic about our games.

I am particularly grateful to Prof. Dr. Yingang Wang, the supervisor of my

master thesis, Dr. Xiaomei Feng and Prof. Dr. Tao Wang. With their support and encouragement, I managed to work in Delft and had a wonderful time here.

I deeply appreciate the love and support from my parents, grandparents and parents in law. They encourage me to pursue my dreams traveling far away from hometown, but always worry about my life in a foreign country. I also thank Chun Cai, Liujin Wu, Meijiao Qian, Jie Gu, Min Ding and Mengqi Cong, who take me as their brother. They are the people who I want to share my happiness and sadness the first time.

Last but certainly not least, a special thanks goes to my beloved wife, Fengjiao, whom I have been in love with for nine years. We learn from each other and complement each other, like neutrons and magnetism. Sometimes we have disagreements on science and daily life, but both of us know the art of living together. She always knows how to cheer me up when I'm down, and feels even happier than I do whenever I make an achievement. Thanks, Fengjiao, for your love and lighting up my life.

LIST OF PUBLICATIONS

PUBLICATIONS RELATED TO THE THESIS

1. **X. F. Miao**, Y. Mitsui, I. Dugulan, P. Roy, L. Caron, N. V. Thang, K. Koyama, K. Takahashi, R. A. de Groot, N. H. van Dijk, and E. Brück, *"Kinetic-arrest induced phase coexistence and metastability in (Mn,Fe)$_2$(P,Si)"*, submitted.

2. **X. F. Miao**, N. V. Thang, L. Caron, H. Yibole, R. Smith, N. H. van Dijk, and E. Brück, *"Tuning the magnetoelastic transition in (Mn,Fe)$_2$(P,Si) by B, C, and N doping"*, submitted.

3. **X. F. Miao**, L. Caron, J. Cedervall, P. C. M. Gubbens, P. Dalmas de Réotier, A. Yaouanc, F. Qian, A. R. Wildes, H. Luetkens, A. Amato, N. H. van Dijk, and E. Brück, *"Short-range magnetic correlations and spin dynamics in the paramagnetic regime of (Mn,Fe)$_2$(P,Si)"*, Phys. Rev. B, accepted (2016) .

4. **X. F. Miao**, L. Caron, P. C. M. Gubbens, P. Dalmas de Réotier, A. Yaouanc, H. Luetkens, A. Amato, N. H. van Dijk, and E. Brück, *"Spin correlations in (Mn,Fe)$_2$(P,Si) compounds above Curie temperature"*, Journal of Science: Advanced Materials and Devices, accepted (2016).

5. **X. F. Miao**, L. Caron, Z. Gercsi, A. Daoud-Aladine, N. H. van Dijk, and E. Brück, *"Thermal-history dependent magnetoelastic transition in (Mn,Fe)$_2$(P,Si)"*, Appl. Phys. Lett. **107**, 042403 (2015).

6. **X. F. Miao**, L. Caron, P. Roy, N. H. Dung, L. Zhang, W. A. Kockelmann, R. A. de Groot, N. H. van Dijk, and E. Brück, *"Tuning the phase transition in transition-metal-based magnetocaloric compounds"*, Phys. Rev. B **89**, 174429 (2014).

OTHER PUBLICATIONS

7. S. Ganapathy, M. Anastasaki, S. Basak, Z. L. Li, **X. F. Miao**, K. Goubitz, F. Mulder, M. Wagemaker, *"The use of nano seed crystals to control peroxide morphology in a non-aqueous Li-O$_2$ battery"*, submitted.

8. A. Davarpanah, J. S. Amaral, V. S. Amaral, E. C. Queirós, P. B. Tavares, **X. F. Miao**, L. Caron, and E. Brück, *"Thermal conductivity of magnetocaloric materials: challenges and opportunities for magnetic refrigeration and thermal management"*, submitted.

9. N. V. Thang, **X. F. Miao**, N. H. van Dijk, and E. Brück, *"Structural and magnetocaloric properties of (Mn,Fe)$_2$(P,Si) materials with added nitrogen"*, J. Alloys Compd. **670**, 123 (2016).

10. J. Dai, Y. G. Wang, **X. F. Miao**, L. Yang, G. Q. Guo, and G. T. Xia, *"Atomic-scale mechanisms of annealing-induced coercivity modification in metallic glass"*, J. Mater. Sci., DOI: 10.1007/s10853-016-0125-z (2016).

11. M. F. J. Boeije, P. Roy, F. Guillou, H. Yibole, **X. F. Miao**, L. Caron, D. Banerjee, N. H. van Dijk, R. A. de Groot, and E. Brück, *"Efficient room-temperature cooling with magnets"*, Chem. Mater., DOI: 10.1021/acs.chemmater.6b00518 (2016).

12. L. Ma, F. Guillou, H. Yibole, **X. F. Miao**, A. J. E. Lefering, G. H. Rao, Z. F. Gu, G. Cheng, and E. Brück, *"Structural, magnetic and magnetocaloric properties of (Mn,Co)$_2$(Si,P) compounds"*, J. Alloys Compd. **625**, 95 (2015).

13. S. Ganapathy, B. D. Adams, G. Stenou, M. S. Anastasaki, K. Goubitz, **X. F. Miao**, L. F. Nazar, and M. Wagemaker, *"Nature of Li$_2$O$_2$ oxidation in a Li-O$_2$ battery revealed by operando x-ray diffraction"*, J. Am. Chem. Soc. **136**, 16335 (2014).

14. L. Caron, **X. F. Miao**, J. C. P. Klaasse, S. Gama, and E. Brück, *"Tuning the giant inverse magnetocaloric effect in Mn$_{2-x}$Cr$_x$Sb compounds"*, Appl. Phys. Lett. **103**, 112404 (2013).

15. F. G. Chen, Y. G. Wang, **X. F. Miao**, H. Hong, and K. Bi, *"Nanocrystalline Fe$_{83}$P$_{16}$Cu$_1$ soft magnetic alloy produced by crystallization of its amorphous precursor"*, J. Alloys Compd. **549**, 26 (2013).

16. **X. F. Miao**, and Y. G. Wang, *"Crystallization mechanism and its correlation with structural and soft magnetic properties of FeSiBPCu nanocrystalline alloys"*, J. Mater. Sci. **47**, 1745 (2012).

17. **X. F. Miao**, Y. G. Wang, and M. Guo, *"Structural, thermal and magnetic properties of Fe-Si-B-P-Cu melt-spun ribbons: Application of non-isothermal kinetics and the amorphous random anisotropy model"*, J. Alloys Compd. **509**, 2789 (2011).

PATENTS

1. E. Brück, **X. F. Miao**, N. V. Thang, *"Magnetocaloric materials comprising manganese, iron, silicon, phosphorus and nitrogen"*, European Patent, application no. 15192313.3, 2015.

2. Y. G. Wang, **X. F. Miao**, *"Iron-based nanocrystalline soft-magnetic alloy"*, Chinese Patent, CN201110418631, granted in 2014.

3. Y. G. Wang, **X. F. Miao**, and M. Guo, *"Iron-based nanocrystalline soft-magnetic alloy with high quenching-state toughness and wide annealing-temperature range"*, Chinese Patent, CN201010601563, granted in 2012.

CONFERENCE PRESENTATIONS

1. Oral presentation (invited): **X. F. Miao**, N. H. van Dijk, E. Brück, *et al*, *"Neutron scattering studies on (Mn,Fe)$_2$(P,Si) magnetocaloric materials"*, MLZ-Conference: Neutrons for Energy, Germany, 2016.

2. Oral presentation: **X. F. Miao**, N. H. van Dijk, E. Brück, *et al*, *"Kinetic-arrest induced phase coexistence and metastability in (Mn,Fe)$_2$(P,Si)"*, 13th Joint MMM-Intermag conference, USA, 2016.

3. Poster presentation: **X. F. Miao**, N. H. van Dijk, E. Brück, *et al*, *"Magnetic short-range order and spin dynamics in the paramagnetic regime of (Mn,Fe)$_2$(P,Si)"*, 13th Joint MMM-Intermag conference, USA, 2016.

4. Oral presentation (invited): **X. F. Miao**, N. H. van Dijk, E. Brück, *et al*, *"Kinetic-arrest in (Mn,Fe)$_2$(P,Si) compounds"*, DDMC, Netherlands, 2015.

5. Oral presentation: **X. F. Miao**, N. H. van Dijk, E. Brück, *et al*, *"Peculiar virgin effect in (Mn,Fe)$_2$(P,Si)"*, Intermag, China, 2015.

6. Oral presentation: **X. F. Miao**, N. H. van Dijk, E. Brück, *et al*, *"Thermal-history dependent phase transition in (Mn,Fe)$_2$(P,Si) compounds"*, Thermag VI, Canada, 2014.

7. Oral presentation: **X. F. Miao**, N. H. van Dijk, E. Brück, *et al*, *"Tuning the phase transition by Si substitution in Mn$_{1.25}$Fe$_{0.70}$P$_{1-x}$Si$_x$ compounds"*, CIMTEC conference, Italy, 2014.

8. Poster presentation: **X. F. Miao**, N. H. van Dijk, E. Brück, *et al*, *"Tunable phase transition in (Mn,Fe)$_2$(P,Si) compounds"*, JEMS, Greece, 2013.

9. Oral presentation: **X. F. Miao**, N. H. van Dijk, E. Brück, *et al*, *"Neutron diffraction study on Mn$_{1.25}$Fe$_{0.70}$P$_{1-x}$Si$_x$ compounds"*, DDMC, Netherlands, 2013.

10. Oral presentation: **X. F. Miao**, N. H. van Dijk, E. Brück, *et al*, *"Si site preference and its influence on phase transition in (Mn,Fe)$_2$(P,Si) compounds"*, 58th MMM conference, USA, 2013.

CURRICULUM VITÆ

Xue-Fei MIAO

Xue-Fei Miao was born on January 23rd, 1987 in Nantong, China. He attended Nanjing University of Aeronautics and Astronautics as an undergraduate student and majored in Materials Science and Engineering. In 2009, he graduated with honor and was recommended as a master student in the same university with exemption from the admission examinations.

In 2012, he received a Master's degree with honor in Materials Science and Engineering at Nanjing University of Aeronautics and Astronautics. The master project, supervised by Prof. Dr. Yingang Wang, was on optimizing the magnetic properties of Fe-based amorphous and nanocrystalline materials.

From June of 2012, he started his PhD project on magnetocaloric materials under the supervision of Prof. Dr. Ekkes Brück and Dr. Niels van Dijk at Delft University of Technology, Netherlands. A variety of experimental techniques, e.g. polarized neutron diffraction, Mössbauer spectroscopy, muon-spin relaxation and electron microscopy were employed for a better understanding of the magneto-elastic coupling in magnetocaloric $(Mn,Fe)_2(P,Si)$-type compounds. The results of this research are presented in this thesis entitled "Magnetoelastic coupling in $(Mn,Fe)_2(P,Si)$ compounds".

Propositions

accompanying the dissertation

MAGNETOELASTIC COUPLING IN MN-FE-P-SI COMPOUNDS

by

Xue-Fei MIAO

1. Discovery of new material systems may renew the interest in old research topics.

2. The tunability of magnetoelastic transition in $(Mn,Fe)_2(P,Si)$ upon doping can be understood by the modifications on crystal and electronic structures.

3. In refrigeration and power conversion applications, the metastable states of $(Mn,Fe)_2(P,Si)$ formed by high-temperature annealing or by a low-temperature kinetic arrest need to be taken into consideration.

4. Magnetoelastic transition in $(Mn,Fe)_2(P,Si)$ is proceeded by the formation of short-range magnetic correlations. The short-range correlations extend in space and slow down on cooling, and finally develop into long-range order.

5. Mixed magnetism in Fe_2P-type compounds is due to the distinct chemical environment around the two metallic sublattice sites.

6. The capability to distinguish Mn from Fe and P from Si atoms, as well as detecting sublattice magnetic moment, makes neutrons better than X-ray for studying $(Mn,Fe)_2(P,Si)$.

7. Patents are good to protect commercial interest but not for the development of science and technology.

8. Polarization in neutron and X-ray experiments is as powerful as spinning balls in table tennis.

9. Tulip blooms after a cold winter, one grows after a tough period.

10. Pronunciation of "r" in Dutch for Asian people is as challenging as that of "Zh-" in Mandarin for western people.

These propositions are regarded as opposable and defendable, and have been approved as such by the promotor Prof. dr. E.H. Brück and copromotor Dr. ir. N.H. van Dijk.